METAL OXIDE REACTIONS IN COMPLEX ENVIRONMENTS: HIGH ELECTRIC FIELDS AND PRESSURES ABOVE ULTRAHIGH VACUUM

Feili Qin, B.S., M.S.

Dissertation Prepared for the Degree of

DOCTOR OF PHILOSOPHY

UNIVERSITY OF NORTH TEXAS

August 2005

APPROVED:

Jeffry A. Kelber, Major Professor
Teresa D. Golden, Committee Member
Terry. D. Golding, Committee Member
Angela Wilson, Committee Member
Bruce Gnade, External Committee Member
Ruthanne D. Thomas, Chair of the Department of Chemistry
Sandra L. Terrell, Dean of the Robert B. Toulouse School of Graduate Studies

Qin, Feili. Metal Oxide Reactions in Complex Environments: High Electric Fields and Pressures above Ultrahigh Vacuum. Doctor of Philosophy (Analytical Chemistry), August 2005, 134 pp., 36 illustrations, reference list, 205 titles.

Metal oxide reactions at metal oxide surfaces or at metal-metal oxide interfaces are of exceptional significance in areas such as catalysis, micro- and nanoelectronics, chemical sensors, and catalysis. Such reactions are frequently complicated by the presence of high electric fields and/or H_2O-containing environments. The focus of this research was to understand (1) the iron oxide growth mechanism on Fe(111) at 300 K and 500 K together with the effect of high electric fields on these iron oxide films, and (2) the growth of alumina films on two faces of Ni_3Al single crystal and the interaction of the resulting films with water vapor under non-UHV conditions. These studies were conducted with AES, LEED, and STM. XPS was also employed in the second study.

Oxidation of Fe(111) at 300 K resulted in the formation of Fe_2O_3 and Fe_3O_4. The substrate is uniformly covered with an oxide film with relatively small oxide islands, i.e. 5-15 nm in width. At 500 K, Fe_3O_4 is the predominant oxide phase formed, and the growth of oxide is not uniform, but occurs as large islands (100 - 300 nm in width) interspersed with patches of uncovered substrate. Under the stress of STM induced high electric fields, dielectric breakdown of the iron oxide films formed at 300 K occurs at a critical bias voltage of 3.8 ± 0.5 V at varying field strengths. No reproducible result was obtained from the high field stress studies of the iron oxide formed at 500 K.

$Ni_3Al(110)$ and $Ni_3Al(111)$ were oxidized at 900 K and 300 K, respectively. Annealing at 1100 K was required to order the alumina films in both cases. The results demonstrate that the structure of the 7 Å alumina films on $Ni_3Al(110)$ is κ-like, which is in good agreement with the DFT calculations. $Al_2O_3/Ni_3Al(111)$ (γ'-phase) and $Al_2O_3/Ni_3Al(110)$ (κ-phase) films undergo drastic reorganization and reconstruction, and the eventual loss of all long-range order upon exposure to $P_{H_2O} > 10^{-5}$ Torr.

$Al_2O_3/Ni_3Al(110)$ film is significantly more sensitive to H_2O vapor than the $Al_2O_3/Ni_3Al(111)$ film, and this may be due to the incommensurate nature of the oxide/$Ni_3Al(110)$ interface. STM measurements indicate that this effect is pressure- rather than exposure- dependent, and that the oxide instability is initiated at the oxide surface, rather than at the oxide/metal interface. The effect is *not* associated with formation of a surface hydroxide, yet is specific to H_2O (similar O_2 exposures have no effect).

ACKNOWLEGEMENTS

I would like to express my special gratitude to my research advisor, Dr. Jeffry A. Kelber, for his guidance and support. Financial support from the Robert Welch foundation under grant B-1356 is gratefully acknowledged. I appreciate Dr. Noel P. Magtoto and Dr. Dwight R. Jennison for informative discussions. I extend my appreciation to my doctoral committee members Dr. Teresa D. Golden, Dr. Angela Wilson, Dr. Terry. D. Golding, and Dr. Bruce Gnade from University of Texas-Dallas.

Especially, I am forever grateful to my husband, Yuhua Zhang, for his constant love, support, and encouragement. Immeasurable thanks go to my three sisters, Huili, Suli, and Yali, for rendering me the sense and the value of sisterhood. I am glad to be one of them.

This thesis is dedicated to the memory of my mother and my father who formed part of my vision and taught me the good things that really matter in life. The happy memory of my mother still provides a persistent inspiration for my journey in this life.

TABLE OF CONTENTS

LIST OF ILLUSTRATIONS

CHAPTER 1

INTRODUCTION

Metal oxides comprise a very diverse class of materials with properties covering the entire range from conductors to semiconductors and insulators [1]. Metal oxides find applications in many fields of scientific and technological importance, including heterogeneous catalysis, micro- and nanoelectronics, chemical sensors, high temperature corrosion inhibitors, composite materials, and optics [2-4]. The high melting points, low density, hardness, and selective reactivity of many metal oxides are well suited to these applications. In many of these applications, metal oxide reactions play a key role in the performance [1, 5]. Understanding the reactions at metal oxide surfaces or at metal-metal oxide interfaces in different environments is of exceptional significance since it is either at the oxide surface or at the metal-oxide interface where processes such as spallation, corrosion, diffusion and wetting occur. For example, metal oxides are ubiquitous in heterogeneous catalysis, serving as catalysts, as catalyst supports, and as modifiers and promoters, among other roles. Metal oxide reactions have a direct effect on the mechanical stability and catalytic activity of the catalysts [1, 3]. In addition, the moisture-induced spallation of metal oxide (alumina and iron oxides) scales from Ni, or Fe-based alloys is a serious problem in the development of materials for advanced high temperature applications [6]. Furthermore, the stability of ultrathin metal oxide

barrier films under non-UHV conditions is a crucial concern in device processing where substrates are exposed to relatively poor vacuum or air during processing steps [7].

Although metal oxides are of broad scientific and technological interest under a variety of non-ultrahigh vacuum (non-UHV) conditions, detailed studies of metal oxide surfaces are typically carried out under rigorously controlled UHV environments [3, 8-13]. This discrepancy arises in part because most modern surface spectroscopies, e.g. Auger electron spectroscopy (AES), low energy electron spectroscopy (LEED), scanning tunneling microscopy (STM) and x-ray photoelectron spectroscopy (XPS) that provide detailed structural and compositional information about a surface, are UHV-based techniques [13, 14]. A common criticism of the UHV approach has been that it is too far removed from the real world, since there may exist "pressure gaps"- qualitative differences between surface properties observed under UHV vs. higher pressure conditions [15]. A number of natural and industrial processes do not occur under such rarified conditions. Adsorbates that are weakly bound to a surface, for example, may play important roles in surface reactions at ambient or higher pressures, but cannot be observed under UHV conditions except at low temperatures, where the chemical reaction is kinetically hindered [16].

In the real world, reactions occurring at either metal oxide surfaces or at metal/metal oxide interfaces are often complicated by the presence of interfacial impurities such as sulfur [17-19] and carbon [20] or by H_2O-containing environments. The effects of interface impurities have been extensively studied [17-20]. On the other hand, the effects of water molecules on metal oxides at the pressure range of 10^{-6} to 1

Torr, which play a crucial role in their surface properties including surface reactivity, have not attracted much attention. Furthermore, specifically adsorbed ions (Cl^-, OH^-, H^+, etc.) can induce electric fields greater than 1 MV/cm across a thin oxide film grown on a metallic substrate [21]. The behavior of ultrathin metal oxide films under high electric field is of critical importance to the development of magnetroresistance memories [22-24] and advanced gate oxides [25]. Despite their obvious importance, to the knowledge of the author, high electric field effects on most metal oxides have not been systematically studied.

The goal of the present study is to provide an in-depth understanding of the effects of environment (i.e., high electric field and intermediate pressures ($>10^{-7}$ Torr – 0.1 Torr) of water vapor) on selected metal oxides. Following oxygen and silicon, aluminum and iron are the most abundant elements in the Earth's crust [26]. As a result, aluminum and iron oxides and hydroxides are among the most abundant materials in the Earth's surface. Aluminum and iron oxides were selected because of their obvious technological importance. This dissertation consists of four chapters. The current chapter provides background information on the fundamental concepts of metal/oxide interaction and adsorbate/metal oxide surface interaction, as well as experimental methodology. In chapter 2, characterization of oxide films grown on Fe(111) at 300 K and 500 K together with the high electric field effects on these films are presented. Chapter 3 reports the theory and experimental studies on the structure of 7 Å alumina films grown on $Ni_3Al(110)$ single crystal. Chapter 4 investigates the interaction of the ultrathin alumina films grown on two faces of Ni_3Al with water vapor under non-UHV conditions.

1.1. Oxide/ Metal and Adsorbate/Oxide Interactions: Basic Concepts

1.1.1. Oxide Growth on Metals and Alloys

Metal oxidation processes are extensively used in technology for protection of materials against corrosion, and production of engineering ceramics and catalysts. The initial stages of oxidation (including oxygen adsorption and dissociation, oxide island nucleation, and growth into a continuous film) as illustrated in Fig. 1.1 [27, 28] have been actively studied and are now understood relatively well [27-29]. Initially, there will be physical adsorption of oxygen molecules on the bare metal surface, which means the oxygen molecules are loosely bound to the metal surface. The molecules then dissociate into atoms that are strongly bound to the metal surface by chemisorption. The enthalpy of the physical adsorption process is relatively small, i.e., 20-25 KJ mol^{-1}, compared to that of chemisoption (as high as 600 KJ mol^{-1}). Previous LEED studies [30] indicate that the chemisorption process of oxygen is connected with the movement of a specific number of metal atoms into the plane of the adsorbed oxygen atoms. The second step involves a general chemical reaction to form small oxide nuclei on the surface [31]:

$$x\,M + \tfrac{1}{2}\,(y\,O_2) \rightarrow M_xO_y \qquad (1\text{-}1)$$

The above reaction consists of two spatially isolated electrochemical processes [27]:

(1) oxidation of metal atoms at the oxide-metal interface:

$$M \rightarrow M^{y+} + y\,e^- \qquad (1\text{-}2a)$$

(2) oxidant reduction at the oxide-gas interface by the electrons liberated in (1-2a):

$$\tfrac{1}{2}\,O_2 + 2\,e^- \rightarrow O^{2-} \qquad (1\text{-}2b)$$

The oxide nuclei formed in the second step continue to grow laterally until they coalesce, and at this point the metal is covered entirely with a continuous oxide film M_xO_y (Fig. 1.1). The continuous oxide film protects or 'passivates' the underlying metal from further oxidation/corrosion [28].

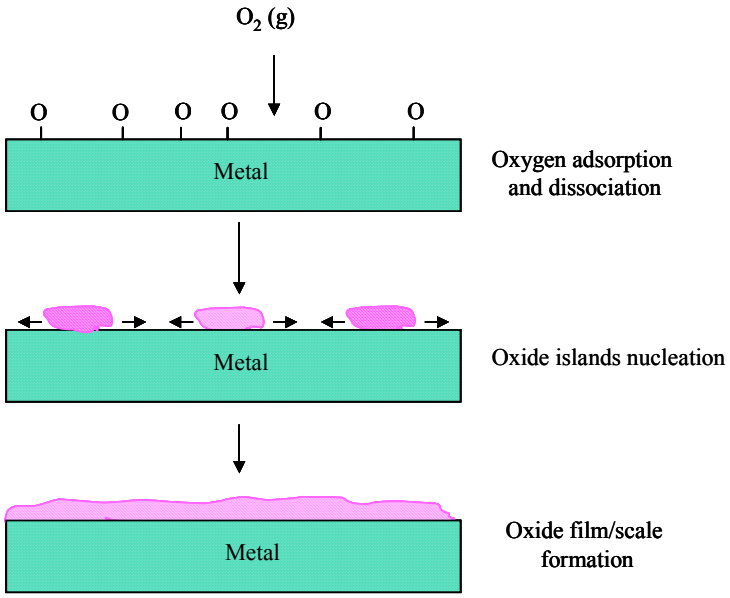

Fig. 1.1. Three steps involved in the initial stage of oxidation of metals.

The process of oxidation can be divided into two categories, low-temperature and high-temperature oxidation, depending on the metal and time-temperature-pressure relationship during the oxidation process. In low-temperature oxidation, the thermal energy is not enough to allow existing ions or electrons (or holes) to surmount the energy barrier to diffusion. As a result, the driving force for the formation of oxides at low

temperature is an electric field. Across very thin oxide films, a very strong electric field is created. An oxidation potential is usually on the order of one volt, hence, there will be a field of ~ 10^7 V cm^{-1} across a film with a thickness of ~ 1 nm [28]. A logarithmic growth rate is typical for low temperature oxidation. The products of high-temperature oxidation are often polycrystalline and contain paths (grain boundaries) for easy ion diffusion. In high-temperature oxidation, thermal energy is sufficient for ion generation and movement through the oxide even though a small electric field may be present. A parabolic growth rate is generally followed. The actual temperature of transition from low- to high-temperature oxidation is a function of the material, its perfection, and purity.

According to their crystallographic states, the metals can be divided into three types: single crystal, polycrystalline, and amorphous metals. Single crystal and amorphous metals differ from polycrystalline metal in that no grain boundaries are present. For oxidation, the type of substrate has a direct effect on the oxidation rate and the quality of the growing oxide films. Even carefully prepared oxide films grown on polycrystalline metal substrates contain defective regions. The defective regions provide paths for facile ion movement and thus, fast oxide growth. Single crystal and amorphous metals minimize such defects and should, therefore, produce higher quality oxides that result in a slower rate of oxidation [32, 33].

Oxidation kinetics is generally described with reference to the mathematical relationship existing between the oxide thickness, *d*, and time, *t*. The kinetics of thick oxide films (> 100 nm) and thin films (< 100 nm) are quite different. At low temperatures, and for thinner oxide films, these relationships are logarithmic, i.e., the rate

of growth of the film or the increase in film thickness obeys an inverse dependence with time, according to the equation [27, 28]:

$$d = K_r \log t \tag{1-3}$$

where K_r is the rate constant. In oxidation processes obeying logarithmic rate laws, after a certain limiting thickness (typically 100 nm) is attained, the initially high oxide growth rate will fall off quickly, unless sufficient thermal energy is supplied to the system to promote further film growth by ionic diffusion through the film under the influence of a concentration gradient [28]. At high temperatures, the rate of oxidation ceases to obey the logarithmic-type law and the growth of thick oxide films obey parabolic growth kinetics [27, 28]:

$$d^2 = K_r t \tag{1-4}$$

In Eqn. (1-4), K_r is the parabolic rate constant. The parabolic rate constant K_r increases exponentially with increase in temperature. Oxide growth under these conditions is extremely fast, as the thickness increases as d^2 with time, and involves diffusion of ions via point defects [27, 28]. Thicker oxide films are usually called oxide scales. The difference between a thin film and a scale is often described in terms of oxide thickness, d, and growth rate, although there is no specific value of d that marks the difference [28].

Thin oxide films can be prepared by a variety of methods [33-39] including laser and arc deposition [35], molecular beam epitaxy (MBE) deposition [33], sol-gel deposition [36], chemical vapor deposition (CVD) [37], plasma-enhanced CVD [38], and laser induced CVD [39]. The preparation of ultrathin oxide films for surface science studies is often accomplished by oxidizing a metal (metal alloy, or semiconductor)

substrate (forming a thin film of the native oxide), or evaporating a metal on a refractory metal substrate in the presence of oxygen [33]. These thin films, however, often have a large density of defects (vacancies, interstitials, dislocations, domain walls, different phases and variants, grain and sub-grain boundaries, etc.), which may completely change their electronic and spectroscopic properties. Therefore, it is often mandatory to use single crystals to control the type and the density of defects which may play a key role on the oxide properties [40].

Oxides prepared by the oxidation of single crystal binary intermetallic alloys include Al_2O_3/NiAl [41-44], Al_2O_3/Ni_3Al [45-52], Al_2O_3/FeAl [53-55], and Ga_2O_3/CoGa [56, 57] etc. In general, oxidation at room temperature results in the formation of amorphous oxide layers, and subsequent annealing to elevated temperatures is needed to produce an ordered oxide film. Usually the temperature required to order the oxide film is much higher than the melting temperature of the pure metal. For example, annealing to 1000 ~ 1200 K followed by room temperature oxidation is necessary to produce well-ordered thin Al_2O_3 films [42, 44, 47, 52], whereas the melting point of pure aluminum metal is only 930 K. The use of intermetallic alloys for the growth of ultrathin oxide films offers the advantage in that higher annealing temperatures can be used for ordering the oxide film without melting the substrate. Well-ordered Al_2O_3 films have been successfully prepared by direct oxidation of NiAl and Ni_3Al single crystal substrates followed by subsequent high temperature annealing [44, 47, 51, 52]. However, the presence of a large lattice mismatch between the alloy surface and the oxide lattice

constant may also lead to the formation of an oxide film with a rather high defect density [3].

1.1.2. Classification of Metal/Oxide Interfaces

The metal/oxide interface is ubiquitous in technology: the protective oxide on beverage cans, the non-protective rust, electrodes on dielectrics, catalysts and sensor materials on oxide substrates. In order for the metal and oxide to keep in contact, there must exist a region through which the intensive properties of the system change from one phase to those of another. Such a region is defined as the metal/oxide interface. Metal/oxide interfaces are special among all heterointerfaces since metals and oxides are quite different in most material properties. For example, bonds in metals are characterized by the delocalization of the electrons. In contrast, most oxides, due to the high electron negativity of oxygen compared with metals, tend to mainly have ionic bonding in which one or more electrons from one atom are removed and attached to another atom. As a result, compared to metal, oxides are usually brittle, elastically stiffer, insulating and have poor thermal conductivity [2].

The use of thin ordered oxide films grown on conducing substrates in model studies offers many advantages over amorphous samples in that such films minimize the influence of parameters such as defect density and grain boundaries that may play a role in the reactivity of the surfaces or the metal/oxide interfaces [41, 42]. Furthermore, the extremely thin nature of such films allows surface science techniques, including XPS, LEED, and STM to directly probe in great detail the changes in the structure and

composition of the well-ordered metal/oxide interfaces and oxide surfaces. Any charging induced in the oxide film during spectroscopic measurements can be dissipated via the metal substrate. A well-known example of this kind is the formation of well-ordered thin alumina films on the low indexed surfaces of certain Al alloys such as NiAl and Ni_3Al [41, 42, 46, 49, 52].

Based on the nature of the reaction products that are formed at the interfaces, metal/oxide interfaces may be classified as follows [20]:

1. Abrupt interface. No chemical reactions occur during the formation of an abrupt interface. The weak bond between metal, R, and metal oxide, MO_y, is associated with the absence of electron transfer from the metallic overlayer to the substrate. Furthermore, the interface is characterized by an abrupt change from one phase to another (R/MO_y). Cu/TiO_2 is a typical example [58-60].
2. Oxide interface. The formation of oxide interfaces involves a redox reaction at the interface between a metal, R, and an oxide, MO_y. Systems in which a stronger bond is observed usually imply that the overlayer atoms are oxidized due to the interaction with lattice oxygen. Oxidation of the overlayer metal is usually accompanied by a reduction of the substrate cations. The interface may be binary ($R/RO_x/MO_y$), ternary ($R/MRO_{x+y}/MO_y$) or an oxide solution (R/RO_x-MO_y/MO_y). Examples of these types are $Al/Al_2O_3/TiO_2$ [61], $Ni/NiAl_2O_4/Al_2O_3$ [62, 63], and Ni/NiO-MgO/MgO [64], respectively.
3. Intermetallic interface. A metal alloy is formed at the interface as a result of the reaction of a metal, R, with the metal atoms from an oxide, MO_y, which may be

represented as R/M-R/MO_y. At an Al/NiO interface, a Ni_3Al interfacial layer is generally observed [65].

1.1.3. Adsorbate/Surface Interactions on Metal Oxides

There are two principal modes of adsorption of gas molecules on surfaces: physical adsorption (physisorption) and chemical adsorption (chemisorption). The basis of distinction is the nature of the bonding between the molecule and the surface. In physisorption the only bonding is by weak Van der Waals - type forces (intermolecular forces). Physisorption occurs without molecular dissociation. There is no significant redistribution of electron density in either the molecule or at the substrate surface. In chemisorption, a chemical bond, involving substantial rearrangement of electron density, is formed between the adsorbate and substrate. The nature of this bond may lie anywhere between the extremes of virtually complete ionic or complete covalent character. Molecules often dissociate when chemisorbed. The problem of distinguishing between chemisorption and physisorption is basically the same as that of distinguishing between chemical and physical interaction in general. No absolutely sharp distinction can be made and intermediate cases exist, for example, adsorption involving strong hydrogen bonds or weak charge transfer [1, 66].

Chemisorption on metal oxide surfaces follows a considerably different pattern from that on metals [1]. The relatively ionic nature of the metal oxides due to the presence of both cations and anions on the surface, leads to a predominance of acid/base, or donor/acceptor, interactions. Cation sites are Lewis acids, and may interact with donor

molecules such as H_2O through a combination of electrostatics and orbital overlap. Oxide ions act as basic sites and can interact with acceptors such as H^+. One of the most common dissociative reactions on metal oxide surfaces is the deprotonation of an adsorbate to produce surface hydroxyl groups. Another important feature of adsorption on metal oxides is the involvement of lattice oxygen atoms. The basic nature of lattice oxygen atoms compared to acidic molecules such as CO_2 often leads to the formation of surface CO_3^{2-} [1]. Furthermore, metal oxides can also interact with adsorbates via oxidation/reduction, or redox, reactions. In a redox reaction there is a change in the oxidation state of the adsorbate, with the release or capture of electrons. Examples are the reaction of H to form H^+ and that of Cl to Cl^-. For mechanistic surface studies of molecular adsorption on metal oxides, three strategies have been applied [67]:

1. adsorption and reaction studies on microcrystalline materials that are composed of crystals of microscopic size (having maximum dimensions of one micron), e.g. by Marchese et al. [68] and Zaki et al. [69],
2. adsorption studies on surfaces of single crystal oxides, e.g. by the Yale [1], Kopenhagen [59, 60] and Manchester [70] groups,
3. adsorption and reaction studies on thin oxide single crystal films growing on metallic substrates, e.g. by Goodman [71, 72], Somorjai [73] and Freund [74, 75] groups.

The third strategy has been proven to be especially useful since most modern electron spectroscopic techniques can be applied in these studies.

Knowledge about molecular adsorption on metal oxide surfaces and the alteration of surface properties resulting from adsorbate-surface interactions is critical for a better understanding of many technological processes. For instance, the interaction of water with metal oxide surfaces has direct impact on catalysis [1, 3], corrosion [6, 76, 77], and metallization [78, 79]. Depending on the system, adsorbed water may be present as a molecule or it may dissociate. As an adsorbed molecule, it may bind to the surface by electrostatic interaction, charge transfer or hydrogen bonding. The water molecule can be very inert on some surfaces, while on others it may oxidize the surface or near-surface regions [8]. A main objective in studying water-surface interactions is to determinie whether water is molecularly vs. dissociatively adsorbed, since the presence or absence of dissociation has significant implications for many chemical processes. The chemical reactivities of water dissociation products are very different from that of water. There are essentially two thermal reaction pathways by which water can dissociate on a solid surface. In the first case, water dissociates, but thermodynamics (and kinetics under UHV conditions) favor recombination of fragments to liberate water [8]:

$$H_2O_{(a)} \rightarrow OH_{(a)} + H_{(a)} \rightarrow H_2O_{(g)} \quad \text{(reversible dissociation)} \qquad (1\text{-}5)$$

In the second one, water dissociates, but thermodynamics favor surface oxidation, the most common irreversible pathway, over recombination of fragments to water:

$$H_2O_{(a)} \rightarrow OH_{(a)} + H_{(a)} \rightarrow O_{(a)} + H_{2(g)} \quad \text{(irreversible dissociation)} \qquad (1\text{-}6)$$

Reversible water dissociation is typically observed on oxide surface, while irreversible water dissociation is typically observed on metal and semiconductor surfaces [8]. It has been long believed that water dissociation on most oxide surfaces is enhanced by the

presence of defect sites. Defect sites are usually highly undercoordinated, which makes them more acidic, and thus more energetically favorable binding sites for water. In addition, a wide variety of structural arranges of cation and anion sites offered by defects is particularly important for water dissociation because this process requires the concerted effort of a cation site binding water and an anion site abstracting a proton. Water adsorption on alumina surfaces at room temperature is reported to be dissociative by previous studies [80, 81]. Dissociative chemisorption of water and the formation of a hydroxide phase is only observed for water vapor pressure above 1 Torr for α-Al_2O_3(0001) and dissociative chemisorption of water occurs mainly at defect sites below this pressure [78, 82]. Both transitional phase (non-α) and α-phase (e.g., sapphire(0001)) surfaces are inert towards H_2O vapor at UHV pressures [10, 43, 46] because for all alumina phases in UHV, bulk-terminated surface cations undergo a strong inward relaxation, effectively shielding these reactive sites within the larger oxygen anion sublattice [41, 43] as shown in Fig. 1.2. XPS data [46] obtained for a thin alumina film grown on Ni_3Al(110), however, strongly suggested that the oxide film was structurally unstable upon exposure to P_{H_2O} of ~ 10^{-4} Torr, 300 K, even though aluminum hydroxide was only observed after exposures to P_{H_2O} ~ 1 Torr, 300 K.

Recently, there has been considerable interest in *cooperative* surface interaction, that is, reactions involving two or more adsorbate molecules reacting at a single surface site [83, 84]. A*b initio* studies indicate that cooperative effects strongly affect the properties of certain adsorbate molecules (e.g. H_2O) [85, 86]. It is now well established

that cooperative effects strongly favor molecules with hydrogen bond (HB) patterns in which each molecule is simultaneously a proton donor and an acceptor of HBs [86, 87].

The cooperative surface interaction is particularly relevant to alumina surface chemistry since molecular dynamics (MD) studies [88] indicate that *cooperative* surface reactions involving several H_2O molecules may be responsible for the surface hydroxylation observed at high pressures. UHV, which is required to keep atomically

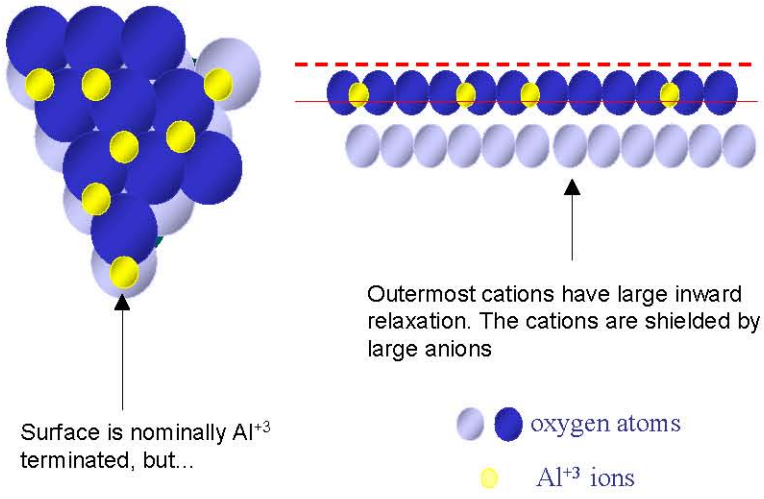

Fig. 1.2. Alumina surface in UHV: relaxation of surface cations reduces reactivity.

clean surfaces, however, precludes observation of many *cooperative* surface interactions, as the following rough calculation shows. From the kinetic theory of gases, the flux (F) of molecules to the surfaces (in terms of atoms/cm^2·sec) at a given pressure P is [16]:

$$F = 3.51 \times 10^{22} \frac{P(torr)}{\sqrt{M(g/mole)T}} \qquad (1\text{-}7)$$

where T is temperature, and M is the average molecular weight of the gas/surface species. Thus, most gas/surface experiments involve changes in surface composition as a function of exposure (= P× time), since this gives the number of single-molecule/surface interactions. The most common unit of exposure is the Langmuir (L; 1L = 10^{-6} torr · sec). Substituting P = 3 × 10^{-6} torr and using the values of M = 28 g/mol and T = 300 K in Eqn. (1-7), we can see that F ≈ 10^{15} molecules/cm^2/sec.

The residence time (τ) for a molecule on a surface is related to the heat of adsorption (ΔH_{ads}) by [16]

$$\tau = \tau_0 \exp(\frac{\Delta H_{ads}}{RT}) \qquad (1\text{-}8)$$

where τ_0 is correlated with surface atom vibrational time. T is the temperature and R is the gas constant. A typical value for τ_0 is 10^{-12} sec [16]. Assuming the heat of adsorption is equal to the heat of desorption obtained from temperature programmed desorption (TPD), ΔH_{ads} for H_2O on the surface of 5 Å thick Al_2O_3/NiAl(110) is 43 KJ/mol [89]. The average surface coverage (θ) of adsorbed molecules on an initially clean surface is determined by the product of the incident flux F and the residence time τ:

$$\theta = F\tau \qquad (1\text{-}9)$$

At 300 K and a partial pressure of water vapor (P_{H_2O}) of 10^{-9} Torr, $\theta_{H_2O} \approx 10^{-8}$ Monolayer (ML). At such low coverage, *cooperative* surface interaction is not possible. MD calculations [88] indicate that H_2O dissociation is stabilized by adjacent H_2O molecules, which may provide a substantial probability for H_2O-H_2O *cooperative* surface

interactions at $P_{H_2O} > 10^{-5}$ Torr. Such a bimolecular dissociation mechanism at the α-Al_2O_3(0001) surface from reference [88] is shown schematically in Fig. 1.3. Cooperative interactions are obviously possible at $P_{H_2O} > 1$ Torr, when hydroxide formation is observed [82].

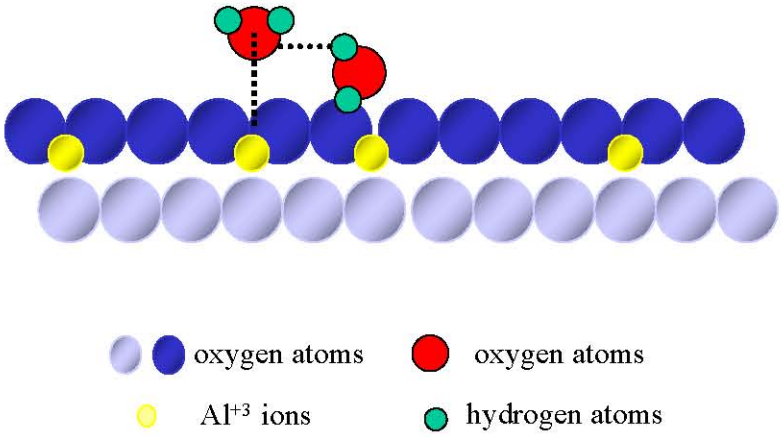

Fig. 1.3. A bimolecular H_2O dissociation mechanism at the α-Al_2O_3(0001) surface: H_2O dissociation stabilized by adjacent H_2O molecule.

1.2. Experimental Methodology

Reactions occurring at solid surfaces are of great importance particularly for practical applications. A surface can be envisaged as the result of a fracture along a certain plane in the bulk material, where the bonds between neighboring atoms are simply severed. The change in the equilibrium position and bonding of surface atoms can cause drastic reconstruction of the outermost layers, i.e., the surface can assume a fundamentally different atomic structure from that of the bulk material [16, 90, 91]. The surface has a strong tendency to interact chemically with particles from the gas phase because of the more or less unsaturated valencies. In order to study atomically clean

surfaces, it is clearly necessary to keep the pressure of the residual gas above the surface very low, which requires ultra high vacuum (UHV). The concentration of atoms on the surface of a solid is on the order of 10^{15} cm^{-2} [16]. A rough calculation indicates that at a pressure of 10^{-6} torr, the surface will be covered with a monolayer of adsorbate within a second at room temperature assuming that every molecule that strikes the surface sticks (i.e., the sticking coefficient is 1). For this reason, the unit of gas exposure is 10^{-6} torr-sec, which is called a langmuir (L). Current surface techniques can detect contamination on the order of 1% of a monolayer. In order to keep an atomically clean surface for at least an hour, often the time scale needed to perform one experiment, working pressure $\leq 10^{-9}$ torr (so-called ultra high vacuum (UHV) conditions) must be regularly attained [16].

A number of UHV-based surface analytical techniques were employed in this research: Auger electron spectroscopy (AES) and X-ray photoelectron spectroscopy (XPS) were employed in surface composition analysis; low-energy electron diffraction (LEED) and scanning tunneling microscopy (STM) were used to characterize the surface structure and topography; and scanning tunneling spectroscopy (STS) was utilized in the study of surface electronic states. The principles of operation for each technique are discussed as follows.

1.2.1. Auger Electron Spectroscopy (AES)

Auger Electron Spectroscopy (*Auger spectroscopy* or AES) was developed in the late 1960's, deriving its name from the effect first observed by Pierre Auger, a French Physicist, in the mid-1920's. AES is a popular method for analysis of surfaces, thin films,

and interfaces. It cannot detect hydrogen or helium, but is sensitive to all other elements, being most sensitive to the low atomic number elements. Auger electron spectroscopy (AES) identifies elemental compositions of surfaces by measuring the energy of Auger electrons. The surface sensitivity of AES is due to the low energy of these electrons ($E \leq 1000$ eV). Electrons in this energy range interact with solid matter very strongly; as a result, their inelastic mean free paths within solid are only a few atomic layers, making AES a suitable technique for surface analysis [92, 93].

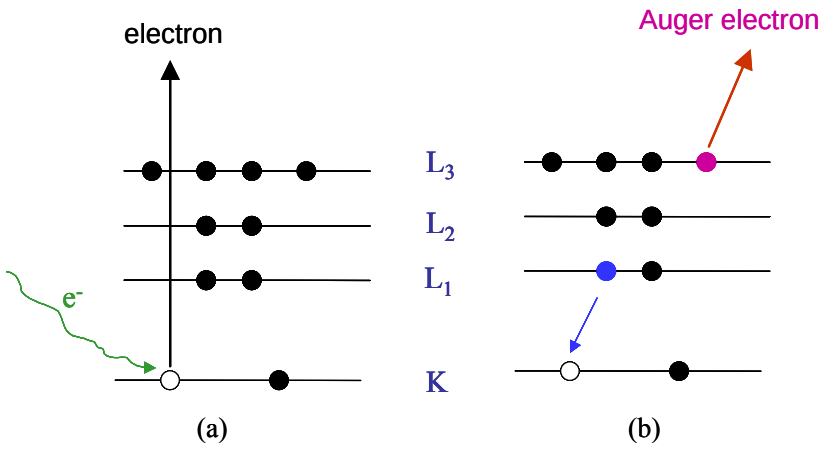

Fig. 1.4. Schematic of Auger process: (a) removal of a core electron; (b) Auger electron emission.

The Auger emission process involves three electrons as shown in. Fig. 1.4. The basic Auger process starts with removal of an inner shell (core level) atomic electron to form a vacancy by bombarding the sample with an electron beam. A second atomic electron falls from a higher shell to fill the inner shell vacancy. Energy must be

simultaneously released. Therefore, a third electron, the Auger electron, escapes carrying the excess energy in a radiationless process. Auger electrons are classified according to the energy levels in the atom that are involved in their production. Therefore, the Auger transition in Fig. 1.4. is labeled as KL_1L_3, where the initial hole is given first, followed by the locations of the final two holes in order of decreasing binding energy.

The kinetic energy (K.E.) of Auger electrons in the above example is approximated by:

$$K.E. = (E_K - E_{L1}) - E_{L3} \tag{1-10}$$

where E_K, E_{L1}, and E_{L3} are electron binding energies at K, L_1, and L_3 levels, respectively. Since K.E. is independent of the formation mechanism of the initial core hole, X-rays can also be used to induce Auger electrons.

Auger spectra are generally analyzed and presented in a differentiated form. In the integrated mode, Auger electron transitions generally appear as small features superimposed on a rather large continuous background of secondary electrons (Fig. 1.5) when the excitation source is an electron beam, therefore, the energy distribution function N(E) is electronically differentiated into dN(E)/dE in order to facilitate easy identification and analysis of the Auger transitions. Each element has Auger electrons with kinetic energies that are characteristic of the atom from which the electrons come. Therefore, the analysis of Auger energies leads to elemental identification. In selected cases, information on chemical binding can be obtained as well from peak position, shape or fine structures. Furthermore, the surface concentration of an element can be derived from the peak-to-peak height (PPH) in the derivatized Auger spectrum [90].

1.2.2. Low Energy Electron Diffraction (LEED)

Low energy electron diffraction (LEED) is the principal technique used for the determination of the long-range order of surface structures. LEED utilizes the wave-particle duality nature of electrons, by which an electron beam can be regarded as a group

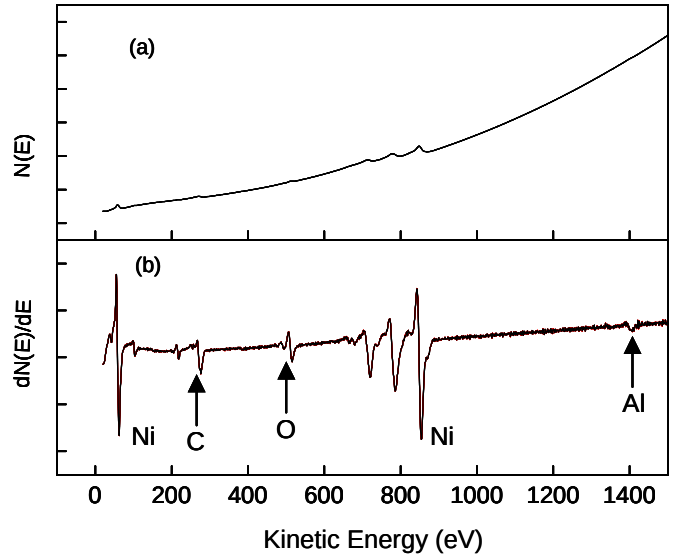

Fig. 1.5. Auger spectra from a contaminated Ni_3Al sample in the (a) integrated and (b) differentiated modes.

of particles, and also as a series of waves incident upon the target material. Using the de Broglie relation, the wavelength (λ) of the incident electron beam can be expressed as [16]:

$$\lambda = \sqrt{\frac{150}{E(eV)}} \qquad (1\text{-}11)$$

Electrons that have been accellerated through a potential of 20 to 200 volts (i.e., their kinetic energy is around 20 to 200 eV) have a wavelength given by the de Broglie relation (Eqn. 1-11) which varies from 2.7 Angstroms to 0.9 Angstroms. This corresponds to the range of distances between atoms in solids and can therefore strongly diffract from them. The LEED experiment, therefore, uses a beam of electrons of a well-defined low energy (typically in the range 20 - 200 eV) incident normal to the sample in order to satisfy the atomic diffraction condition (λ must be smaller than or comparable to the interatomic spacing).

Surface atoms scatter incident electrons in all directions. In some of these directions the scattered beams are in phase and reinforce each other to give diffracted beams i.e. constructive interference. For convenience, the scattering can be divided into two types: forward scattering where the angle of scattering is $< 90°$, and back scattering that reverses the momentum normal to the surface. In LEED, we are dependent on back scattering for the electrons we observe. Fig. 1.6 schematically illustrates interference between waves scattering from a one-dimensional row of atoms (with atomic separation *a*) in a crystal with the electron beam incident normal to the array. For the two adjacent atoms shown in Fig. 1.6, the path difference between beams is $d = a \sin\theta$. For constructive interference, the path difference must be an integral multiple of the wavelength of the incident electron beam. The result is Bragg's law of diffraction:

$$a \sin\theta = n \lambda \qquad n = 1, 2, 3\ldots \tag{1-12}$$

which is known as the Bragg condition. Depending upon the d and λ, there may be several angles θ for which constructive interference can occur [93]. For a surface with a

two-dimensional array of atoms with primitive interatomic distances of *a* and *b*, the Bragg condition requires both $a\sin\theta_a = n\lambda$ and $b\sin\theta_b = m\lambda$ for constructive interference to occur, i.e. the incoming electrons can only be scattered along a set of lines dispersed from the surface [91, 93, 94].

Fig. 1.7 shows a typical LEED apparatus. The LEED system has two major components: (1) an electron gun producing monochromatic electrons and (2) a detector system which detects only the elastically scattered electrons. The electron gun produces a collimated monoenergetic beam of electrons with specific energy (20 to 200 eV). In a

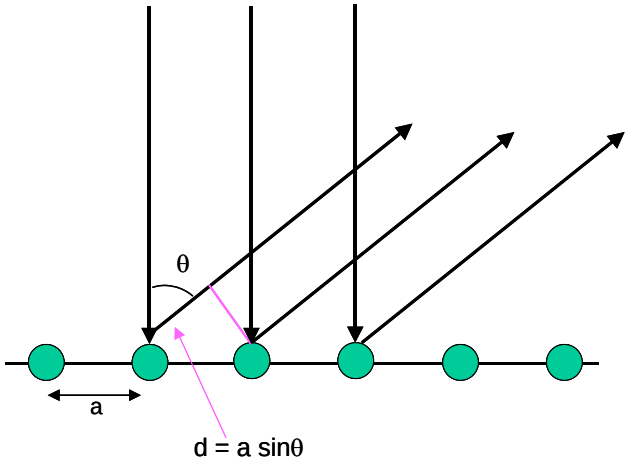

Fig. 1.6. Diffraction of electrons from a one-dimensional array of atoms.

LEED experiment, the beam of collimated monoenergetic electrons is directed toward the sample surface, where a fraction of the incoming low energy electrons is elastically scattered (Fig. 1.7). The sample must be a single crystal with a well-ordered surface structure in order to generate a back-scattered electron diffraction pattern. The detector

consists of four metal grids at different voltages and a fluorescent screen. The first grid (counted from the sample) is at ground potential to ensure a field free region around the

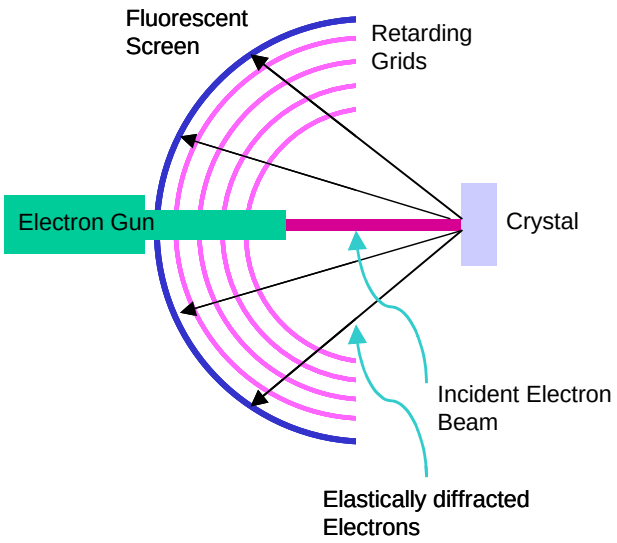

Fig. 1.7. A schematic LEED experiment set-up.

sample. The next two grids are set to the retarding voltage, which is slightly lower than the kinetic energy of the electrons produced by the gun. They repel almost all inelastically scattered electrons. The elastically scattered (diffracted) electrons pass the next grid which is set to ground voltage again and are then accelerated towards the fluorescent screen which is set to a high positive voltage. Bombardment of diffracted electrons onto the screen results in bright spots whose pattern reflects the ordered arrangement of surface atoms by a reciprocal relationship [94, 95].

There are two major applications for LEED. The first one is to provide qualitative information from inspection of the surface diffraction pattern. From one short LEED experiment, we can obtain direct information about the surface order and quality. When the surface is reconstructed or covered with adsorbates, the LEED images can quickly give information about the surface symmetry, periodicities, or rotational alignment of an adsorbate unit cell with respect to the substrate unit cell. The second application of LEED is the quantitative structure determination. In this application, the intensities of the various diffracted beams are recorded as a function of the incident electron beam energy to generate so-called I-V curves which, by comparison with theoretical curves, may provide accurate information on atomic positions. Despite this complicated procedure, LEED is the most important tool for quantitative surface structure determination [1, 94].

1.2.3. Scanning Tunneling Microscopy (STM) and Spectroscopy (STS)

The scanning tunneling microscope (STM) is widely used in both industrial and fundamental research to obtain atomic-scale images of surfaces. It provides a three-dimensional profile of the electronic states of the surface which is very useful for characterizing surface roughness, observing surface defects, and determining the size and conformation of molecules and aggregates on the surface. Binnig and Rohrer developed the first STM in 1981, for which they were awarded the Nobel Prize in 1986 [96, 97].

A schematic drawing of the STM set-up is shown in Fig. 1.8. A bias voltage is applied between an atomically sharp metal tip and an electrically conductive sample to be investigated (metal or doped semiconductor). After the tip is brought into close proximity

(a few angstroms) to the sample surface, a very small tunneling current can flow due to the quantum mechanical tunneling effect, without the need for the probe tip to physically touch the surface. The direction of tunneling current flow is dependent on the polarity of

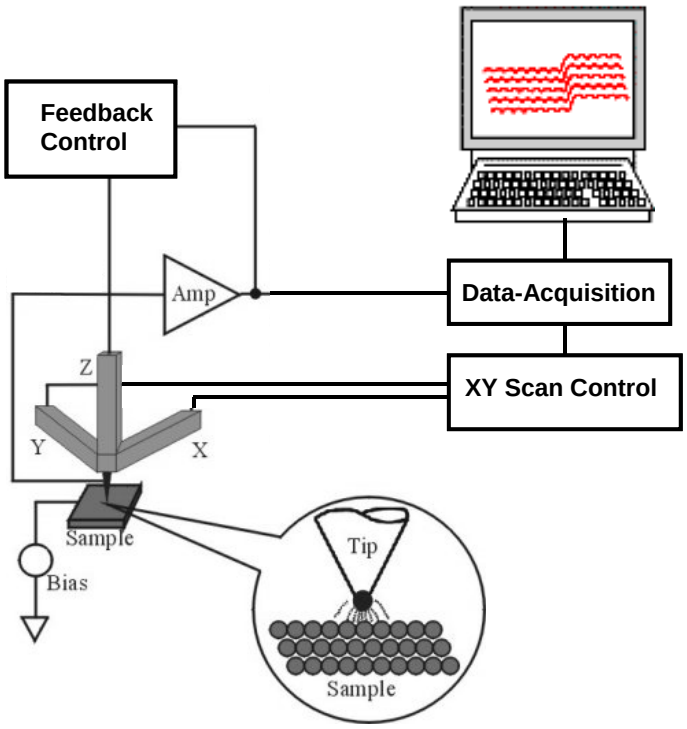

Fig. 1.8. Schematic illustration of basic STM set-up.

the bias: when the sample is negatively biased, electrons will tunnel from the occupied states of the sample into the empty states or conduction band states of the tip; electrons will tunnel from the occupied states of the tip into the empty states or conduction band states of the sample when the sample is positively biased.

At a distance of only a few Å, the overlap of tip and sample electron wave functions is large enough for a tunneling current I_t to occur, which is given by

$$I_t \propto e^{-2\kappa d} \tag{1-13}$$

where d denotes the tip-sample distance and the decay constant for the wave functions in the barrier (κ) is given by $k = \sqrt{2m\Phi}/\eta$, in which Φ is the local barrier height or the effective local work function, and $\eta = h/2\pi$. For metals with typical work functions of 4 eV-5 eV, k is on the order of 1 $Å^{-1}$. Therefore, an increase of the tunneling distance of only 1 Å changes the tunneling currents by about an order of magnitude.

The tunneling current can be used to probe physical properties locally at the sample surface as well as to control the tip-sample separation distance. The magnitude of the tunneling current is very sensitive to any change in the tip-sample separation distance because the tunneling current is exponentially dependent on this separation. It is this sensitivity that makes it possible to monitor and detect changes in the tip-sample separation distance. Motion of the tip (or sample) both laterally and vertically with respect to the sample (or tip) can be controlled with sub-atomic accuracy by means of piezoelectric drives that are mechanically connected to the tip (or sample). Changing the position in the lateral (x,y) plane allows you to scan continuously across the sample surface and changing the vertical (z) position allows you to maintain desired tip-sample distance. STM can be designed to scan a sample in either of two modes: constant height mode (CHM) or constant current mode (CCM) [96].

The most widely used mode of STM operation is CCM (Fig. 1.9a). In CCM, a feedback loop is used to adjust the vertical position of the scanner at each measurement

point to keep the current constant. In practice, the actual tunneling current I_t is compared with a preset constant value (I_0), typically 0.5-5nA, in a feedback circuit. The feedback signal, proportional to the difference between I_t and I_0, provides a correction voltage to the z piezoelectric drive and thus causes the tip-sample distance to change when a protrusion or a depression is traversed. For example, when the feedback loop detects an increase in tunneling current ($I_t > I_0$), it adjusts the voltage applied to the z piezoelectric drive to increase the distance between the tip and the sample. The measured quantity in this mode is the voltage required to move the tip up and down (z voltage) to maintain the constant current. Recording the *z* voltage as a function of the lateral tip position during raster scanning yields a map of the surface topography. The advantage of CCM is that large areas can be scanned while the disadvantage is that the resolution is low compared to the CHM [96].

In the CHM (Fig. 1.9b), the tip-sample separation is kept constant by holding the z-coordinate constant, equivalent to a slow or disabled feedback, and the current is recorded over each point. Since the tunneling current (I_t) changes exponentially with tip-sample distance, corrugations or depressions in the sample surface will give rise to variations in the current as the tip is scanned across the surface in this mode. That is, the tunneling current tends to decrease as the separation between the tip and the surface atoms increases and vice versa. Therefore, the current as a function of lateral position represents a topography image of the sample surface. This mode is only appropriate for atomically flat surfaces, as otherwise a tip crash would be inevitable [96].

At a first approximation, interpretation of the STM image as a surface topograph is generally adequate. More accurately, scanning tunneling spectroscopy (STS) performed in STM provides information about the local electronic structure of the sample by probing the density of states (DOS) at the sample surface as a function of energy. In general, STS is carried out in the middle of an STM image acquisition so that atom-resolved probing of spectroscopic signals can be achieved. There are several ways of

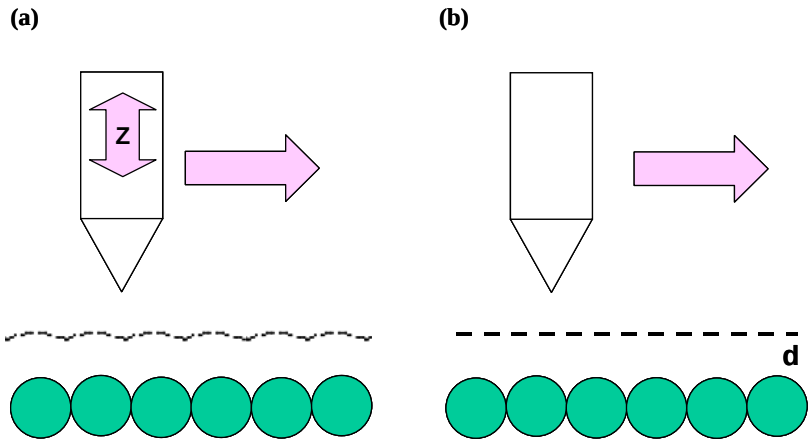

Fig. 1.9. Scanning modes for STM: (a) constant current mode; (b) constant height mode.

obtaining the STS information, including topography imaging at different applied potentials, current imaging at different heights, *I-V* (or *dI/dV-V*) data acquisition as a modulation of the potential, Z/V curve (tip-sample separation vs. bias voltage in constant current mode), and I/Z curve (tunneling current vs. tip-sample separation in constant bias mode) [98].

The *I-V* curve (tunneling current vs. bias voltage in constant height mode) is the most common STS method. It can be obtained over an averaged large region or at a selected location (single point), which correlates the surface topography with the local electronic structure. To obtain an I/V curve, the actual scan is stopped and the tip is moved to the desired position with the feedback loop closed. By interrupting (switching off) the feedback loop and keeping a fixed tip-sample separation, a voltage ramp is applied and the tunneling current is recorded. The resulting I-V curve is characteristic of the electronic structure at a specific x,y location on the sample surface. For the interpretation of the spectroscopic data the normalized differential conductivity of the measured I-V curves ((dI/dV)/(I/V)) is calculated. This quantity carries information about the local DOS of the sample [96, 98].

The invention of STM heralded a new era in surface science in which the structure and topography of surfaces could be imaged down to atomic dimensions. The operation of STM relies on the electrical conductivity of the sample. Therefore, both imaging and spectroscopic (STS) aspects of the technique could be immediately exploited in the study of metals and semiconductors. Nevertheless, it has been demonstrated that STM studies on the oxide surfaces are practical, if the material can be made sufficiently bulk conducting (like TiO_2) [99]. Another approach, as pointed out in section 1.1.1, is the use of thin oxide films on the metallic substrates. In this case, we have to discriminate between two situations as illustrated in Fig. 1.10 using potential diagrams, due to the band gap of the oxide [3].

When imaging at low bias voltages V_{bisa}, only electronic states located close in energy to the metal substrate Fermi level are accessible, whereas the electronic states of the oxide are not accessible. Under this tunneling condition, therefore, electron can only tunnel between the tip and the metal substrate, with the oxide acting as a tunneling barrier. Generally speaking, at low bias voltages, STM is more sensitive to the

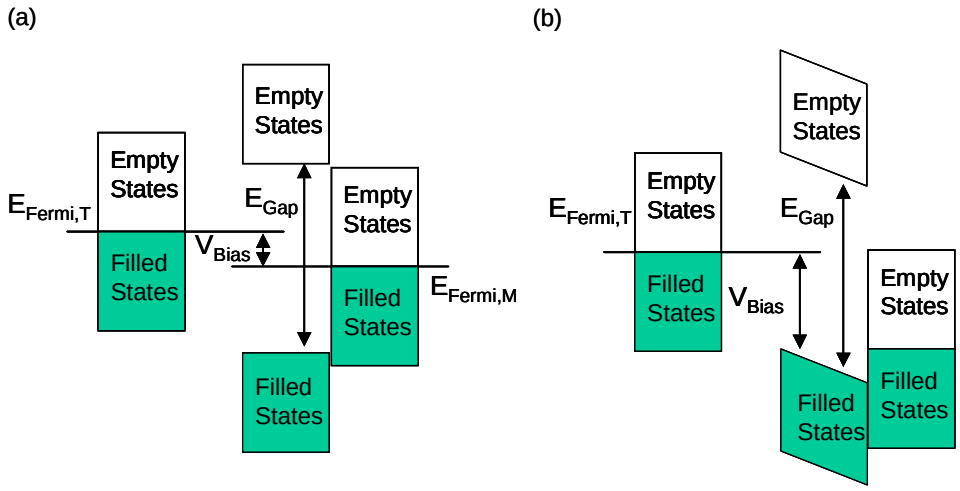

Fig. 1.10. The potential diagrams illustrate the different tunneling condition when imaging a thin oxide film on metallic substrate: (a) low bias voltage; (b) high bias voltage.

film/substrate interface. In contrast, imaging at high bias voltage (higher than ½ of the band gap of the oxide) involves tunneling between oxide valence (filled states) or conduction (empty states) band states located further from the Fermi surfaces [3]. STM images obtaining under this condition reflect accurately the topography of the oxide overlayer. This effect has been previously demonstrated for ultrathin films of $Al_2O_3/Ni_3Al(111)$ [100], $Al_2O_3/Ni_3Al(110)$ [101] and $SiO_2/Si(111)$ [102].

1.2.4. X-Ray Photoelectron Spectroscopy (XPS)

X-ray photoelectron spectroscopy (XPS), also known as ESCA (electron spectroscopy for chemical analysis), is a surface sensitive non-destructive technique that provides quantitative surface chemical state information for all elements except hydrogen and helium. XPS was developed in the mid 1960s by K. Siegbahn and his research group [103]. Siegbahn was awarded the Nobel Prize for Physics in 1981 for his work in XPS. The principle behind the XPS technique is the photoelectric effect, i.e. the sample is illuminated with X-ray photons that result in the ejection of photoelectrons from the surface. The photoemission process is illustrated in Fig. 1.11. In XPS, when a beam of X-rays strikes a sample surface, the energy of the X-ray photon is adsorbed completely by the core electron of an atom, leading to ionization and the emission of a core (inner shell) electron. The kinetic energy (KE) of the ejected photoelectron is determined by the energy of the x-ray radiation, $h\nu$, the electron binding energy, E_B, and the work function of the spectrometer (a constant for a given analyzer),Φ_s, as given by [90]:

$$KE = h\nu - E_B - \Phi_s \qquad (1\text{-}14)$$

By measuring the kinetic energy of the photoelectron, the binding energy can be determined using Eqn. (1-14).

For every element, there will be a characteristic binding energy associated with each core atomic orbital. In other words, each element has a characteristic set of binding energies. The spectrum from a mixture of elements is approximately the sum of the peaks of the individual constituents. Therefore, XPS is a powerful tool to identify and determine the atomic compositions of a sample. In addition, the binding energy of an

electron is particularly sensitive to the chemical environment through a "chemical shift" effect. The chemical shift can arise for several reasons: difference in formal oxidation state, difference in local chemical and physical environment and so on. It gives rise to small shifts (~ 0.1 eV-10 eV) in the binding energy of an electron. For example, atoms of

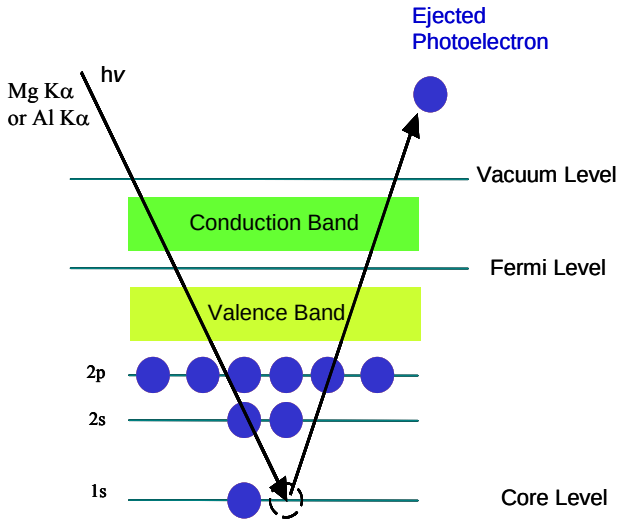

Fig. 1.11. Photoemission process for one electron model in a solid.

a higher positive oxidation state exhibit a higher binding energy due to the extra coulombic interaction between the photo-emitted electron and the ion core. As a result, variation in the elemental binding energies (the chemical shifts) allows for a determination of the chemical state of certain elements. The ability to discriminate between different oxidation states and chemical environments is one of the major strengths of the XPS technique. Furthermore, the intensity of the XPS peak is associated with the concentration of the element within the sampled region. Thus, the technique is capable of yielding a quantitative analysis [90].

A typical X-ray photoelectron spectrometer is displayed in Fig. 1.12 [90]. It is composed of an X-ray source, electron energy analyzer, electron detector, and a recorder. The X-ray source consists of an anode of a suitable material (Mg and/or Al), which is bombarded by energetic electrons that are emitted from the cathode. An electron analyzer measures the kinetic energy distribution of the emitted photoelectrons. The concentric hemispherical analyzer (CHA) consists of a lens, entrance slit, two concentric hemispheres held at negative voltages, and an exit slit (Fig. 1.12). The function of the lens is two-fold. First, it focuses photoelectrons emitted from the substrate onto the entrance slit to the analyzer. Secondly, it retards the photoelectrons to a constant kinetic energy known as the pass energy. The pass energy is proportional to the difference in voltage between the two hemispheres. Only electrons with a kinetic energy equal to the pass energy will get through the analyzer. By retarding the electrons to a constant kinetic energy, a fixed resolution is applied across the entire spectrum.

The incident X-Rays used in ejecting the electrons must possess energy that is both monochromatic and of accurately known. The X-ray source material must also be a light element since X-ray line widths, which must be as narrow as possible in ESCA, are proportional to the atomic number of the source material. It is for these reasons that commercial XPS systems typically use the Kα X-rays of aluminum (Al Kα E = 1.487 keV) and magnesium (Mg Kα E = 1.254 keV). The emitted photoelectrons will therefore have kinetic energies in the range of 0 - 1480 eV or 0 - 1250 eV, respectively. Although the X-rays penetrate deep into the sample, only the electrons on the surface of the sample are able to escape without significant loss of energy for analysis, since such

electrons have very short inelastic mean free path (IMFP) in solids. As such, XPS is necessarily a surface-sensitive technique with analysis depths typically below 10 nm. XPS is capable of detecting chemical species down to ~1% of the surface concentration. XPS experiments must be conducted under UHV (<10^{-9} Torr) to avoid attenuation of radiation and scattering of electrons in the gas phase [90].

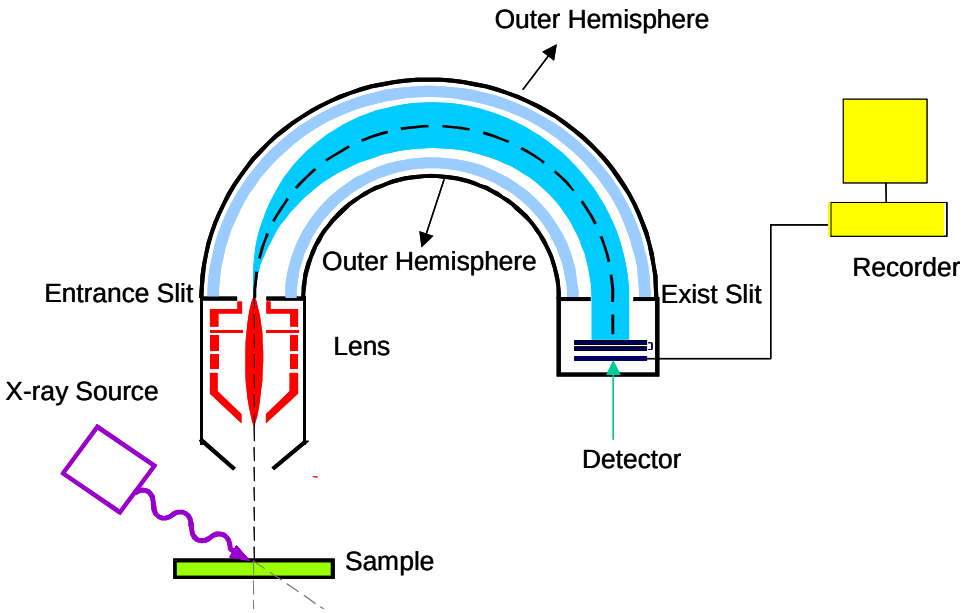

Fig. 1.12. Schematic drawing of a XPS spectrometer with a concentric hemispherical analyzer.

1.3. Chapter References

[1] Henrich, V. E. and Cox, P. A., The Surface Science of Metal Oxides, Cambridge University Press, New York, 1994.

[2] Ernst, F., *Mat. Sci. Eng.*, **R14**, 97 (1995).

[3] Bäumer, M. and Freund, H.-J., *Prog. Surf. Sci*, **61**, 127 (1999).

[4] Street, S. C., Xu, C. and Goodman, D. W., *Annu. Rev. Phys. Chem.*, **48**, 43 (1997).

[5] Strongin, D. R., Bare, S. R. and Somorjai, G. A., *J. Catal.*, **103**, 289 (1987).

[6] Smialek, J. L. and Morscher, G. N., *Mater. Sci. Eng. A*, **332**, 11 (2002).

[7] Guinn, K. V., Donnelly, V. M., Gross, M. E., Baiocchi, F. A., Petrov, I. and Greene, J. E., *Surf. Sci*, **295**, 219 (1993).

[8] Henderson, M. A., *Surf. Sci. Rep.*, **46**, 1 (2002).

[9] Freund, H.-J., Baumer, M., Libuda, J., Risse, T., Rupprechter, G. and Shaikhutdinov, S., *J. Catal.*, **216**, 223 (2003).

[10] Elam, J. W., Nelson, C. E., Cameron, M. A., Tolbert, M. A. and George, S. M., *J. Phys. Chem. B*, **102**, 7008 (1998).

[11] Gassman, P., Franchy, R. and Ibach, H., *Surf. Sci.*, **319**, 95 (1994).

[12] Hsiao, G., Erley, W. and Ibach, H., *Surf. Sci.*, **405**, L465 (1998).

[13] Goodman, D. W., *J. Vac. Sci. Technol. A*, **14**, 1526 (1996).

[14] Olivier, J. and Poirier, R., *Surf. Sci.*, **105**, 347 (1981).

[15] Goodman, D. W., *Surf. Sci.*, **299-300**, 837 (1994).

[16] Somorjai, G. A., Introduction to Surface Chemistry and Catalysis, John Wiley & Sons Ltd, New York, 1994.

[17] Chen, L., Magtoto, N. P., Addepali, S., Ekstrom, B. and kelber, J. A., *Oxid. Met.*, **54**, 285 (2000).

[18] Addepalli, S. G., Magtoto, N. P. and Kelber, J. A., *Langmuir*, **16**, 8352 (2000).

[19] Addepalli, S. G., Magtoto, N. P. and Kelber, J. A., *Surf. Sci.*, **458**, 123 (2000).

[20] Lad, R. J., *Surf. Rev. Lett.*, **2**, 109 (1995).

[21] Sullivan, J. P., Dunn, R. G., Barbour, J. C., Wall, F. D., Missert, N. and Buchheit, R. G., K. R. Hebert, R. S. Lillard and B. R. MacDougall, Oxide Films, Toronto, Canada, 2000, Electrochemical Society, Inc., 2000-4 (2000) 24.

[22] Schedel-Niedrig, T., Weiss, W. and Schlogl, R., *Phys. Rev. B*, **52**, 17449 (1995).

[23] Park, B. G. and Lee, T. D., *IEEE Trans. Magn.*, **35**, 2919 (1999).

[24] Miyazaki, T. and Tezuka, N., *J. Magn. Magn. Mater.*, **139**, L231 (1995).

[25] Kolodzey, J., Chowdhury, E. A., Adam, T. N., Qui, G., Rau, I., Olowolafe, J. O., Suehle, J. S. and Chen, Y., *IEEE Trans. Electron Devices*, **47**, 121 (2000).

[26] Fauer, G., Principles and Applications of Inorganic Geochemistry, MavMillan, New York, 1991.

[27] Jones, D. A., Principles and Preventions of Corrosion, Macmillan Publishing Company, New York, 1991.

[28] Scully, J. C., The Fundamentals of Corrosion, Pergamon Press, New York, 1990.

[29] Kubaschewski, O. and Hopkins, B. E., Oxidation of Metals and Alloys, Butterworth and Co. Ltd., Northern Ireland, 1962.

[30] Rae, A. U. M., *Surf. Sci.*, **1**, 319 (1964).

[31] Fontana, M. G., Corrosion Engineering, McGraw-Hill, Inc., New York, 1986.

[32] Fan, J. C. C. and Henrich, V. E., *Appl. Phys. Lett.*, **25**, 401 (1974).

[33] Franchy, R., *Surf. Sci. Rep.*, **38**, 195 (2000).

[34] Jacobsson, J. R., Thin Film Technologies, SPIE, Bellingham, WA, 1983.

[35] Anders, S., Anders, A., Rubin, M., Wang, Z., Raoux, S., Kong, F. and Brown, I. G., *Surf. Coat. Technol*., **76-77**, 167 (1995).

[36] Anast, M., Jamting, Å., Bell, J. M. and Ben-Nissan, B., *Thin Solid Films*, **253**, 303 (1994).

[37] Huo, D. T. C., Yan, M. F. and Foo, P. D., *J. Vac. Sci. Technol. A*, **9**, 2602 (1991).

[38] Lucovsky, G., Richard, P. D., Tsu, D. V., Lin, S. Y. and Markunas, R. J., *J. Vac. Sci. Technol. A*, **4**, 681 (1986).

[39] Tsuji, M., Sakumoto, M., Itoh, N., Obase, H. and Nishimura, Y., *Appl. Surf. Sci.*, **51**, 171 (1991).

[40] Vurens, G. H., Salmeron, M. and Somorjai, G. A., *Prog. Surf. Sci.*, **33**, 333 (1990).

[41] Jaeger, R. M., Kuhlenbeck, H., Freund, H.-J., Wuttig, M., Hoffmann, W., Franchy, R. and Ibach, H., *Surf. Sci.*, **259**, 235 (1991).

[42] Libuda, J., Winkelmann, F., Bäumer, M., Freund, H.-J., Bertrams, T., Neddermeyer, H. and Müller, K., *Surf. Sci.*, **318**, 61 (1994).

[43] Libuda, J., Frank, M., Sandell, A. and Freund, H.-J., *Surf. Sci.*, **384**, 106 (1997).

[44] Blum, R.-P., Ahlbehrendt, D. and Niehus, H., *Surf. Sci.*, **396**, 176 (1998).

[45] Qin, F., Magtoto, N. P., Kelber, J. A. and Jennison, D. R., *J. Molec. Catal. A*, **228**, 83 (2005).

[46] Garza, M., Magtoto, N. P. and Kelber, J. A., *Surf. Sci.*, **519**, 259 (2002).

[47] Addepalli, S. G., Ekstrom, B., Magtoto, N. P., Lin, J.-S. and Kelber, J. A., *Surf. Sci.*, **442**, 385 (1999).

[48] Bardi, U., Atrei, A. and Rovida, G., *Surf. Sci.*, **268**, 87 (1992).

[49] Cotterill, G. F., Niehus, H. and O'Connor, D. J., *Surf. Rev. Lett.*, **3**, 1355 (1996).

[50] Becker, C., Kandler, J., Raaf, H., Linker, R., Pelster, T., Draeger, M., Tanemura, M. and Wandelt, K., *J. Vac. Sci. Technol. A*, **16**, 1000 (1998).

[51] Qin, F., Magtoto, N. P. and Kelber, J. A., *Surf. Sci.*, **565**, L277 (2004).

[52] Rosenhahn, A., Schneider, J., Becker, C. and Wandelt, K., *Appl. Surf. Sci.*, **142**, 169 (1999).

[53] Kizilkaya, O., Hite, D. A., Zehner, D. M. and Sprunger, P. T., *Surf. Sci.*, **529**, 223 (2003).

[54] Xu, C.-H., Gao, W. and He, Y.-D., *Scripta Mater*, **28**, 975 (2000).

[55] Graupner, H., Hammer, L., Heinz, K. and Zehner, D. M., *Surf. Sci.*, **380**, 335 (1997).

[56] Schmitz, G., Gassmann, P. and Franchy, R., *J. Appl. Phys.*, **83**, 2533 (1998).

[57] Eumann, M., Schmitz, G. and Franchya, R., *Appl. Phys. Lett.*, **72**, 3440 (1998).

[58] Diebold, U., Pan, J. M. and Madey, T. E., *Phys. Rev. B*, **47**, 3868 (1993).

[59] Wu, M.-C. and Møller, P. J., *Surf. Sci.*, **224**, 250 (1989).

[60] Møller, P. J. and Wu, M.-C., *Surf. Sci.*, **224**, 265 (1989).

[61] Dake, L. S. and Lad, R. J., *Surf. Sci.*, **289**, 297 (1993).

[62] Zhong, Q. and Ohuchi, F. S., *J. Vac. Sci. Technol. A*, **8**, 2107 (1990).

[63] Betrabet, H. S., Reddy, S. N. S. and Pureshothaman, S., *Ceramic Eng. Sci. Proc.*, **10**, 1531 (1989).

[64] Parmaliana, A., Arena, F. and Frusteri, F., *J. Chem. Soc. Faraday Trans.*, **86**, 2663 (1990).

[65] Imaduddin, S. and Lad, R. J., *Surf. Sci.*, **290**, 35 (1990).

[66] Woodruff, D. P. and Delchar, T. A., Modern Techniques of Surface Science, Cambrige University Press, New York, 1994.

[67] Freund, H.-J., Dillmann, B., Seiferth, O., Klivenyi, G., Bender, M., Ehrlich, D., Hemmerich, I. and Cappus, D., *Catal. Today*, **32**, 1 (1996).

[68] Marchese, L., Coluccia, S., Martra, G. and Zecchina, A., *Surf. Sci.*, **269**, 135 (1992).

[69] Zaki, M. I. and Knözinger, H., *J. Catal.*, **119**, 311 (1989).

[70] Condon, N. G., Murray, P. W., Leibsle, F. M., Thornton, G., Lennie, A. R. and Vaughan, D. J., *Surf. Sci.*, **310**, L609 (1994).

[71] Wu, M., Estrada, C. A. and Goodman, D. W., *Phys. Rev. Lett.*, **67**, 2910 (1991).

[72] Wu, M., Truong, C. and Goodman, D. W., Adsorption on Ordered Surfaces of Ionic Solids and Thin Films, Vol. 33, Springer Verlag, Heidelberg, 1993.

[73] Weiss, W., Barbieri, A., Hove, M. A. V. and Somorjai, G. A., *Phys. Rev. Lett.*, **71**, 1848 (1993).

[74] Lemire, C., Meyer, R., Henrich, V. E., Shaikhutdinov, S. and Freund, H.-J., *Surf. Sci.*, **572**, 103 (2004).

[75] Carlsson, A. F., Naschitzki, M., Bäumer, M. and Freund, H.-J., *Surf. Sci.*, **545**, 143 (2003).

[76] Janakiraman, R., Meier, G. H. and Pettit, F. S., *Metall. and Mater. Trans. A*, **30A**, 2905 (1999).

[77] Maris-Sida, M. C., Meier, G. H. and Pettit, F. S., *Metall. and Mater. Trans. A*, **34A**, 2609 (2003).

[78] Niu, C., Shepherd, K., Martini, D., J.Tong, Kelber, J. A., Jennison, D. R. and Bogicevic, A., *Surf. Sci.*, **465**, 163 (2000).

[79] Kelber, J. A., Niu, C., Shephed, K., Jennison, D. R. and Bogicevic, A., *Surf. Sci.*, **446**, 76 (2000).

[80] Chen, J. G., Crowell, J. E. and J. T. Yates, J., *Phys. Rev. B*, **33**, 1436 (1986).

[81] Frederick, B. G., Apai, G. and Rhodin, T. N., *Surf. Sci.*, **244**, 67 (1991).

[82] Liu, P., Kendelewicz, T., G. Brown, J., Neslon, E. J. and Chambers, S. A., *Surf. Sci.*, **417**, 53 (1998).

[83] Giordano, L., Goniakowski, J. and Suzanne, J., *Phys. Rev. Lett.*, **81**, 1271 (1998).

[84] AKagi, K. and Tsukada, M., *Thin Solid Films*, **343-344**, 397 (1999).

[85] Xantheas, S. S. and Dunning, Jr., T. H., *J. Chem. Phys.*, **99**, 8774 (1993).

[86] Xantheas, S. S., *J. Chem. Phys.*, **100**, 7523 (1994).

[87] Masella, M., Gresh, N. and Flament, J.-P., *J. Chem. Soc. Faraday Trans.*, **94**, (1998).

[88] Hass, K. C., Schneider, W. F., Curioni, A. and Andreoni, W., *Science*, **282**, 265 (1998).

[89] Tzvetkov, G., Zubavichus, Y., Koller, G., Schmidt, T., Heske, C., Umbach, E., Grunze, M., Ramsey, M. G. and Netzer, F. P., *Surf. Sci.*, **543**, 131 (2003).

[90] Briggs, D. and Seah, M. P., Pratical Surface Analysis, Vol. 1, John Wiley & Sons Ltd, New York, 1990.

[91] Ertl, G. and Kuppers, J., Low Energy Electrons and Surface Chemistry, VCH Publishers, New York, 1985.

[92] Ertl, G. and Kueppers, J., Low Energy Electrons and Surface Chemistry, Vol. 4, Verlag Chemie, Weinheim, 1974.

[93] Feldman, L. C. and Mayer, J. W., Fundamentals of Surface and Thin Film Analysis, P T R Prentice Hall, Englewood Cliffs, 1986.

[94] Pendry, J. B., Low Energy Electron Diffraction, Academic Press Inc., New York, 1974.

[95] Ohtani, H., Kao, C.-T., Hove, M. A. V. and Somorjai, G. A., *Prog. Surf. Sci.*, **23**, 155 (1986).

[96] Wiesendanger, R., Scanning Probe Microscopy and Spectroscopy: Methods and Applications, Cambridge University Press, Cambridge, 1994.

[97] Binning, G., Rohrer, H., Gerber, C. and Weibel, E., *Phys. Rev. Lett.*, **49**, 57 (1982).

[98] Feenstra, R. M., *Surf. Sci.*, **299-300**, 965 (1994).

[99] Bownell, D. A., *Prog. Surf. Sci.*, **57**, 187 (1998).

[100] Magtoto, N. P., Niu, C., Anzaldua, M., Kelber, J. A. and Jennison, D. R., *Surf. Sci.*, **472**, L157 (2001).

[101] Bertrams, T., Brodde, A. and Neddermeyer, H., *J. Vac. Sci. Technol. B*, **12**, 2122 (1994).

[102] Rosenhahn, A., Schneider, J., Kandler, J., Becker, C. and Wandelt, K., *Surf. Sci.*, **433-435**, 705 (1999).

[103] Siegbahn, K., Nording, C. N., Fahlman, A., Nordberg, R., Hamrin, K., Hedman, J., Johansson, G., Bermark, T., Karlsson, S. E., Lindgren, I. and Linberg, B., ESCA: Atomic, Molecular and Solid State Structure Studied by Means of Electron Spectroscopy, Almqvist and Wilksells, Uppsala, 1967.

CHAPTER 2

OXIDE FILM GROWTH ON Fe(111) AND STM INDUCED HIGH ELECTRIC FIELD STRESS IN Fe_2O_3/Fe(111) [*]

2.1. Introduction

The oxygen/iron system is involved in a wide variety of technologically important areas such as catalytic oxidation [1, 2], corrosion process [3], and metallurgy [4]. Furthermore, the magnetic properties of iron oxides are utilized for the development of high-density magnetic recording media and sensors [5-7]. Previous studies have examined oxidation at the surfaces of thin films [6], electrolytic rod [8], and polycrystalline substrates [9, 10]. Single crystal substrates [11-13] have been employed in the kinetic and structural studies of oxygen/iron interaction to get a better understanding of the elementary mechanisms of oxidation process. LEED [11, 12, 14, 15], AES [8, 11, 13, 16], XPS [10, 17, 18], electron energy-loss spectroscopy (EELS) [19, 20], and ultraviolet photoelectron spectroscopy (UPS) [21], are the most common surface science techniques that have been employed in these studies.

The basic surface science underlying the formation and reactivity of iron oxides, however, is not well understood, despite their technological importance and numerous

[*] This chapter is reproduced with permission from Elsevier (Thin Solid Films). Reference: Qin, F., Magtoto, N.P., Garza, M. and Kelber, J.A., *Thin Solid Films*, **444**, 179 (2003).

efforts by different research groups. Reasons for this include the unavalibititity of large iron oxide single crystals and the difficulty associated with preparing clean stoichiometric surfaces in UHV [22]. In addition, some iron oxides (FeO and Fe_2O_3) are electrical insulators in bulk form, which gives rise to charging problems when using electron spectroscopy techniques [5]. A related problem is the imaging of the iron oxide surfaces with STM since this requires the flow of current between the tip and the sample. One way to overcome these experimental problems is to prepare ultrathin oxide films on a metal substrate [23, 24]. Such films are sufficiently thin as to not charge under electron bombardment, allowing the application of surface spectroscopic probes [25]. Furthermore, by preparing ultrathin iron oxide on metal substrate, STM and STS can be used to investigate both geometric and electronic properties of iron oxide surfaces. Recently, a number of surface science studies have attempted to explore the surface structures of various single crystal iron oxide phases using STM [7, 22, 26-30]. These studies have provided information on the formation and transformation of iron oxides [27, 29], surface crystal structure [28], and surface termination, composition and reconstruction of iron oxides [7, 22, 26, 30]. Schedel-Niedrig et al. have, using core and valence level photoemission [5], shown that the electronic structure of an iron oxide film is equivalent to that of the corresponding bulk material. STM and STS measurements, therefore, can add considerable insight into the growth process of iron oxides by providing spatially resolved data on surface topography and electronic structure during various growth stages.

STM has been recently utilized to study the dielectric breakdown of oxide films as well [31-35]. The application of even a modest bias voltage (1 –3 V) across ultrathin films of dielectric materials can generate an extremely high electric field (in excess of 10^7 V/cm), because the STM tip/sample distance is exceptionally small. In addition, due to its high spatial resolution, STM allows for systematic study of the effects of high electric field on the morphology and composition of a surface, which directly leads to the understanding of the intrinsic dielectric characteristics of the film at nanometer-scale resolution. Dielectric breakdown of thin SiO_2 films [36-38] and Al_2O_3 films [34, 39, 40] has been previously studied. In general, the breakdown of SiO_2 films is connected with the formation of traps or defects inside the oxides and at the interface. Abrupt ("hard") breakdown is observed on well ordered, ultrathin Al_2O_3 films grown on a $Ni_3Al(111)$ substrate at field strengths of 11 ± 1 MV/cm [35].

The behavior of ultrathin iron oxide films under high electric field is of critical importance to the development of magnetroresistance memories [5, 6]. Furthermore, thin iron oxide films serve as corrosion barriers for iron and iron alloys. It has been demonstrated that the current induced by the mobile ions in these barriers increases exponentially under high electric field [41, 42]. Localized corrosion and dielectric breakdown of the passive films, also referred to as "pitting", are often observed under electrochemical conditions (applied potential or anion absorption). These electrochemical conditions are typically associated with the generation of electric fields greater than 1MV/cm [43, 44]. High field stress study of such films, therefore, is directly relevant to understanding corrosion of iron.

In this chapter we report the oxide growth on Fe(111) at different temperatures and the dielectric breakdown behavior of iron oxides formed at different temperatures. STM/STS data indicate fundamentally different oxide growth processes occurred at 300 K and 500 K. Oxidation at 300 K results in the formation of relatively small oxide islands that uniformly cover the Fe(111) substrate. The oxide film grown at 500 K is less uniform with islands that range from 100 – 300 nm in width. The height variation of the oxide islands ranges from 7-15 nm. Dielectric breakdown of iron oxide formed at 300 K occurs at a critical tip/sample bias voltage of 3.8 ± 0.5 V at estimated electric field strengths between 12 and 17 MV/cm. No reproducible result is obtained from the high field stress studies of the iron oxide formed at 500 K. AES results indicate that oxidation of the Fe(111) at room temperature results in the formation of both Fe_2O_3 and Fe_3O_4, and that Fe_3O_4 is the predominant oxide phase observed while oxidizing the sample at 500 K.

2.2. Experimental Methods

Experiments were carried out in an Omicron UHV-STM system as shown schematically in Fig. 2.1. The UHV system was composed of two parts: the sample analysis chamber and the STM chamber. The sample analysis chamber was equipped with an Auger spectrometer from Physical Electronics (CMA 10-155), and a four-grid LEED optics (Omicron). The STM chamber was equipped with an ambient temperature STM system (Omicron). Additional facilities in the sample analysis chamber included an ion gun for sputter-cleaning the sample, manual leak valves for introducing small amounts of gases (O_2, H_2O) into the chamber. The STM chamber was attached to the

sample analysis chamber (Fig. 2.1). A 12-inch travel high precision *x*-*y*-*z* manipulator allowed translation of the sample along the three directions within the sample analysis chamber, as well as rotation about the manipulator axis. Sample transfer to the STM stage was accomplished with the use of a wobble-stick. STM tips were made by electrochemically etching a polycrystalline tungsten wire (diameter 0.01 in.). While mounted on the manipulator, the sample could be heated from the rear by indirect resistive heating of the sample holder. A type K thermocouple was attached to a sample clip approximately 5 mm away from the sample. The difference between the actual temperature and the thermocouple reading was not calibrated.

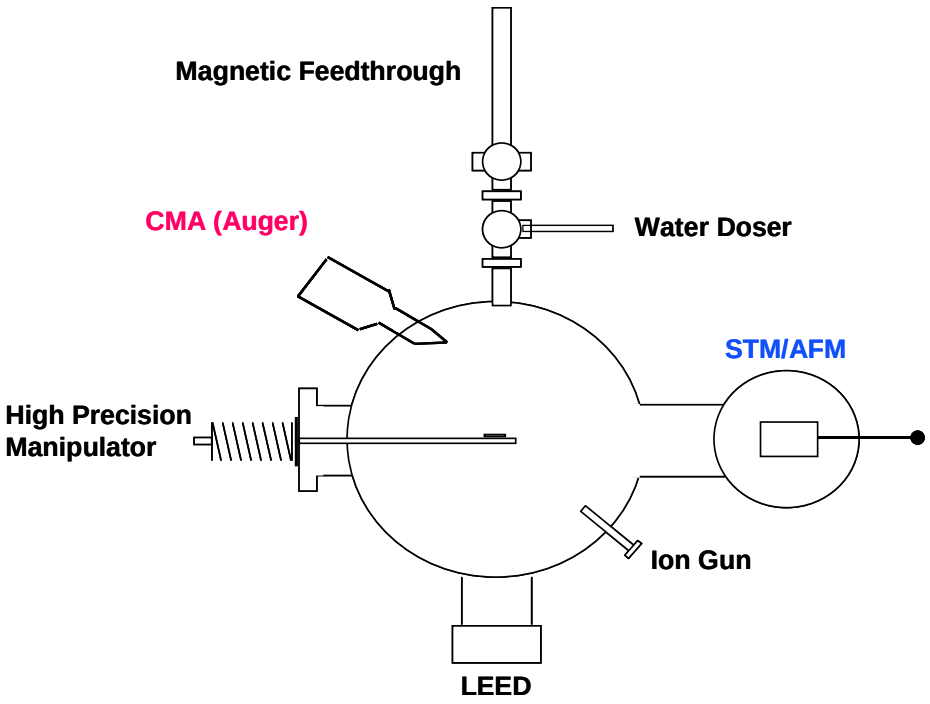

Fig. 2.1. Schematic illustration of the UHV-AES/LEED/STM system (top view).

The base pressure of the experimental ion/Ti sublimation-pumped chamber was 5 $\times 10^{-11}$ Torr after bake-out. A turbomolecularly pumped sample introduction chamber (base pressure, 5×10^{-10} Torr) was attached to the experimental chamber and separated from it by a gate valve. Sample transport between the two chambers occurred under controlled UHV conditions by means of a magnetic linear feedthrough. Dual filters mounted between the turbomolecular pump and the rotary backing pump were used to prevent back-migration of rotary pump oil vapor into the UHV system.

Auger spectra were acquired using a cylindrical mirror analyzer (CMA) with a coaxial electron gun. The electron gun was operated with excitation energy of 3 keV with an estimated spot diameter of 0.2 cm^2. In order to assure consistent peak energies, the sample-to-analyzer distance was always adjusted by measuring the energy of the 3 KeV elastic peak [45]. Auger spectra were acquired in the integral mode [N(E)] mode under computer control, and then differentiated [dN(E)/dE] and smoothed using a Savitzky-Golay program.

The Fe(111) crystal (99.94% pure, obtained from ESPI) had a diameter of 9.6 mm and a thickness of 1mm, and was aligned to within ±1° of the (111) plane. The sample was spot-welded onto a tantalum plate that could be transferred between the manipulator and STM stage by a wobble-stick. The impurities on the Fe(111) sample most notably were sulfur, oxygen, and carbon. The Fe(111) was cleaned by repeated cycles of Ar^+ sputtering followed by annealing to 700 K, until the surface was judged clean by AES LEED, and STM. The cleanliness of the sample was verified by the absence of observable carbon and sulfur impurities, and the lowest achievable concentration of

oxygen (~ 0.1 monolayer of oxygen). The 0.1 ML coverage of the oxygen impurity on the Fe(111) surface was calculated using equation :

$$\frac{\theta_A\left(1-e^{-\frac{a_A}{\lambda_A}}\right)}{1-\theta_A\left(1-e^{-\frac{a_A}{\lambda_B}}\right)}=\frac{I_A/I_A^{\infty}}{I_B/I_B^{\infty}} \qquad (2\text{-}1)$$

Here, θ_A is the fractional monolayer coverage of oxygen, λ_A is the inelastic mean free path of $O_{(510)}$ peak in oxygen, α_A is the diameter of oxygen molecule, I_A and I_B are the intensity of O (KVV) transition at 510 eV and Fe (LMM) transition at 703 eV, I_A^{∞} and I_B^{∞} are the atomic sensitivity factor of $O_{(510)}$ and $Fe_{(703)}$ transition [46]. The Fe(111) surface with 0.1 ML of oxygen yielded a sharp $2\sqrt{3} \times 2\sqrt{3}$ LEED pattern, in agreement with previous work [47]. STM imaging of the clean iron surface showed terraces typically 150 - 300 nm in width. The step heights were as high as ~50 Å. I/V spectroscopy (not shown) of the clean surface demonstrated ohmic behavior.

Oxidation experiments were carried out at different temperatures by backfilling the chamber with oxygen gas at partial pressures in the range 1×10^{-7} to 5×10^{-7} Torr. O_2 gas (99.998% pure, purchased from Matheson and used without further purification) was introduced into the chamber through a manual leak valve. Pressures were measured with a nude ion gauge previously calibrated for N_2. Exposures are reported in Langmuir (1 L = 10^{-6} Torr-sec), and have not been corrected for ion gauge sensitivity or flux to the sample. The Auger electron gun filament and the ion pump were shut off during oxidation.

STM measurements and dielectric breakdown studies were carried out in constant current mode at room temperature with the sample typically biased positive. Iron oxides were subjected to high electric fields by applying bias voltage between the sample and the STM tip while maintaining an active feedback loop to inhibit tip/sample physical contact. The experimental details have been described elsewhere [34]. After imaging a large area of the oxide surface, scanning was stopped and the tip was directed to a specific point above the surface within this area. With the feedback loop set at 1 nA, the tunneling voltage was increased to a desired value in 200 steps. Each step required about 200 μs. The magnitude of the electric field (E) at a certain bias voltage (V) was estimated according to:

$$E = V/(t_{ox} + d), \qquad (2\text{-}2)$$

Here t_{ox} is the oxide thickness and d is the tip-sample distance. The tip-sample distance d is the sum of the initial tip-sample separation d_0 (i.e., the tip-sample distance at 0.1 V bias and 0.1 nA feedback current) and the recorded displacement d_1 of tip from d_0 upon increasing the bias voltage to a specific value. The value of d_0 was estimated using the plots of gap voltage versus tip-sample separation (not shown). The value of d_0 (at 0.1 V bias and 0.1 nA feedback current) was estimated to be 14 Å from the fact that the tip approached the sample by about 14 Å when the bias was reduced from initial tunneling bias voltage of 0.1 V to 0 V, where minimum tip-sample separation is expected [34]. Eqn. (2-2) neglects the influence of the dielectric constant of iron oxide for the reason that the dielectric constant of the ultrathin oxide film (< 10 Å) undoubtedly differs from that of the bulk oxide due to the overlap of the wave function of the oxide with the metal

substrate [48]. The use of Eqn. (2-2) to estimate tip sample separation, and therefore field strengths, is obviously an approximation. Critical breakdown values for ultrathin Al_2O_3 films, derived from Eqn. (2-2), are, however, in good agreement with extrapolated results from capacitance measurements on thicker films [34, 35]. After each high field stressing, the image was acquired under normal tunneling conditions, i.e., 0.1 V bias voltage and 0.1 nA constant feedback current.

2.3. Results

2.3.1. Oxidation of Fe(111) at 300 K

Oxidation at 300 K was performed on the clean iron surface at oxygen pressures in the range of 1.0×10^{-7} to 5.0×10^{-7} Torr. Since no oxygen and iron lineshape changes occur in the regions near 510 eV and 703 eV, the O(510 eV)/Fe(703 eV) Auger ratios may be used to accurately calculate the surface coverage of oxygen [13]. Variation in the O(510 eV)/Fe(703 eV) intensity ratio with oxygen exposure at 300 K is shown in Fig. 2.2a (300 K) compared to results obtained at 500 K (Fig. 2.2b). Exposing Fe(111) to O_2 at 300 K (Fig. 2.2a) results in a rapid initial increase in oxygen coverage, approaching saturation at ~ 200 L exposure. Spectrum A of Fig. 2.3 represents a Fe(111) sample with low oxygen coverage (0.1 monolayer of oxygen) due to reaction with background gas in vacuum chamber. This spectrum exhibits a single Fe (MVV) transition with a negative-going peak in the derivate spectrum at 47 eV [8]. Unlike the higher energy Fe Auger peaks, the low energy 47 eV transition exhibits several changes with increasing oxygen exposure at 300 K, as shown in Fig. 2.3. It has been recognized that these lineshape

changes in the Fe (MVV) Auger transition following oxygen exposure are associated with the development of different oxide phases [8, 10, 11, 13]. After oxygen exposure of 10 L at 300 K (spectrum B of Fig. 2.3), there is a large reduction in negative-going intensity of the 47 eV peak and the appearance of a negative-going shoulder at 52 eV. In addition, the positive-going peak at 36 eV of pure iron shifts to 34 eV. The intensity of the 52 eV negative-going peak became greater as the oxygen exposure was increased.

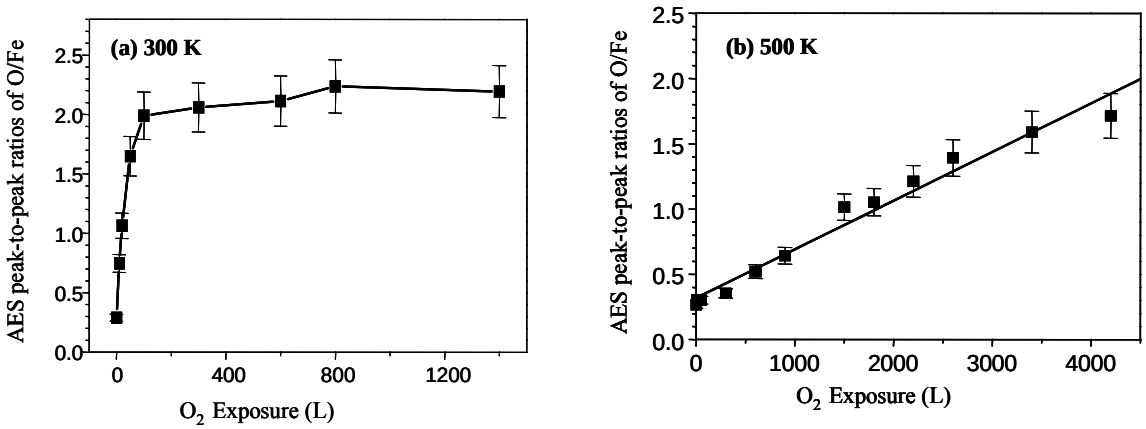

Fig. 2.2. Evolution of oxygen peak-to-peak heights with O_2 exposure for Fe(111) during oxidation at (a) 300 K; (b) 500 K.

Upon comparison of Auger spectra with reference iron oxide spectra in the literature [8, 13], the negative-going peak at 52 eV can be assigned to Fe_3O_4. The shift of the positive-going peak might be an indication that there is some Fe_2O_3 present in the oxide layer at this stage. It is notable that the Fe_3O_4 -containing overlayer (spectrum B of Fig. 2.3) exhibits the Fe (MVV) transition of metallic iron at 47 eV, possibly due to the contribution of the underlying metallic iron [8, 13]. After a cumulative oxygen exposure

of 20 L at 300 K, a negative-going peak is observed to develop at 44 eV and increases in intensity. The 47 eV Auger transition due to metallic iron was not detected for oxygen exposure greater than 20 L (spectrum C of Fig. 2.3), demonstrating that most of the

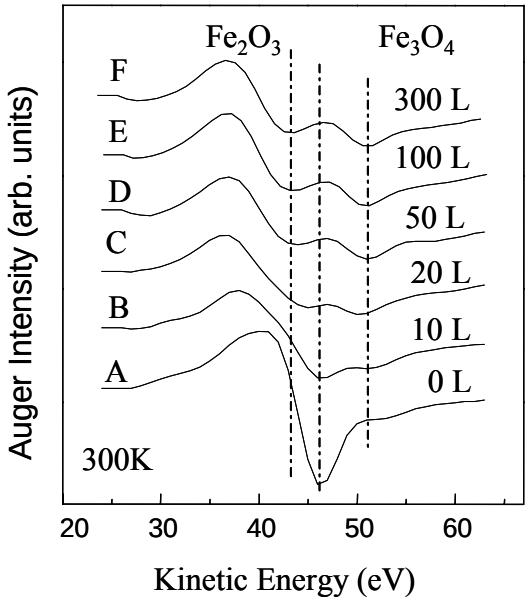

Fig. 2.3. Changes in the Auger lineshape with increasing O_2 exposure at 300 K.

surface region of the Fe(111) sample had been converted to an oxidized electronic state. The presence of the two peaks at 44 eV and 52 eV resembles the lineshape associated with Fe_2O_3 [8, 13]. Auger spectra at the saturation exposure indicate that an Fe_2O_3 overlayer has developed on top of the Fe_3O_4 layer [8, 11, 13, 16]. Several other groups have reported similar results on oxidation studies of Fe(110), Fe(100), and polycrystalline Fe at 300 K [11-13].

STM measurements were carried out after exposing the clean Fe(111) surface to 400 L of oxygen at 300 K. STM images (Fig. 2.4a) revealed that an oxide film with numerous small islands was formed. The size of the islands ranged from 5 to 15 nm, and the height variations were several angstroms (5 Å to 8 Å) (Fig. 2.4b). As shown in Fig. 2.4c and Fig. 2.4d, tunneling current versus gap voltage (I-V) measurements showed that both the oxide islands and the areas between the islands displayed insulating behavior, indicating that the Fe(111) substrate was uniformly covered by iron oxide. No LEED pattern was observed after oxidation, indicating the absence of a long-range order in the oxide film.

2.3.2. Oxidation of Fe(111) at 500 K

Oxidation at 500 K was performed on the clean iron surface at oxygen pressures in the range of 1.0×10^{-7} to 5.0×10^{-7} Torr. In contrast to the oxidation at 300 K, the AES $O_{(510)}/Fe_{(703)}$ peak-to-peak height ratio (Fig. 2.2b) did not exhibit saturation for O_2 exposures up to 4200 L. Changes in the low energy Fe (MVV) Auger lineshape with increasing oxygen exposure at 500 K are displayed in Fig. 2.5. It is notable that the metallic Auger transition at 47 eV is still detectable even at an O_2 exposure of 4200 L. In contrast, this peak is no longer detectable after 20 L O_2 exposure at 300 K. The low energy Auger spectrum of Fe(111) with O_2 exposure of 4200 L at 500 K (Fig. 2.5) displays only the 52 eV peak and the 47 eV metallic iron peak which are characteristic of Fe_3O_4, indicating the predominant formation of Fe_3O_4 under such conditions. Oxidation studies of Fe(110) at higher temperature exhibit similar behavior [11, 13]. The shift of the

positive-going peak at 36 eV might be an indication that there is some Fe_2O_3 present in the oxide. These results suggest that Fe_3O_4 is the more stable oxide phase at 500 K, and that Fe_2O_3, which formed at 300 K, is not stable and hence exists only in small amount at

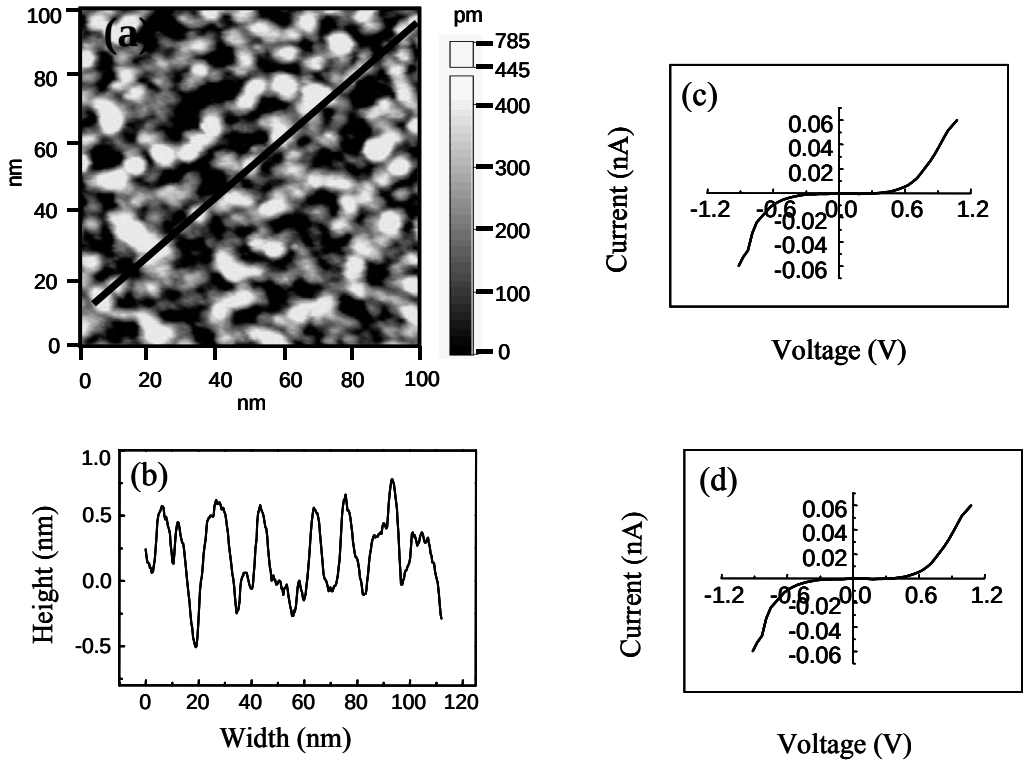

Fig. 2.4. Fe (111) surface after exposure to O_2 at 300 K: (a) A 100 nm × 100 nm STM image after 400 L O_2 exposure (Vgap = 0.1 V, I = 0.1 nA); (b) Line profile of the surface; (c) I/V spectra for the islands; (d) I/V spectra for areas between islands.

500 K under UHV conditions. This may be due to the migration of Fe from the substrate through the growing oxide at 500 K, resulting in the reduction of Fe_2O_3 to Fe_3O_4, which produces predominantly Fe_3O_4 on the Fe(111) surface at 500 K [13].

An STM image (Fig. 2.6a) taken after exposure to 1500 L O_2 revealed that oxidation of the Fe(111) surface at 500 K results in the formation of larger and more scattered oxide islands compared with oxidation at 300 K. The height variation of the islands ranges from 70 Å to150 Å. Fig. 2.6b displays an island with a height of 90 Å and

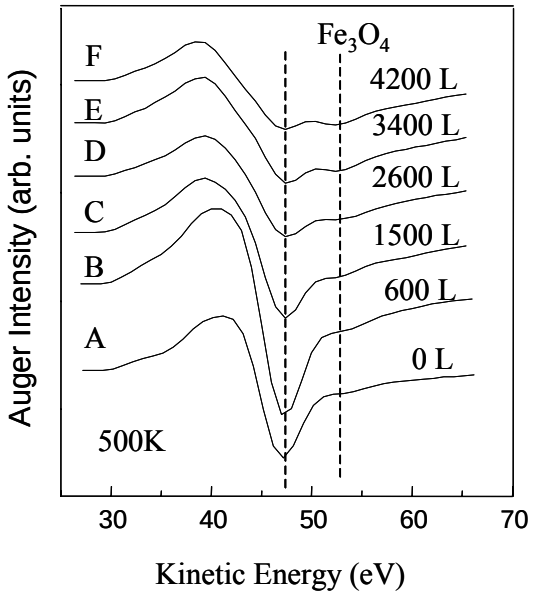

Fig. 2.5. Changes in the Auger lineshape with increasing O_2 exposure at 500 K.

width of 120 nm. I/V measurements (Fig. 2.6c) indicate insulating behavior in areas covered by oxide islands and ohmic behavior in the area between the islands, demonstrating that oxidation of Fe(111) at 500 K resulted in the formation of oxide islands interspersed with patches of a metallic substrate, which is consistent with the persistence of the Fe^0 MVV transition at 47 eV (Fig. 2.5), and the absence of saturation in oxide formation at 4200 L.

2.3.3. High Electric Field Stressing of Iron Oxides Formed at 300 K and 500 K

Fe oxide films formed at 300 K were exposed to high electric fields by systematically increasing the bias voltage between the STM tip and the sample while in constant current feedback. Under constant current feedback conditions, the onset of

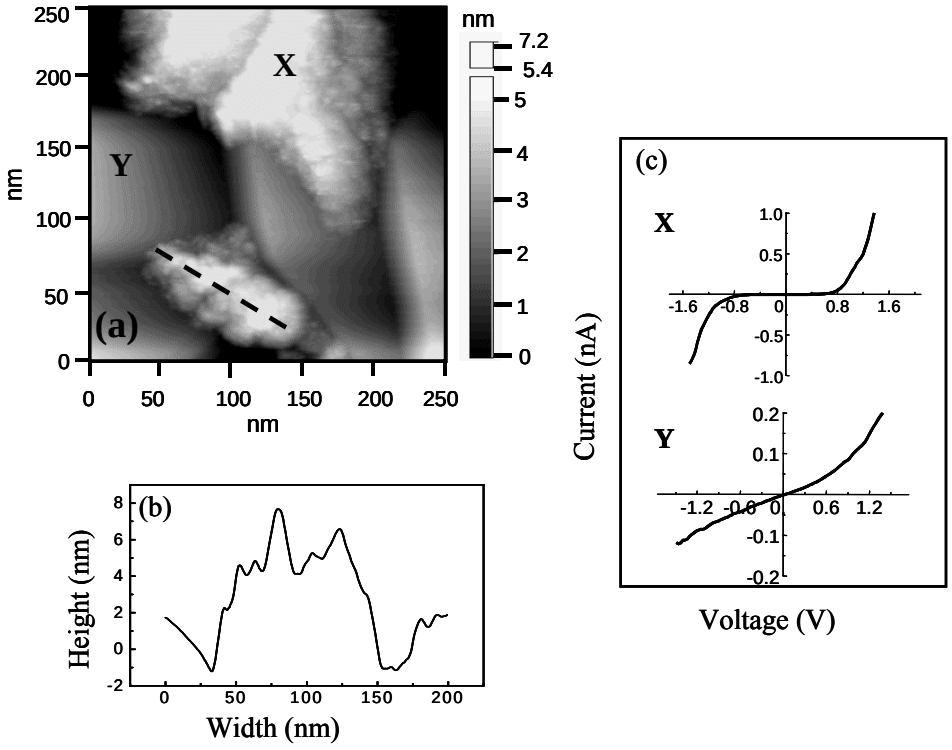

Fig. 2.6. Fe (111) surface after exposure to O_2 at 500 K: (a) A 250 nm × 250 nm STM image after 1500 L O_2 exposure (Vgap = 0.1 V, I = 0. 1 nA); (b) Line profile of the surface; (c) I/V spectra for X and Y region.

breakdown was marked by a precipitous retreat of the tip from the sample surface (Fig. 2.7). The occurrence of dielectric breakdown was also marked by the appearance of a feature that appeared as an elevation under constant current imaging (Fig. 2.8). As shown

by line profiles (Fig. 2.8d), the apparent size of such features was normally 6 to 20 nm in height with diameters ranging from 50-200 nm.

In order to probe the nature of the elevated feature observed under constant current imaging, constant height imaging was performed over the feature displayed in Fig. 2.8c. Prior to imaging at constant height mode, the tip-sample separation was set at 14 Å by adjusting the feedback current at 0.1 nA and bias voltage at 0.1 V. High scanning speed (up to 5000 nm/s) and significantly reduced feedback were used during constant height scanning, so that the controller could not respond to the current changes induced

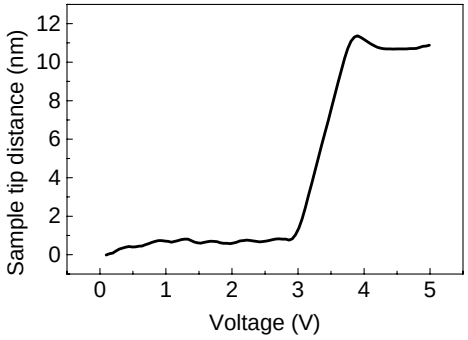

Fig. 2.7. A Z/V spectrum for the dielectric breakdown of the iron oxide formed at 300 K.

by individual features on the surface. The dashed line in Fig. 2.8d represents the movement of the tip over the sample surface under constant height scanning mode. This procedure did not result in physical interaction (tip crash) between the tip and the apparent feature at the breakdown site. In contrast, performing such an action with a "real" topographical surface feature (e.g., an oxide island) would immediately result in tip/sample collision and in the loss or at least severe distortion of the subsequent image

and immediate disruption of the tunneling current. The absence of tip-surface physical interaction during constant height imaging under these conditions indicates that the elevated feature displayed in constant current images (Fig. 2.8c) is not primarily due to mass transport, but due to electronic changes in the surface. This response is similar to that observed for high field studies of $Al_2O_3/Ni_3Al(111)$ [35]. This conclusion is further corroborated by current/voltage (I/V) spectroscopy of the affected region before and after high field exposure (Fig. 2.9). As shown in Fig. 2.9, I/V behavior of the affected region

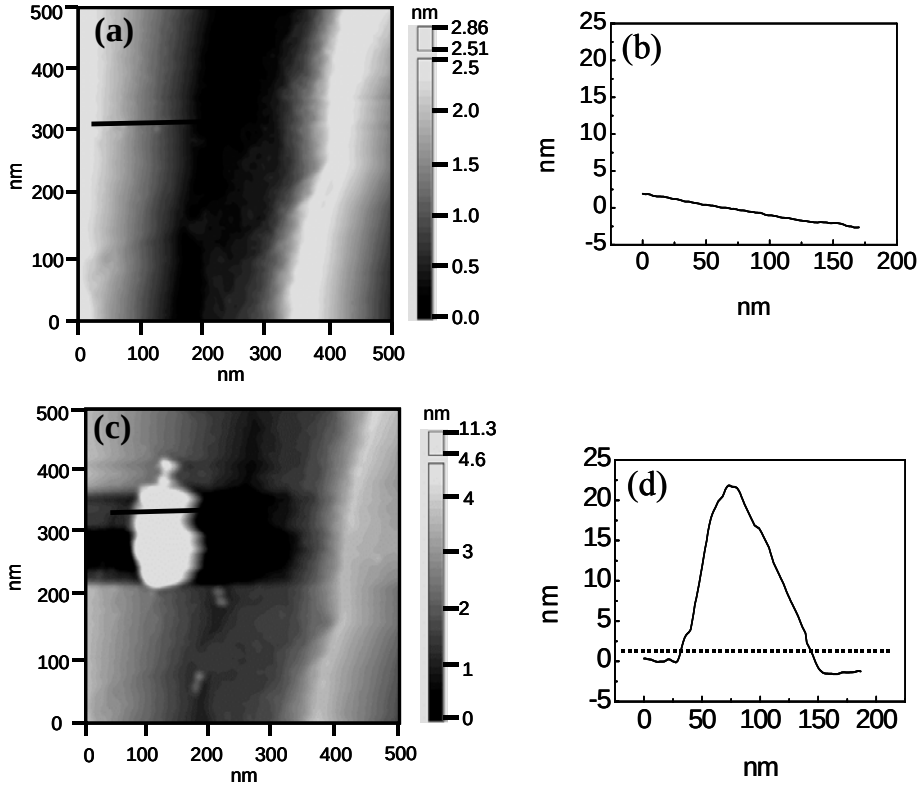

Fig. 2.8. 500nm × 500 nm STM images of iron oxide formed at 300 K: (a) before high field stressing; (c) after high field stressing (Vgap = 0.1 V, I = 0.1 nA); (b) and (d)– corresponding line profiles of (a) and (c). The dashed line in (d) represents the movement of the tip over the sample surface under constant height scanning mode.

(Fig. 2.8) before and after breakdown indicates that the breakdown has changed the local electronic properties of the oxide from insulating to ohmic in nature.

High electric field stress was applied to different areas of the iron oxide formed at 300 K for certain feedback current, hence a set of breakdown Z/V curves was obtained for each feedback current. By varying the feedback current, i.e. the tip/sample distance, the induced electric field could be systematically varied. The data in Fig. 2.10 indicate that for the iron oxide grown at 300 K, a critical breakdown voltage of 3.8 ± 0.5 V is observed, but that the corresponding applied field associated with breakdown varies from ~ 12 MV/cm to 17 MV/cm. The data in Fig. 2.10 were acquired with the sample

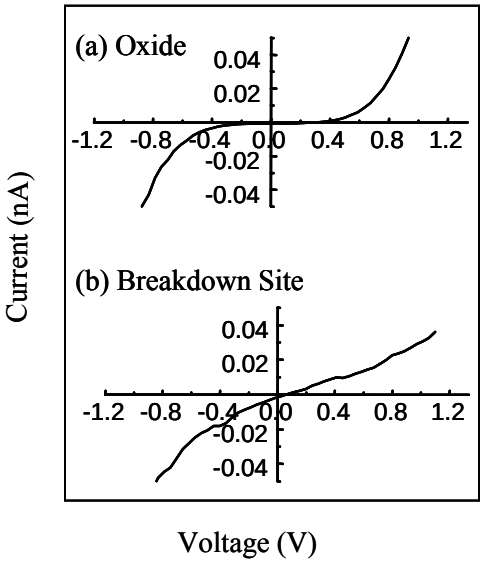

Fig. 2.9. I/V spectra of iron oxide formed at 300 K of (a) oxide; (b) breakdown site.

biased positive with respect to the tip. Systematic study on the effect of electric field stressing in the opposite direction was also carried out on the iron oxide formed at 300 K. The result showed that the breakdown threshold voltage at negative bias (sample biased

negative with respect to the tip) for different feedback current is 0.3 V higher than at positive bias (4.1 vs 3.8 V). A higher breakdown threshold voltage with the sample biased negative was also observed on SiO_2 films [32] and thin Al_2O_3 films [35]. Such polarity-induced differences in breakdown voltages have been associated with electron injection into the oxide [32]. In this case, however, the voltage difference (0.3 V) is smaller than the uncertainty in the measured threshold (0.5 V), so nothing definitive can be said on this point from the existing data.

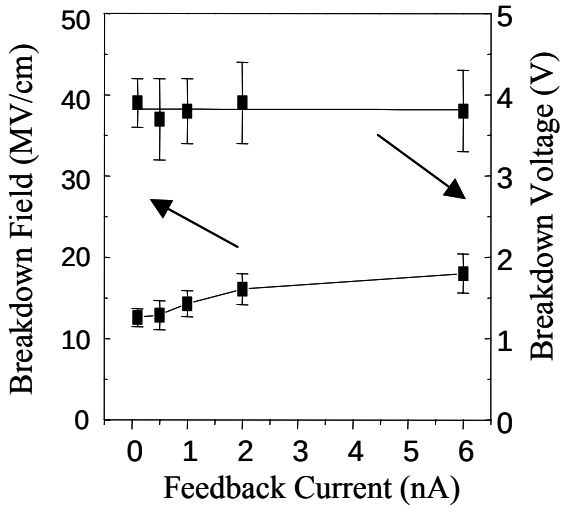

Fig. 2.10. Dielectric breakdown voltages and fields of iron oxide formed at 300 K using different feedback current (sample biased positive).

High electric field stress was also applied on the iron oxide formed at 500 K. However, no reproducible result was obtained from this study, so not much can be said on this point from the existing data.

2.4. Discussion

The results shown here indicate that oxidation of Fe(111) at 300 K proceeds in a qualitatively different manner than at 500 K. Oxidation of Fe(111) at 300 K results in the roughening of the surface as evidenced by the appearance of the smaller oxide islands. However, the substrate steps remain visible (Fig. 2.8a), which is a clear indication that the oxide growth at 300 K is governed by the limited mobility of the oxygen atom rather than transport of the metal atom, as observed previously for the study of the oxide formation on $Ni_3Al(111)$ [49]. The decrease of oxygen sticking coefficient with O_2 exposure (Fig. 2.2a) indicates limited oxide or Fe metal surface mobility. The STM results (Fig. 2.4) in conjunction with the AES data (Fig. 2.3) indicate the growth of thin Fe_3O_4 islands on a continuous insulating layer (perhaps FeO). At higher exposures, Fe_2O_3 forms on the Fe_3O_4 islands. A typical island height of 5 Å to 8 Å is consistent with negligible O and Fe transport during oxide formation. This mechanism of Fe oxide formation at 300 K is in close agreement with that proposed previously in the absence of STM data [50]. This model also suggests that the presence of impurities (such as sulfur) at the oxide/metal interface substantially limit the area of interfacial metal/oxide bond formation, thus contributing to the thermal instability of the oxide layer [51].

At 500 K, STM (Fig. 2.6) indicates the formation of thicker (~ 50 Å or higher) islands on the metallic substrate. This is consistent with a constant sticking coefficient for O_2 (Fig. 2.2b) and the persistence of a metallic Fe signal in the Auger spectrum (Fig. 2.5), and indicates that O_2 molecules react with the Fe surface, followed by oxygen (or oxide) migration to form oxide islands. The predominance of Fe_3O_4 rather than Fe_2O_3 at 500 K

has been ascribed to Fe transport to the surface of the growing oxide resulting in continual partial reduction of the Fe_2O_3 film [13]. The persistence of a metallic substrate combined with a constant O_2 sticking coefficient and the predominance of Fe_3O_4 formation at 500 K indicate a process in which enhanced Fe mobility inhibits the formation of a continuous oxide layer, and that field-enhanced Fe diffusion within oxide islands results in thicker islands but with the ongoing partial reduction of the oxide from Fe_2O_3 to Fe_3O_4.

A band gap value of 2.1 eV has been reported for a thermally grown iron oxide film that consisted of an inner Fe_3O_4 layer and an outer Fe_2O_3 layer [52]. The band gap in bulk Fe_2O_3 has been reported as 2.34 eV [53]. Fe_3O_4 (magnetite) being half metallic displays a co-existence of metallic character for one electron population and insulating character for the other, which leads to 100% spin polarization at the Fermi level [54]. Magnetite has good room temperature conductivity, which arises because of electron hopping between Fe^{+2} ion and Fe^{+3} ion sites. For this reason, a band gap is not expected to show up in the I/V spectra of Fe_3O_4. The band gap of 2.1 eV observed in the previous study [52] was attributed to Fe_2O_3. In our study, the iron oxide film formed at 300 K comprised of Fe_2O_3 and Fe_3O_4. An apparent band gap of 0.8 eV was obtained for this film (Fig. 2.9). In view of the fact that the thickness of the iron oxide film used in the previous study [52] was 3μ, and that the thickness of the oxide film in our study is only several angstroms, it is easy to understand the discrepancy. The narrowing of the band gap has also been reported for ultrathin Al_2O_3 film [35, 55, 56]. According to density functional theory calculations [48], the narrowing of the band gap in ultra-thin oxide

films is due to the overlap of wave functions of the oxide with the metal substrate, resulting in a broadening of the densities of the states near the oxide band edge.

A band gap value of 2.0 eV for single crystal magnetite $Fe_3O_4(110)$ at feedback current of 0.2 nA and scanning voltage of 2 V has been obtained by STS [7]. This apparent anomaly in the behavior of the conductive magnetite was accounted for by the presence an "α-Fe_2O_3-like" on the Fe_3O_4 surface. Detailed analysis of LEED patterns and STM data demonstrated that the magnetite surface formed an "α-Fe_2O_3-like" termination, which had the hcp structure, with an ABAB… stacking of the hexagonal oxygen layers along (111), while Fe_3O_4 has an ABCABC… stacking. Although an α-Fe_2O_3 surface layer cannot be matched smoothly to the (110) surface of the Fe_3O_4 bulk because of the different stacking of the oxygen layers, a structure ("α-Fe_2O_3-like") that preserves the tripled periodicity and the higher oxygen content can be formed [7]. The presence of an insulating layer of "α-Fe_2O_3-like" at the magnetite surface can explain the reported band gap [7]. In this study, a band gap value of 1.6 eV for the iron oxide (primarily Fe_3O_4) formed at 500 K was obtained (Fig. 2.6). The Fe_3O_4 formed in this study at 500 K contains isolated oxide islands with thickness in excess of 70 Å, and no observed long-range order. The observed band gap of 1.6 eV may, therefore, reflect an "α-Fe_2O_3-like" termination of the surface similar to the data reported earlier [7], together with a significant number of defect states in the band gap.

The fact that magnetite is conductive can explain the response of iron oxide (predominantly Fe_3O_4) formed at 500 K to high electric field stressing. The band gap we observed is not due to the presence of an insulator, but is probably because of the

presence of a "α-Fe_2O_3-like" termination layer. In addition, the oxide islands formed at 500 K is considerably larger with a broader distribution of island dimensions. Hence, it is not surprising that we cannot get reproducible results on the high field study iron oxide formed at 500 K.

Oxide dielectric breakdown under electric field stress is an important issue for the use of ultrathin oxide films in gate oxides and capacitors, as well as in GMR and other nanoelectronic applications. The ability to consistently induce breakdown of oxide films grown at 300 K, regardless of tip/sample polarity, indicates that the observed effects are not due simply to electron field emission from the tip resulting in electron stimulated desorption or other damage to the oxide. STM-induced breakdown measurements carried out on 7 Å thick, highly ordered Al_2O_3 films on $Ni_3Al(111)$ [34] indicated that the breakdown was a function of the applied field, rather than the applied voltage. In contrast, voltage-dependent dielectric breakdown in Al-Al_2O_3-Au diodes has been reported by Hickmott [39], where the breakdown voltage is ~ 4.5 V independent of Al_2O_3 thickness. The breakdown of iron oxide thin film formed at 300 K in our study occurs at a constant voltage independent of the tip-sample distance. At present, we cannot explain the difference, but a possible factor may be that our simple estimates of field strength (Eqn. 2-2) do not permit a sufficiently accurate determination of field strength for a film of highly irregular topography. Another possibility is that there are two types of mechanisms which produce defects and/or bond scission under electric field stress. One type is influenced primarily by applied voltage, the other by applied field. One such mechanism would involve an electron transition from a valence ("bonding") to a

conduction ("antibonding") band. Such a transition would be expected to occur at a critical voltage (V_{crit}), concurrent with dielectric breakdown. Just such a $\sigma \rightarrow \sigma^*$ mechanism has been proposed for field-induced Si-H bond scission [57]. Such a V_{crit}-dependent mechanism might also be indicative of a process dominated by electron injection across the metal oxide interface into empty oxide states, and this would explain the results observed [39] for conventional capacitance measurements carried out on thicker films. For the ultrathin Fe oxide discussed here, a V_{crit} of ~ 3.8 V is hard to reconcile with an observed band gap of ~ 2 eV for a thermally grown Fe_3O_4 film which is Fe_2O_3 terminated [52]. The breakdown results reported here therefore suggest an electron injection mechanism.

In contrast, the critical field (E_{crit}) results obtained for STM-induced breakdown studies of ultrathin Al_2O_3 films [34] on $Ni_3Al(111)$ suggest a process dominated by the Stark effect due to the coupling of the electric field with an ionic bond [58]. Bond scission would occur at field strengths which inhibit phonon transfer between ionic (presumably metal-oxygen) bonds and more covalent neighboring bonds. In fact, such a field-induced threshold has also been observed for Si-H bond scission [59].

All the above, of course, is highly speculative. More detailed measurements on single-phase oxides on well-defined substrates, with accurate measurements of tip-sample distance and calculations of electric field strength, are obviously required. The different results for different oxides, or even for nominally similar oxides with different oxide/metal interfaces, thicknesses, etc., may have important consequences in such applications as the fabrication of tunneling-based nanoelectronic devices.

2.5. Conclusions

AES, LEED and STM were used to study the oxidation of Fe(111) at 300 K and 500 K. In addition, STM and STS were employed to investigate the effect of high electric stress on iron oxide formed at both temperatures. The oxidation results indicate that at 300 K, Fe_2O_3 forms on top of Fe_3O_4, and that the Fe(111) substrate is uniformly covered with an oxide film with relatively small oxide islands. At 500 K, Fe_3O_4 is the predominant oxide phase formed, and the growth of oxide is not uniform, but occurred as large islands growing on a metallic substrate. Dielectric breakdown of iron oxide formed at 300 K occurred at a critical tip/sample bias voltage of 3.8 ± 0.5 V at estimated electric field strengths between 12 and 17 MV/cm. No reproducible result was obtained from the high field stress studies of the iron oxide formed at 500 K.

2.6. Chapter References

[1] Chinchen, G., Davis, P. and Sampson, R. J., in J. R. Anderson and M. Boudart (Eds.): Catalysis: Science and technology, Vol. 8, Springer, Berlin, 1987.

[2] Golodets, G. I., Heterogeneous Catalytic Reaction Involving Molecular Oxygen, Elsevier, Amsterdam, 1983.

[3] West, J. M., Basic Corrosion and Oxidation, 2nd ed., Ellis Horwood Limited, Chichester, 1986.

[4] Arabcysk, W. and Narkiewicz, U., *Appl. Surf. Sci.*, **108**, 379 (1997).

[5] Schedel-Niedrig, T., Weiss, W. and Schlogl, R., *Phys. Rev. B*, **52**, 17449 (1995).

[6] Kim, H.-J., Park, J.-H. and Vescovo, E., *Phys. Rev. B*, **61**, 15284 (2000).

[7] Jansen, R., Brabers, V. A. M. and Kempen, H. v., *Surf. Sci.*, **328**, 237 (1995).

[8] Seo, M., Lumsden, J. B. and Staehle, R. W., *Surf. Sci.*, **50**, 541 (1975).

[9] Sault, A. G., *Appl. Surf. Sci.*, **74**, 249 (1994).

[10] Ertl, G. and Wandelt, K., *Surf. Sci.*, **50**, 479 (1975).

[11] langell, M. and Somorjai, G. A., *J. Vac. Sci. Technol.*, **21**, 858 (1982).

[12] Simmons, G. W. and Dwyer, D. J., *Surf. Sci.*, **48**, 373 (1975).

[13] Smentkowski, V. S. and J. T. Yates, J., *Surf. Sci.*, **232**, 113 (1990).

[14] Gafner, G. and Feder, R., *Surf. Sci.*, **57**, (1976).

[15] Lu, J.-P., Albert, M. and Bernasek, S. L., *Surf. Sci.*, **215**, 348 (1989).

[16] Seo, M., Lumsden, J. B. and Staehle, R. W., *Surf. Sci.*, **42**, 337 (1974).

[17] Welsh, I. D. and Sherwood, P. M. A., *Phys. Rev. B*, **40**, 6386 (1989).

[18] Aronniemi, M., Sainio, J. and Lahtinen, J., *Surf. Sci.*, **578**, 108 (2005).

[19] Miyano, T., Sakisaka, Y., Komeda, T. and Onchi, M., *Surf. Sci.*, **169**, 197 (1986).

[20] Erley, W. and Ibach, H., *Solid State Commun.*, **37**, 937 (1981).

[21] Brundle, C. R., Chuang, T. J. and Wandelt, K., *Surf. Sci.*, **68**, 459 (1977).

[22] Chambers, S. A. and Joyce, S. A., *Surf. Sci.*, **420**, 111 (1999).

[23] Goodman, D. W., *J. Vac. Sci. Technol. A*, **14**, 1526 (1996).

[24] Street, S. C., Xu, C. and Goodman, D. W., *Annu. Rev. Phys. Chem.*, **48**, 43 (1997).

[25] Vurens, G. H., Salmeron, M. and Somorjai, G. A., *Prog. Surf. Sci.*, **33**, 333 (1990).

[26] Condon, N. G., Leibsle, F. M., Lennie, A. R., Murray, P. W., Vaughan, D. J. and Thornton, G., *Phys. Rev. Lett.*, **75**, 1961 (1995).

[27] Condon, N. G., Leibsle, F. M., Lennie, A. R., Murray, P. W., Parker, T. M., Vaughan, D. J. and Thornton, G., *Surf. Sci.*, **397**, 278 (1998).

[28] Wiesendanger, R., Shvets, I. V., Burgler, D., Tarrach, G., Guntherodt, H. J., Cory, J. M. D. and Graser, S., *Science*, **255**, 583 (1992).

[29] Fellows, R. A., Lenie, A. R., Raza, H., Pang, C. L., Thornton, G. and Vaughan, D. J., *Surf. Sci.*, **445**, 11 (2000).

[30] Stanka, B., Hebenstreit, W., Diebold, U. and Chambers, S. A., *Surf. Sci.*, **448**, 49 (2000).

[31] Watanabe, H., Baba, T. and Ichikawa, M., *J. Appl. Phys.*, **85**, 6704 (1999).

[32] Fukano, Y., Sugawara, Y., Yamanishi, Y., Oasa, T. and Morita, S., *Jpn. J. Appl. Phys.*, **32**, 290 (1993).

[33] Wallace, R. M., Chen, P. J., Archer, L. B. and Anthony, J. M., *J. Vac. Sci. Technol.* B, **17**, 2153 (1999).

[34] Niu, C., Magtoto, N. P. and Kelber, J. A., *J. Vac. Sci. Technol. A*, **19**, 1947 (2001).

[35] Magtoto, N., Niu, C., Ekstrom, B., Addepalli, S. and Kelber, J. A., *Appl. Phys. Lett.*, **77**, 2228 (2000).

[36] Chen, C.-C., Chang, C.-Y., chien, C.-H., Huang, T.-Y., Lin, H.-C. and Liang, M.-S., *Appl. Phys. Lett.*, **74**, 3708 (1999).

[37] Yamada, H. and Makino, T., *Appl. Phys. Lett.*, **59**, 2159 (1991).

[38] Yasue, T., Yoshida, Y., koyama, H., Kato, T. and Nishioka, T., *J. Vac. Sci. Technol.* B., **15**, 1884 (1997).

[39] Hickmott, T. W., *J. Appl. Phys.*, **88**, 2805 (2000).

[40] Kurnosikov, O., Nooij, F. C. d., LeClair, P., Kohlhepp, J. T., Koopmans, B., Swagten, H. J. M. and Jonge, W. J. M. D., *Phys. Rev. B*, **64**, 153407 (2001).

[41] Metikos-Hukovic, M. and Omanovic, S., *Mat. Chem. Phys.*, **38**, 55 (1994).

[42] Lohrengel, M. M., *Mater. Sci. and Eng. R.*, **11**, 243 (1993).

[43] Xu, Y., Wang, M. and Pickering, H. W., *J. Electrochem. Soc.*, **140**, 3448 (1993).

[44] Sullivan, J. P., Dunn, R. G., Barbour, J. C., Wall, F. D., Missert, N. and Buchheit, R. G., K. R. Hebert, R. S. Lillard and B. R. MacDougall, Oxide Films, Toronto, Canada, 2000, Electrochemical Society, Inc., 2000-4 (2000) 24.

[45] Riviere, J. C., in D. Briggs and M. P. Seah (Eds.): Practical surface analysis: Auger and X-ray photoelectron spectroscopy, Vol. 1, Wiley, New York 1979, p. 19.

[46] Seah, M. P., in D. Briggs and M. P. Seah (Eds.): Practical surface analysis: Auger and X-ray photoelectron spectroscopy, Vol. 1, Wiley, New York, 1990, p. 201.

[47] Lin, J.-S., Cabibil, H. and Kelber, J. A., *Surf. Sci.*, **395**, 30 (1998).

[48] Jennison, D. R., Verdozzi, C., Schultz, P. A. and Sears, M. P., *Phys. Rev. B*, **59**, R15605 (1999).

[49] Rosenhahn, A., Schneider, J., Kandler, J., Becker, C. and Wandelt, K., *Surf. Sci.*, **433-435**, 705 (1999).

[50] Kelber, J. A., Addepalli, S. G., Lin, J.-S. and Cabibil, H., P. Y. Hou, M. J. McNallan, R. Oltra, E. J. Opila and D. A. Shores, High Temperature Corrosion and Materials Chemistry, San Diego, CA, 1998, The Electrochemical Society, Inc., 98-99 (1998) 190.

[51] Lin, J.-S., Ekstrom, B., Addepalli, S. G., Cabibil, H. and Kelber, J. A., *Langmuir*, **14**, 4843 (1998).

[52] Wilhelm, S. M., Yun, K. S., Ballenger, L. W. and Hackerman, N., *Electrogenerated Chemiluminescence*, **126**, 419 (1979).

[53] Strehlow, W. H. and Cook, E. L., *J. Phys. Chem. Ref. Data*, **2**, 163 (1973).

[54] Zhang, Z. and Satpathy, S., *Phys. Rev. B*, **44**, 13319 (1991).

[55] Addepalli, S. G., Ekstrom, B., Magtoto, N. P., Lin, J.-S. and Kelber, J. A., *Surf. Sci.*, **442**, 385 (1999).

[56] Xu, C. and Goodman, D. W., *Chem. Phys. Lett.*, **263**, 13 (1996).

[57] Avouris, P., Walkup, R. E., Rossi, A. R., Shen, T.-C., Abeln, G. C., Tucker, J. R. and Lyding, J. W., *Chem. Phys. Lett.*, **257**, 148 (1996).

[58] Akpati, H. C., Nordlander, P., Lou, L. and Avouris, P., *Surf. Sci.*, **401**, 47 (1998).

[59] Persson, B. N. J. and Avouris, P., *Surf. Sci.*, **390**, 45 (1997).

CHAPTER 3

THEORY AND EXPERIMENTS ON THE STRUCTURE of 7 Å ALUMINA FILMS GROWN ON $Ni_3Al(110)$ *

3.1. Introduction

Since interactions between H_2O and heterogeneous catalysts are potentially important for understanding a multitude of reactions, many papers have probed H_2O interactions with alumina, a common support material [1-8]. Several studies involved the basal plane of α-Al_2O_3 or sapphire(0001) [1-5, 7, 8]. Though not a cleavage plane, it can be prepared for UHV studies. It is known that the sticking probability of H_2O to this surface at 300 K is essentially zero in UHV [2]. If the partial pressure of H_2O is raised to $\geq$ 1 Torr, however, the surface changes to one that is OH terminated [5]. This only minimally disturbs the deeper crystal because the old surface layer with three O-ions and one Al-ion per unit cell has a charge of 3-, just the same as the new OH-ion terminated surface. Indeed, all alumina exposed to ambient conditions is OH-terminated, with the clean surface 1/3 ML of Al-ions removed [5].

It has been shown that annealing the sapphire(0001) surface in UHV to 1200 K [3, 4] or even 1400 K [2] does not remove all OH. We speculate that this is because OH-

* This chapter is reproduced with permission from Elsevier (Journal of Molecular Catalysis A: Chemical). Reference: Qin, F., Magtoto, N.P., Kelber, J.A. and Jennison, D.R., *J. Molec. Catal. A*, **228**, 83 (2005).

ions are electrostatically bound and hence immobile, so nearest neighbor OH-ions are needed to react and release H_2O. Indeed, XPS shows about 1/3 ML of OH remains after annealing because at below this coverage, OH groups have no nearest neighbor hydroxyls with which to react. In order to study alumina supports without charging and to use all surface science tools such as STM, ultrathin (< 1 nm) films have been grown on nickel aluminides such as NiAl [9] and Ni_3Al [10, 11] by high temperature oxidation, which draws Al out of the substrate, but not Ni.

The most studied film is the 5 Å (or two O-layer) film on NiAl(110) [12]. As with sapphire, H_2O does not chemisorb on Al_2O_3/NiAl(110) in UHV at 300 K, and only one experiment created OH on this film by using a small deposition of Al metal, which formed islands to adsorb and dissociate water [6]. Since the earliest work on ultrathin alumina films on NiAl(110) [9], it has been known that a domain structure results because of a lattice mismatch between the overlaying alumina and the substrate. The exact structure of the film, however, has remained elusive in spite of many experiments that used it as a model for a heterogeneous catalyst support [12]. While the structural details of the film are unknown, STM has been able to show a hexagonal array of surface O-ions [13]. However, this is not definitive as several alumina phases have similar O-lattice structures and the vertical relief (buckling) could be mitigated by film thinness. In this early study, the Al-ions were invisible.

Finally, STM has been used to determine the adhesion between a Pd crystalline nanocluster and the film [14]. Indeed, the latter experimental breakthrough, made possible by collaboration between the Freund and Besenbacher groups, also stimulated a

theoretical collaboration concerning surface energy determination [15], which resulted in considerable recognition [16]. Theory and experiment agree on the work of adhesion; however, sapphire (α-alumina) was used in the theoretical work to model the oxide surface. The agreement between theory (sapphire(0001)) and experiment (5 Å Al_2O_3/NiAl(110)) suggests that these thinnest films (5 Å) [9] are either sapphire-like or indeed buckle less and thus behave (relax) differently than slightly thicker films grown on other substrates.

Very recently, CTR XRD by Stierle, *et al*. [17] provided definitive information on the Al-sublattice structure: by having equal amounts of tetrahedral and octahedral site Al-ions, the film resembles the A-plane of κ-alumina [18]. Improved STM experiments were also able to show the characteristic zig-zag rows of Al-ions in alternating sites [19]. These results were predicted by theory several years earlier by Jennison and Bogicevic [20], when DFT showed that distributing the Al-ions in this manner in the first layer was favored energetically over having all ions occupying the same type of site.

In order to understand interactions of oxide surfaces with the complex reaction environments relevant to catalysis, we must know the atomic structure of this film both on the surface and with depth. In this chapter, we address structural issues: 1) Does the preference for κ-alumina extend to thicker films, such as those with three O-layers? 2) What is the nature of the interface with the underlying nickel aluminide metals? 3) To what extent are these films accurate models for catalyst support materials? In order to probe these questions, we combine DFT calculations with STM, AES and LEED experiments done on a 7 Å (three O-layer) film. It has been known for some time that

films thicker than 5 Å can be grown, either on NiAl(100) [21] or on facets of Ni_3Al [10, 22, 23]. Here, using both STM and LEED, we examine one such film, on $Ni_3Al(110)$. We compare it to our first DFT calculation on a three O-layer film on a substrate of Al(111) and to the earlier prediction of phase [20] and to a conjecture concerning the oxide/metal interface [24].

3.2. Experimental Methods

Experiments were carried out in an Omicron UHV-STM system that has been described in section 2.2. The base pressure of the experimental ion/Ti sublimation-pumped chamber was 5×10^{-11} Torr after bake-out. The chamber was equipped with an Auger spectrometer from Physical Electronics (CMA 10-155), four-grid LEED optics (Omicron), and an ambient temperature STM (Omicron), as well as ion bombardment and gas dosing.

AES measurements were performed using the cylindrical mirror analyzer with a coaxial electron gun. Auger data were collected with an excitation beam energy of 3 KeV in the integral mode [N(E)] mode under computer control, and then differentiated [dN(E)/dE] and smoothed using a Savitzky-Golay program. Intensities were determined from peak-to-peak heights (pph) in derivative mode, and molar concentrations were calculated [25] using the pph and published atomic sensitivity factors [26] according to:

$$\frac{N_A}{N_B} = F_{AB}^{A} \times \frac{I_A / I_A^{\infty}}{I_B / I\infty_B} \qquad (3\text{-}1)$$

where N_A, I_A and I_A^∞, respectively, represent the molar concentration, Auger peak-to-peak height (pph) and the atomic sensitivity factor of element A. The Auger electron matrix factor F_{AB}^A for the element A in a homogeneous binary alloy AB can be estimated by considering backscattering effects and difference in mean free paths of A and B [25].

The thickness (d) of the oxide overlayer can be estimated according to [25]:

$$\frac{N_A}{N_B} = \frac{1-\exp[-d/\lambda_A(E_A)]}{\exp[-d/\lambda_B(E_B)]} \qquad (3\text{-}2)$$

where N_A and N_B are the atomic concentrations of the overlayer and substrate, respectively, and λ_A and λ_B are the mean free path length of element A and B respectively. In the AES experiments, the peak-to-peak heights (pph) of the $O_{(510)}$ and $Ni_{(848)}$ were used in calculating the thickness of the oxide film.

The $Ni_3Al(110)$ single crystal sample (MaxTek) had a diameter of 10 mm and a thickness of 0.5 mm, and was aligned to within ±1° of the (110) plane. The sample was spot-welded onto a tantalum plate that could be transferred between the manipulator and STM stage by a wobble-stick. While mounted on the manipulator, the sample could be heated from the rear by indirect resistive heating. A type K thermocouple was attached to a sample clip approximately 5 mm away from the sample. The difference between the actual temperature and the thermocouple reading was not calibrated. The samples were cleaned by repeated cycles of Ar^+ sputtering followed by annealing to 1100 K, until the surface was judged clean by AES, LEED and STM measurements.

Annealing to ~ 1100 K is necessary in order to recover the equilibrium surface composition since it is known that preferential sputtering of Al occurs [27]. The

$Ni_3Al(110)$ was then oxidized at ~ 900 K by backfilling the chamber with O_2 (Matheson, 99.9997% Purity) through a manual leak valve at a pressure of 1×10^{-6} Torr. High temperature oxidation was necessary since oxidation at room temperature followed by annealing to ~ 1100 K resulted in the disappearance of the O_{503} signal or the O(1s) XPS signal. This effect has been previously reported for $Ni_3Al(001)$ [28]. The sample was then annealed in UHV to obtain the well-ordered alumina thin film.

The DFT [29, 30] calculations were made with the Vienna *Ab initio* Simulations Package (VASP) [31-33] in the local density approximation (LDA) [34] and in the generalized gradient approximation (GGA) known as PW91 [34]. Because the former yields a slightly more accurate geometry for this system, it was used here. The ultrasoft pseudopotentials of Vanderbilt [35] describe this system to high accuracy with a plane wave cutoff of 396 eV. Because of the long-range electrostatic forces in oxide as opposed to metallic systems, we used a large vacuum gap between the slabs, which repeats along the ***c***-axis due to the plane wave basis set. We found ~ 15 Å or greater to be adequate.

3.3. Results

3.3.1. Clean $Ni_3Al(110)$

The $Ni_3Al(110)$ was cleaned by repeated cycles of Ar^+ sputtering followed by annealing to 1100 K, until a sharp LEED pattern was observed and the level of C and other contaminants was below the detectable AES limit (typically, $< \sim 10^{13}$ cm^{-2}). A STM image of the clean $Ni_3Al(110)$ is shown in Fig. 3.1a. Although no C or O was

observable for this sample by AES, STM indicated the continued presence of small islands typically 30-60 Å in diameter (probably associated with trace amounts of

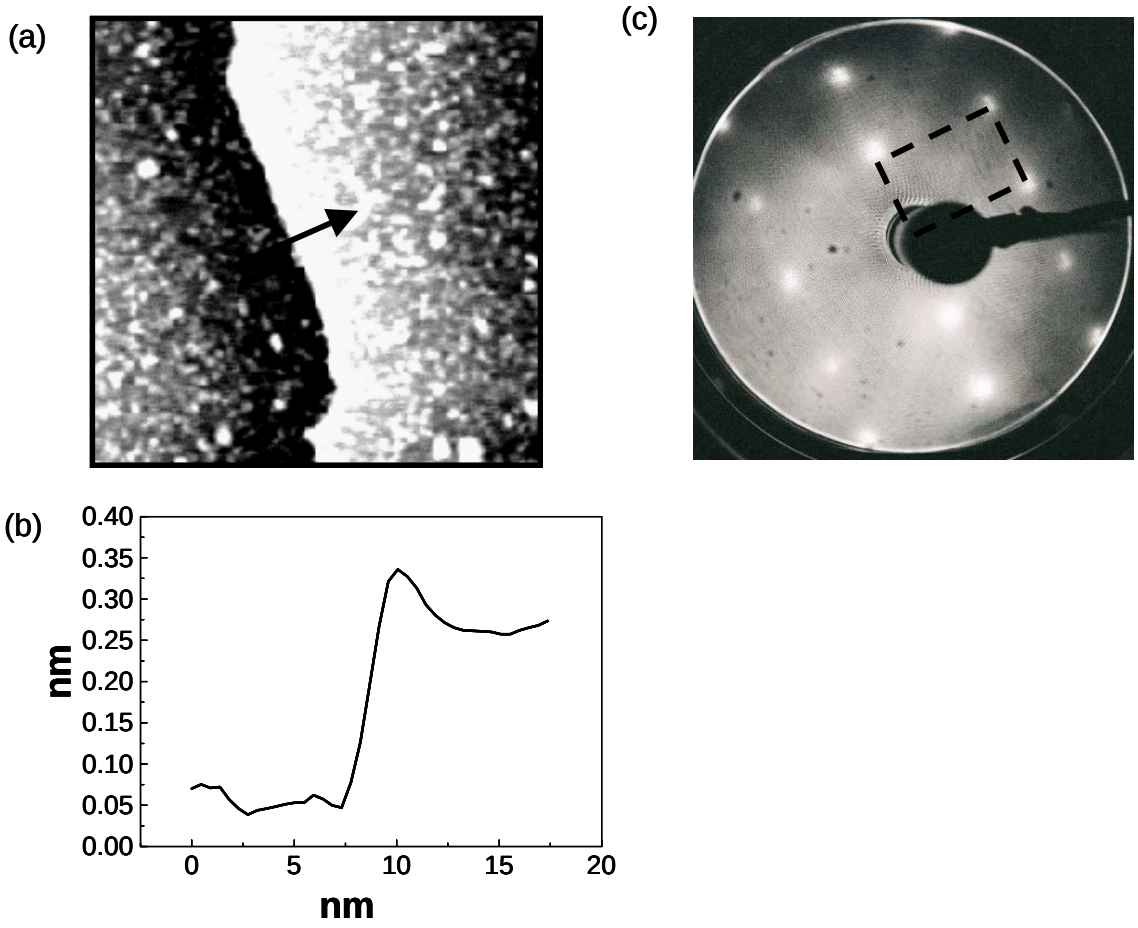

Fig. 3.1. (a) A 100 nm × 100 nm STM image of the clean $Ni_3Al(110)$ surface, bias voltage = 0.1 V, I = 0.1 nA; (b) A line profile of the surface which shows the measured step height of steps is consistent with an atomic step of 2.5 Å; (c) (1 × 1) LEED pattern of the surface, incident energy = 60 eV. The broken line rectangle indicates the (1 × 1) unit mesh.

chemisorbed oxygen) interspersed across the surface, in agreement with previously published results [11]. The measured height of the steps is consistent with an atomic step

of ~ 2.55 Å, indicated by the line profile shown in Fig. 3.1b. The clean sample displays a sharp 1 × 1 LEED pattern as in Fig. 3.1c. The lattice constants calculated from LEED are 3.56 Å along the [110] direction and 5.05 Å along [001] direction, in good agreement with the results of Cotterill et al. [11]. The relative atomic concentration of aluminum at the $Ni_3Al(110)$ surface was estimated (Eqn. 3-1) to be 0.25 ± 0.01, which corresponds to a bulk-like composition of aluminum atoms and demonstrates that no excess aluminum is present on the clean surface compared with the bulk.

3.3.2. AES of 7 Å $Al_2O_3/Ni_3Al(110)$

Clean $Ni_3Al(110)$ was oxidized at ~ 900 K by backfilling the chamber with O_2 (Matheson, 99.9997% Purity) through a manual leak valve at a pressure of 1×10^{-6} Torr, and the $O_{(510)}/Ni_{(848)}$ intensity ratio versus O_2 exposure was monitored by AES. The oxygen uptake curve (Fig. 3.2a) reveals that the saturation level is attained at ~ 400 Langmuir (L; 1 L = 10^{-6} Torr-sec), with an $O_{(510)}/Ni_{(848)}$ intensity ratio of ~ 0.9. Changes in the low energy Al and Ni AES spectral lineshapes during the oxidation of $Ni_3Al(110)$ are shown in Fig. 3.2b. Spectrum A in Fig. 3.2b represents a clean $Ni_3Al(110)$ sample, and exhibits the Ni (MVV) transition at 104 eV [22], the Ni ($M_{23}VV$) transition at 61 eV, and also a shoulder at 68 eV, which corresponds to the Al ($L_{23}VV$) transition [22]. The oxidation of aluminum is characterized by the shift of the metallic aluminum peak from 68 eV to 54 eV [36, 37], and the onset of a shoulder at 38 eV [36, 37]. In a similar manner, the oxidation of Ni is characterized by a shift of the Ni metallic peak at 61 eV to 53.5 eV [38]. Therefore, there is considerable overlap of Ni and Al oxide-related features

in the spectral region of 50-60 eV, making the detection of nickel oxidation problematic. Spectrum B in Fig. 3.2b was obtained after 500 L O_2 exposure of the $Ni_3Al(110)$ surface at 900 K. The oxidation of aluminum is indicated by the disappearance of the metallic Al

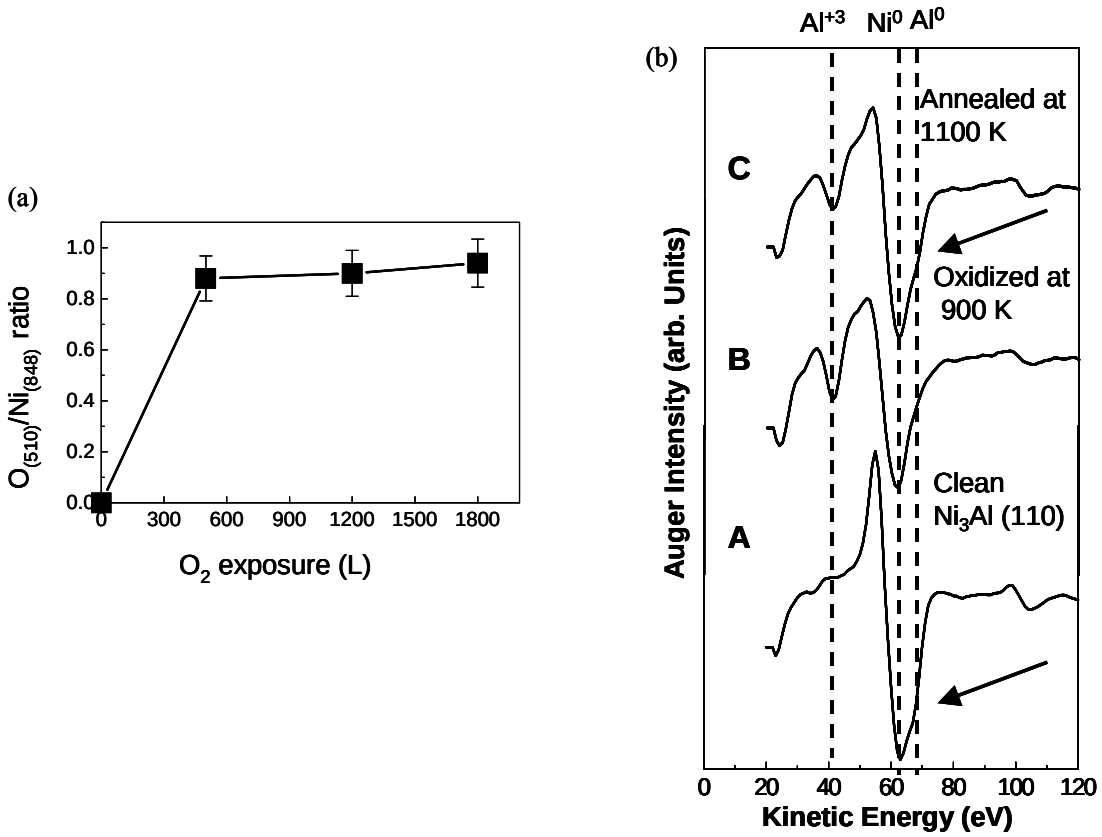

Fig. 3.2. AES analysis of the oxidation of Ni3Al(110) (The sample was oxidized at 900 K and annealed at 1100 K): (a) Change in the $O_{(510)}/Ni_{(848)}$ intensity ratio versus O_2 exposure on clean $Ni_3Al(110)$; (b) Low energy AES lineshape changes during the oxidation of $Ni_3Al(110)$.

peak (68 eV) and the appearance of the Al^{+3} peak at 38 eV [36, 37]. As shown in spectrum C in Fig. 3.2b, annealing the oxide grown at 900 K on clean $Ni_3Al(110)$ to 1100

K for 1 hour in UHV results in the reappearance of the Al^0 peak (68 eV) which indicates aluminum enrichment in the near-surface region. This is consistent with previous reports that an Al interfacial layer on Ni-Al alloys is stabilized by the presence of an Al_2O_3 overlayer [9, 22]. Using Eqn. (3-2), the thickness of the alumina layer was estimated to be ~ 7 Å.

3.3.3. Theoretical Studies of 7 Å $Al_2O_3/Ni_3Al(110)$

The κ-phase of alumina is the CVD phase. Since the A-plane results in a maximal spread of Al-ions in a monolayer, it is natural to suspect that this might serve as a template for further growth. Therefore, we computed a 7 Å (three O-layer) film. Because of the rotation of the film with respect to the underlying material (to relieve interfacial stress caused by a lattice mismatch), the unit cell is too large for computational study at present. Thus, we placed the film on a four layer Al(111) substrate, which has a minimal lattice mismatch. Because two studies (one on a film [20] and one on the sapphire/Al(111) interface [39]) showed that a true Al metal substrate would result in Al atoms crossing the interface and becoming chemisorbed on the oxide, the Al-metal substrate was frozen on the z-axis. Because the A-plane has maximal Al-ion separation and minimal buckling, it should have the lowest surface energy. Therefore, the theory calculation was A/B/O(111)/Al(111) where the O(111) was chemisorbed on the Al(111) surface (see below concerning structure with depth).

Fig. 3.3 shows the top and side views of the relaxed slab computed using DFT. X" marks the largest interstitial sites, which can contain atomic H (Ref. [40]) upon exposure

to water at sufficient pressures. The 2x1 unit cell (left) has its edges at the row tops, explicitly shown on the right. As shown nicely in a figure in Ref. [17], only the κ-phase has this cell. Thus we conclude that the 7 Å films are κ-like; i.e., are distorted versions of this phase. More distortion is found than Stierle, *et al.* [17] found for the thinner film, as is logical since the freedom to relax is less for the thinner film.

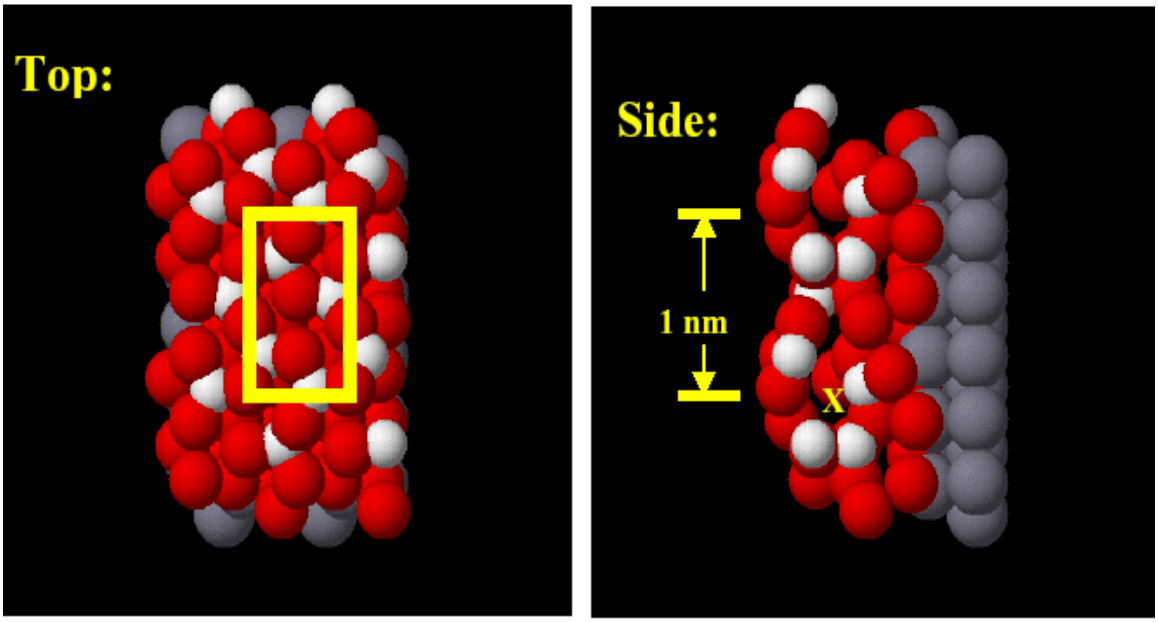

Fig. 3.3. Top and side views of the relaxed slab computed using DFT. "X" marks the largest interstitial sites. O-ions are red, Al-ions are white, and Al-metal atoms in the model substrate, necessitated by a lattice mismatch at the interface, are gray.

3.3.4. STM and LEED of 7 Å $Al_2O_3/Ni_3Al(110)$

Fig. 3.4 shows a near atomic-resolution constant current STM image (20 nm × 20 nm) obtained for the as-grown 7 Å $Al_2O_3/Ni_3Al(110)$. Clear rows are seen and the

distance between the rows, ~ 1 nm, is in good agreement with calculations for a kappa-phase structure as shown in Fig. 3.3. A 300 nm × 300 nm STM image of the $Al_2O_3/Ni_3Al(110)$ sample is shown in Fig. 3.5a. The as-grown $Al_2O_3/Ni_3Al(110)$ film

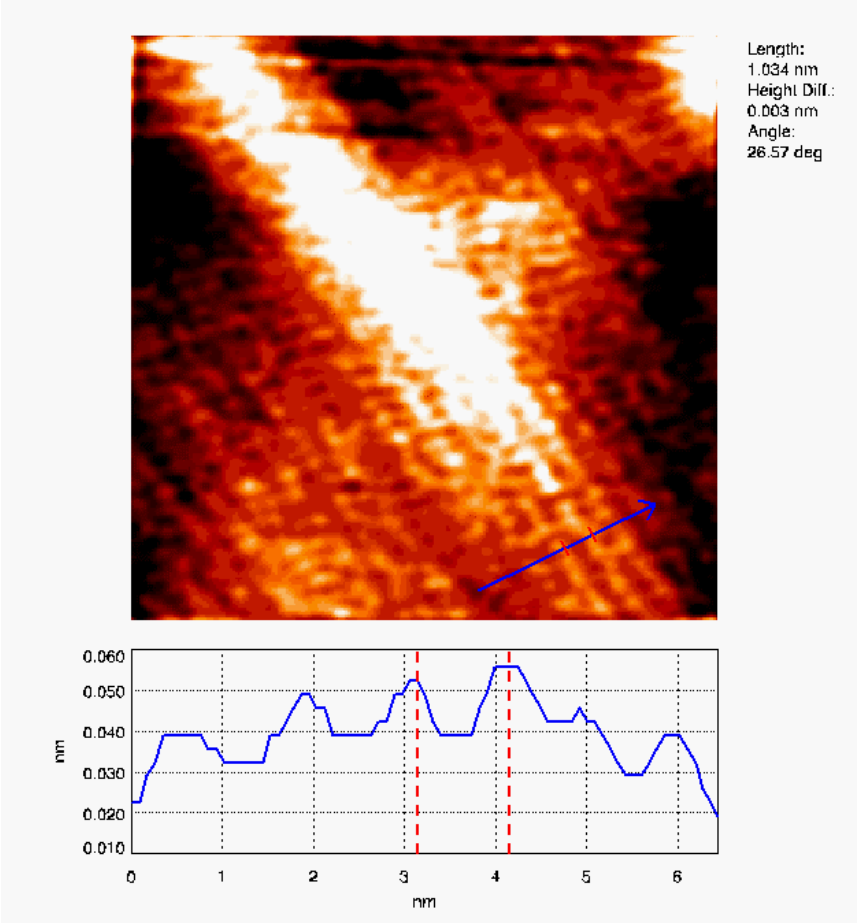

Fig. 3.4. Near atomic resolution, constant current STM image of the $Al_2O_3/Ni_3Al(110)$ film, showing the row structure and a row separation in agreement with the prediction of the calculation shown in Fig. 3.3.

consists of rows of oxide oriented along the [110] axis, but with random width along the [001] direction, consistent with the diffuse LEED scattering (Fig. 3.5b).

Formation of Al_2O_3 on top of the $Ni_3Al(110)$ substrate results in the appearance of diffuse scattering in the LEED pattern (Fig. 3.5b), attributed by Cotterill et al. [11] to the formation of an incommensurate oxide/metal interface. The film reported in the previous study consisted only of a chemisorbed oxygen phase on top of a metallic substrate [11], whereas the films discussed in this chapter (e.g., Fig. 3.5b) contain a true oxide phase, as evidenced by an Auger peak associated with the presence of Al^{+3} (Fig. 3.2b).

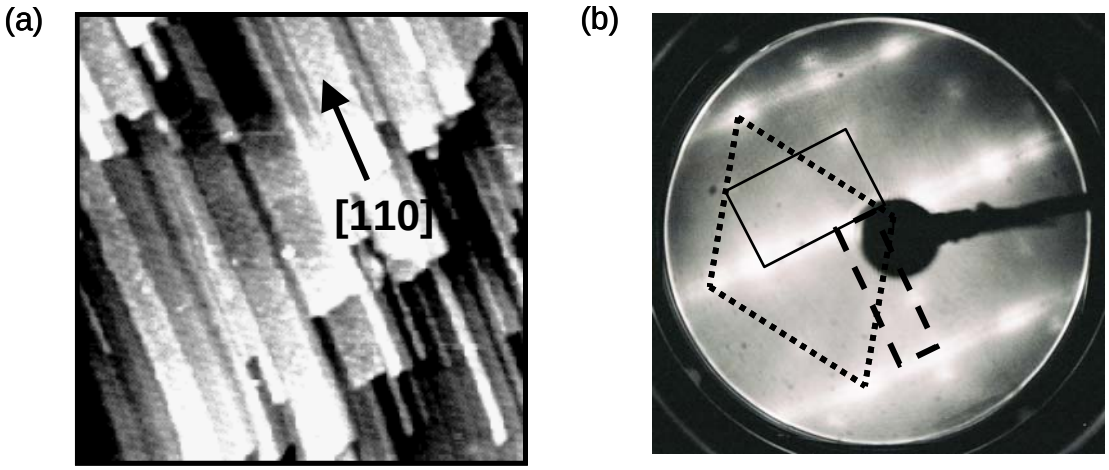

Fig. 3.5. (a) 300 nm × 300 nm STM image of the $Al_2O_3/Ni_3Al(110)$ (incommensurate reconstruction), bias voltage = 2 V, I = 0.1 nA. The surface is covered by a striped structure that runs along [110] direction. (b) LEED image of the $Al_2O_3/Ni_3Al(110)$, incident energy = 60 eV; Solid line rectangle indicates the 1 × 1 mesh of the substrate. Broken line rectangle and broken line hexagonal represent the unit meshes of the oxide-induced reconstruction. Al_2O_3 film was grown on top of the $Ni_3Al(110)$ substrate via oxidizing the $Ni_3Al(110)$ at 900 K followed by annealing to 1100 K.

The LEED pattern in Fig. 3.5b is a clear superposition of three structures. Due to the extremely thin nature of the alumina overlayer, the 1 × 1 mesh of the $Ni_3Al(110)$ substrate is still observed as indicated by the solid line rectangle in Fig. 3.5b. Analysis of

the LEED pattern (Fig. 3.5b) indicates an overlayer that is incommensurate with the metal substrate. The overlayer consists of a hexagonal mesh with a lattice constant of 2.9 ± 0.1 Å (shown by the broken line in Fig. 3.5b) and a weaker rectangular mesh (broken rectangular line), which corresponds to spacings of 3.0 ± 0.1 Å along [110] direction and 10.2 ± 0.1 Å along [001] direction [11]. The pseudo-rectangular structure is the small κ-alumina signature. The hexagonal structure is the octahedral O(111)/Al(111) pattern, which supports the previous conjecture [24] as shown in Fig. 3.6. The fact that the oxide overlayer is not commensurate with the metal substrate indicates that the chemical bonding within the surface layer is much stronger than the bond strength normal to the surface [11].

In Fig. 3.6 we see a conjecture made by Jennison et al. several years ago concerning the interface between alumina films and nickel aluminide substrates [24]. It was proposed [24] that there would be chemisorbed oxygen (1 ML) on Al(111), which has been drawn out of the substrate. The logic was that less energy would be needed to rotate Al(111) on a nickel aluminide substrate (metal on metal) than oxide on metal in order to relieve the lattice mismatch.

3.4. Discussion

The bimetallic compounds contain Al as a source for alumina formation by surface segregation during the oxidation process. In addition, the intermetallic compounds, NiAl and Ni_3Al, exhibit well ordered low indexed surfaces which show bulk stoichiometry. Therefore, they are suitable substrates for studying the oxygen adsorption

and the initial stage of oxide formation. A complex group of oxides including NiO, $NiAl_2O_4$, and Al_2O_3 have been formed on NiAl and Ni_3Al surfaces when oxidizing the samples at atmospheric pressure [41, 42]. In contrast, the preferred oxide on these surfaces is only Al_2O_3 at low oxygen pressures under UHV conditions [43, 44].

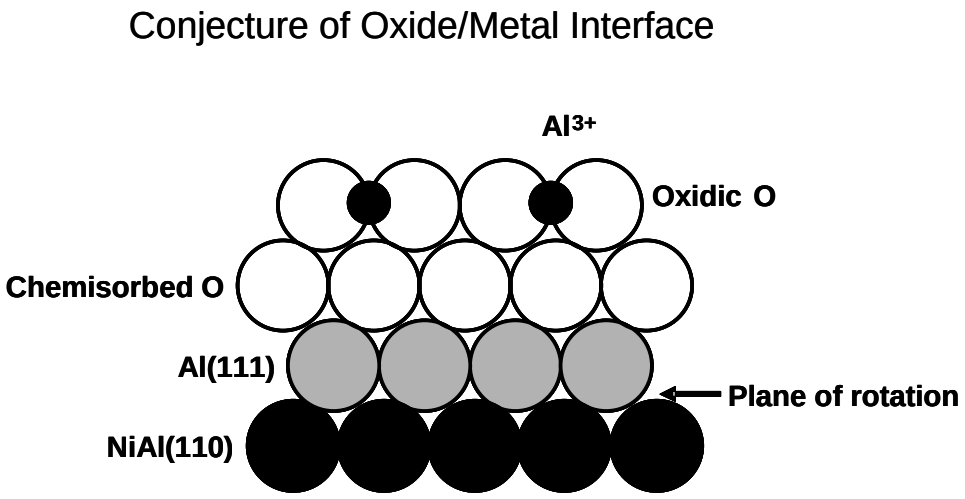

Fig. 3.6. The original conjecture of a structure having alumina and chemisorbed O on Al(111), rotated on nickel aluminide substrates.

Alumina, or Al_2O_3, exhibits a number of different phases, e.g. α, β, γ, η, θ, and κ alumina [18]. The α-Al_2O_3 is the thermodynamically stable phase, which has only octahedrally coordinated Al cations [45]. The presence of tetrahedrally coordinated Al cations in the structure is common to all or most of the transitional phase alumina, as opposed to α-phase [45]. The films discussed here are κ-like, but other transitional phase films can be grown by variations in oxidation procedure or annealing temperature [46, 47]. A question of considerable importance is the extent to which the κ-like or other

transitional phase thin alumina films grown on single crystal aluminide substrates are actual models for the amorphous gamma-like alumina generally used as a catalyst support. Experimental [46, 47] and theoretical studies indicate that the various transitional (non-α) phases differ from each other only in terms of relative octahedral vs. tetrahedral site occupancy and share many common characteristics regarding density and structure.

In addition, recent agreement between electrochemistry results for amorphous alumina films grown on Al(111) and DFT calculations on a κ-phase model indicate that the kappa film is an excellent model for amorphous alumina [40]. In contrast, vibrational studies of probe molecules at various oxide surfaces under UHV conditions indicate systematic variation in acid/base surface properties with annealing temperature and the transitional phase produced [46, 47]. A recent study of high resolution electron energy loss spectroscopy (HREELS) study of a thin, amorphous γ-like alumina film indicated only two different types of surface hydroxyl sites on the thin film surface (i.e., different pK_a values), as opposed to five observed for amorphous alumina powders. The preponderance of evidence therefore seems to be that all transitional phase alumina films manifest strong similarities in reactivity, electronic properties and structure, but that differences in surface acid/base properties are revealed by detailed measurements under UHV conditions. The extent to which differences in UHV-stable surface structures result in differences in reactivity and supported metal particle behavior under complex catalytic environments is an outstanding challenge for modern surface science.

3.5. Conclusions

STM, LEED, AES and DFT calculations were used to study the oxidation of $Ni_3Al(110)$. The results demonstrate that structure of the 7 Å alumina films on $Ni_3Al(110)$ is κ-like. An earlier theoretical prediction [20], a film which is κ-like, and a conjecture [24], 1 ML of $O_{(a)}$ on Al(111) at the interface, are now both supported by experiment. As-grown alumina films on $Ni_3Al(110)$ exhibit a true oxide layer with an incommensurate interface. With this knowledge of atomic structure, it is now possible to turn to the questions involving the interactions with H_2O, adsorption, dissociation, possible penetration of neutral H atoms into the film, and finally recombination and dissociation. Transitional phase alumina thin films grown on single crystal aluminides share many common structural, electronic and chemical characteristics with each other and with actual support materials. Despite systematic differences in surface acid/base properties revealed under UHV conditions, these alumina films appear sufficiently similar to amorphous catalyst supports to serve as tractable models for bridging the pressure gap between UHV surface science and realistic catalytic environments.

3.6. Chapter References

[1] Elam, J. W., Nelson, C. E., Cameron, M. A., Tolbert, M. A. and George, S. M., *J. Phys. Chem. B*, **102**, 7008 (1998).

[2] Ahn, J. and Rabalais, J. W., *Surf. Sci.*, **388**, 121 (1997).

[3] Kelber, J. A., Niu, C., Shepherd, K., Jennison, D. R. and Bogicevic, A., *Surf. Sci.*, **446**, 76 (2000).

[4] Niu, C., Shepherd, K., Martini, D., J.Tong, Kelber, J. A., Jennison, D. R. and Bogicevic, A., *Surf. Sci.*, **465**, 163 (2000).

[5] Eng, P. J., Trainor, T. P., G. E. Brown, J., Waychunas, G. A., Neville, M., Sutton, S. R. and Rivers, M. L., *Science*, **288**, 1029 (2000).

[6] Libuda, J., Frank, M., Sandell, A. and Freund, H.-J., *Surf. Sci.*, **384**, 106 (1997).

[7] Chambers, S. A., Droubay, T., Jennison, D. R. and Mattsson, T. R., *Science*, **297**, 827 (2002).

[8] Jennison, D. R. and Mattsson, T. R., *Surf. Sci.*, **544**, L689 (2003).

[9] Libuda, J., Winkelmann, F., Bäumer, M., Freund, H.-J., Bertrams, T., Neddermeyer, H. and Müller, K., *Surf. Sci.*, **318**, 61 (1994).

[10] Rosenhahn, A., Schneider, J., Becker, C. and Wandelt, K., *Appl. Surf. Sci.*, **142**, 169 (1999).

[11] Cotterill, G. F., Niehus, H. and O'Connor, D. J., *Surf. Rev. Lett.*, **3**, 1355 (1996).

[12] Baumer, M. and Freund, H.-J., *Prog. Surf. Sci.*, **61**, 127 (1999).

[13] Ceballos, G., Spong, Z., Pascual, J. I., Rust, H.-P., Conrad, H., Baumer, M. and Freund, H.-J., *Chem. Phys. Lett.*, **359**, 41 (2002).

[14] Hansen, K. H., Worren, T., Stempel, S., Laegsgaard, E., Baumer, M., Freund, H.-J., Besenbacher, F. and Stensgaard, I., *Phys. Rev. Lett.*, **83**, 4120 (1999).

[15] Mattson, A. E. and Jennison, D. R., *Surf. Sci.*, **520**, 611 (2002).

[16] Jacoby, M., *C & E News*, **80**, 4 November (2002).

[17] Stierle, A., Renner, F., Streitel, R., Dosch, H., Drube, W. and Cowie, B. C., *Science*, **303**, 1652 (2004).

[18] Yourdshahyan, Y., Reberto, C., Halvarsson, M., Bengtsson, L., Langer, V., Lundqvist, B. I., Ruppi, S. and Rolander, U., *J. Am. Ceram. Soc.*, **82**, 8265 (1999).

[19] Kulawik, M., Nilius, N., Rust, H. P. and Freund, H. J., *Phys. Rev. Lett*, **91**, 256101 (2003).

[20] Jennison, D. R. and Bogicevic, A., *Surf. Sci.*, **464**, 108 (2000).

[21] Blum, R.-P., Ahlbehrendt, D. and Niehus, H., *Surf. Sci.*, **396**, 176 (1998).

[22] Addepalli, S. G., Ekstrom, B., Magtoto, N. P., Lin, J.-S. and Kelber, J. A., *Surf. Sci.*, **442**, 385 (1999).

[23] Garza, M., Magtoto, N. P. and Kelber, J. A., *Surf. Sci.*, **519**, 259 (2002).

[24] Jennison, D. R., Verdozzi, C., Schultz, P. A. and Sears, M. P., *Phys. Rev. B*, **59**, R15605 (1999).

[25] Seah, M. P., Practical Surface Analysis, Wiley, New York, 1990.

[26] Davis, L. E., MacDonald, N. C., Palmberg, P. W., Raich, G. E. and Weber, R. E., Handbook of Auger Electron Spectroscopy, Physical Electronics Industries, Inc, Eden Prairie, MN, 1979.

[27] Shen, Y. G., O'Connor, D. J. and McDonald, R. J., *Surf. Interf. Anal.*, **18**, 729 (1992).

[28] Shen, Y. G., O'Connor, D. J. and MacDonald, R. J., *Surf. Interf. Anal.*, **17**, 903 (1991).

[29] Hohenberg, P. and Kohn, W., *Phys. Rev.*, **136**, B864 (1964).

[30] Kohn, W. and Sham, L. J., *Phys. Rev.*, **140**, A1133 (1965).

[31] Kresse, G. and Hafner, J., *Phys. Rev. B*, **47**, 558 (1993).

[32] Kresse, G. and Hafner, J., *Phys. Rev. B*, **49**, 14251 (1995).

[33] Kresse, G. and Furthmüller, J., *Phys. Rev. B*, **54**, 11169 (1996).

[34] Perdew, J. P. and Zunger, A., *Phys. Rev. B*, **23**, 5048 (1981).

[35] Vanderbilt, D., *Phys. Rev. B*, **41**, 7892 (1990).

[36] Chen, J. G., Crowell, J. E. and J. T. Yates, J., *Phys. Rev. B*, **33**, 1436 (1986).

[37] Homeny, J. and Buckley, M. M., *Mater. Lett.*, **9**, 443 (1990).

[38] Roberts, R. H. and Ramsey, J. A., *J. Electron Spectrosc.*, **52**, 185 (1990).

[39] Siegel, D., Louis G. Hector, J. and Adams, J. B., *Phys. Rev. B*, **65**, 85415

[40] Jennison, D. R., Schultz, P. A. and Sullivan, J. P., *Phys. Rev. B.*, **69**, 041405(R) (2004).

[41] Young, E. W. A., Rivière, J. C. and Welch, L. S., *Appl. Surf. Sci.*, **28**, 71 (1987).

[42] Venezia, A. M. and Loxton, C. M., *Surf. Interface Anal.*, **2**, 287 (1988).

[43] Venezia, A. M. and Loxton, C. M., *Surf. Sci.*, **194**, 136 (1988).

[44] Bardi, U., Atrei, A. and Rovida, G., *Surf. Sci.*, **268**, 87 (1992).

[45] Ruberto, C., Yourdshahyan, Y. and Lundqvist, B. I., *Phys. Rev. B*, **67**, 195412 (2003).

[46] Gassmann, P., Franchy, R. and Ibach, H., *Surf. Sci.*, **319**, 95 (1994).

[47] Lee, M. B., Lee, J. H., Frederick, B. G. and Richardson, N. V., *Surf. Sci.*, **448**, L207 (2000).

CHAPTER 4

H_2O-INDUCED INSTABILITY OF $Al_2O_3/Ni_3Al(110)$ AND $Al_2O_3/Ni_3Al(111)$ THIN FILMS UNDER NON-UHV CONDITIONS

4.1. Introduction

The structures and reactivities of alumina surfaces are of exceptional significance in a broad range of applications, including catalysis, micro- and nano-electronics, high temperature corrosion inhibition, optics, etc. [1-3]. Most such applications involve transitional (non-alpha) phase alumina films in contact with non-UHV environments, rather than the frequently studied sapphire(0001) surface [4, 5].Well-ordered alumina films grown on Ni-Al single crystal substrates—frequently used as model systems in surface science investigations—are of various transitional phases, depending on the details of the oxidation and annealing process [6]. These films include: $Al_2O_3/Ni_3Al(110)$ (κ-phase) [7, 8], $Al_2O_3/Ni_3Al(111)$ (γ'-phase) [9-11], $Al_2O_3/NiAl(001)$ (θ-phase) and ultrathin $Al_2O_3/NiAl(110)$ (κ-phase) [12].

Experimental and theoretical evidence indicate that the reactivities of alpha aluminas are distinct from those of the transitional phases (gamma, kappa, etc.), and that the transitional phases share strong similarities in terms of oxygen lattice structure and density [6, 13]. The room temperature spallation of alumina scales from aluminide substrates affects the various transitional phases, but not alpha-alumina [14]. Catalytic

activities observed for transitional aluminas decrease dramatically or cease altogether upon formation of the alpha phase [15]. Experimental [16] atomic-level studies of metal/oxide adhesion strongly suggest that adhesion at the metal/sapphire interface differs significantly from that for transitional phase oxides due to the greater relaxation possible with transitional phases. In summary, although detailed surface acid/base properties of the various transitional phases show systematic differences [17], the transitional phases show distinct similarities in behavior which sets them apart from the alpha phase.

Water is perhaps the most important and most pervasive adsorbate on our planet since it appears in so many interfacial systems. The moisture-induced spallation of alumina scales from Ni- or Fe- based Al alloys is a serious problem in the development of materials for advanced high temperature applications. Typically, such scales are formed by oxidation of the alloy at high temperature, but spallation is observed upon exposure to moisture or water immersion at ambient temperatures [3, 18-20], as well as at elevated temperatures during cyclic oxidation [21-23]. This phenomenon has been the subject of investigation from a mechanistic point of view [3, 22] but relatively little is understood of the relevant surface/interfacial chemistry. Although the interface in question is commonly assumed to be metal/α-alumina, due to annealing temperatures involved, recent localized diffraction and microscopy measurements [14] clearly demonstrate that transitional phases are often present at the interface, due to kinetic factors such as local variations in surface composition (i.e., impurities, coatings, aluminum concentration near the interface), or possibly topography. Previous studies of moisture effects on spallation

during cyclic oxidation [21, 23] indicate that the presence of moisture can result in changes in interfacial "toughness". There is no atomic-level understanding, however, as to the changes in interfacial chemical or physical structure associated with such a decrease in toughness. As a first step in acquiring such an understanding, we have used surface science techniques to probe the interactions at room temperature of H_2O with ordered transitional phase alumina films grown on single crystal Ni_3Al substrates. Subsequent studies will examine effects at elevated temperatures and on α-alumina films.

Although oxide scales in practice often have thicknesses > 1 μm, the oxide films in this study are typically < 1nm thick (although essentially similar behavior has been observed for films ~1.8 nm thick [7]), the extremely thin nature of such films allows surface science techniques, including XPS, LEED and STM to directly probe H_2O-induced changes in chemical bonding and structure at the well-ordered metal/oxide interface. A high degree of caution is obviously needed in extrapolating such results to "real world" spallation phenomena. Surface science studies such as this represent an initial step in obtaining precise information concerning a set of extremely complex phenomena. The results reported here, however, indicate a surprising reaction between H_2O molecules and transitional aluminas; a pressure-dependent reconstruction which begins at surface defect sites and gradually results in severe morphological reconstruction and roughening of the alumina film, even at 300 K.

The interaction of ordered α-phase and metastable alumina surfaces with H_2O has been the subject of extensive theoretical [13, 24-27] and experimental [1, 2, 4, 5, 12, 28-30] study within the surface science community. An important point is that most

experimental surface science studies of environmental interactions at alumina surfaces have been conducted under ultra-high vacuum (UHV) conditions, and alumina films under such conditions display a general inertness towards reaction with H_2O vapor, except at defect sites [12, 31]. Dissociative chemisorption of H_2O and the formation of a hydroxide phase is observed only for $P_{H_2O} > 1$ Torr for α-Al_2O_3(0001) [4, 5]. X-ray photoelectron spectroscopy (XPS) data [7] obtained for a thin alumina film grown on Ni_3Al(110), however, strongly suggested that that oxide film was structurally unstable upon exposure to P_{H_2O} of ~ 10^{-4} Torr, 300 K, even though aluminum hydroxide was only observed after exposures to P_{H_2O} ~ 1 Torr, 300 K. Although "real world" spallation phenomena usually involves $P_{H_2O} >> 1$ Torr [3, 18-20], the issue of technological relevance, however, is the effective P_{H_2O} at or near the interfacial spallation zone, or how a certain external level of humidity results in interfacial spallation. Our findings indicate that interfacial reactions may well be induced even if effective P_{H_2O} near the interface is well below 1 Torr.

In this chapter, STM, LEED, AES and XPS data are presented which confirm previous observations [7] and demonstrate that alumina films grown on Ni_3Al(111) and Ni_3Al(110) undergo drastic reorganization and reconstruction under extremely mild conditions: $P_{H_2O} > 10^{-5}$ Torr, 300 K. The film grown on the (110) substrate (κ-Al_2O_3/Ni_3Al(110)) is significantly more sensitive to H_2O vapor than the γ'-Al_2O_3/Ni_3Al(111) film, and this may be due to the incommensurate nature of the oxide/Ni_3Al(110) interface. This instability, or surface reconstruction, is not associated

with formation of a surface hydroxide, yet is specific to H_2O. Similar O_2 exposures have no effect. The data also show that the H_2O-induced reconstruction is pressure-dependent rather than exposure-dependent, and that the oxide instability is initiated at the oxide surface, rather than at the oxide/metal interface.

4.2. Experimental Methods

The experiments were carried out in two separate ultrahigh vacuum (UHV) systems. The AES, LEED, and STM measurements were performed in an Omicron UHV-STM system. Details of this system, and the preparation of W tips, have been described in section 2.2. A turbomolecularly pumped sample introduction chamber (base pressure, 5×10^{-10} Torr) was attached to the experimental chamber and separated from it by a gate valve. Sample transport between the two chambers occurred under controlled UHV conditions, and exposure to H_2O vapor was carried out in the introduction chamber. Long term (> 2 hours) exposures in the introduction chamber resulted in a total carbon contamination of < 0.05 monolayer, as determined by AES. Although this *ex-situ* methodology allows higher pressure (> 10^{-7} Torr) exposures than in UHV, the before/after STM measurements invariably sample different regions of the oxide surface. Therefore, care was taken during each STM measurement to acquire multiple large area (300 nm × 300 nm) scans in order to determine that the observed effects were representative of the surface as a whole. STM measurements were carried out in constant current mode at room temperature with the tip typically biased negative relative to the sample.

The XPS measurements were carried out in a separate system as shown schematically in Fig. 4.1. This system consists of a sample introduction chamber (base pressure, 2×10^{-9} Torr) and an experimental chamber (base pressure, 1×10^{-10} Torr) equipped with a hemispherical electron energy analyzer (VSW) for XPS and 3-grid LEED optics (Omicron), an unmonochromated x-ray source (Physical Electronics) and an ion gun (Specs) for sample cleaning. XPS spectra were acquired using Mg Kα radiation, with a constant analyzer pass energy of 22 eV.

The same Ni_3Al (110) and Ni_3Al (111) single crystals were used for both XPS and STM/AES/LEED studies. The Ni_3Al(110) single crystal sample (MaxTek) had a diameter of 10 mm and a thickness of 0.5 mm, and was aligned to within ±1° of the (110) plane. The Ni_3Al(111) single crystal sample (MaxTek) had a diameter of 10 mm and a thickness of 0.5 mm and it was polished on one side with an orientation miscut angle < 0.25°. Each sample was spot-welded onto a tantalum plate that could be transferred between the manipulator and STM stage by a wobble-stick. The samples were cleaned by repeated cycles of Ar^+ sputtering followed by annealing to 1100 K, until the surface was judged clean by AES, LEED and STM measurements.

Annealing to ~ 1100 K is necessary in order to recover the equilibrium surface composition since it is known that preferential sputtering of Al occurs [32]. The Ni_3Al(110) was then oxidized at ~ 900 K by backfilling the chamber with O_2 (Matheson, 99.9997% Purity) through a manual leak valve at a pressure of 1×10^{-6} Torr. High temperature oxidation was necessary since oxidation at room temperature followed by annealing to ~ 1100 K resulted in the disappearance of the O_{503} signal or the O(1s) XPS

signal. This effect has been previously reported for $Ni_3Al(001)$ [33]. The $Ni_3Al(111)$ was oxidized at room temperature by backfilling the chamber with O_2 (Matheson, 99.9997% purity) through a manual leak valve at a pressure of 1×10^{-6} Torr. The sample was then

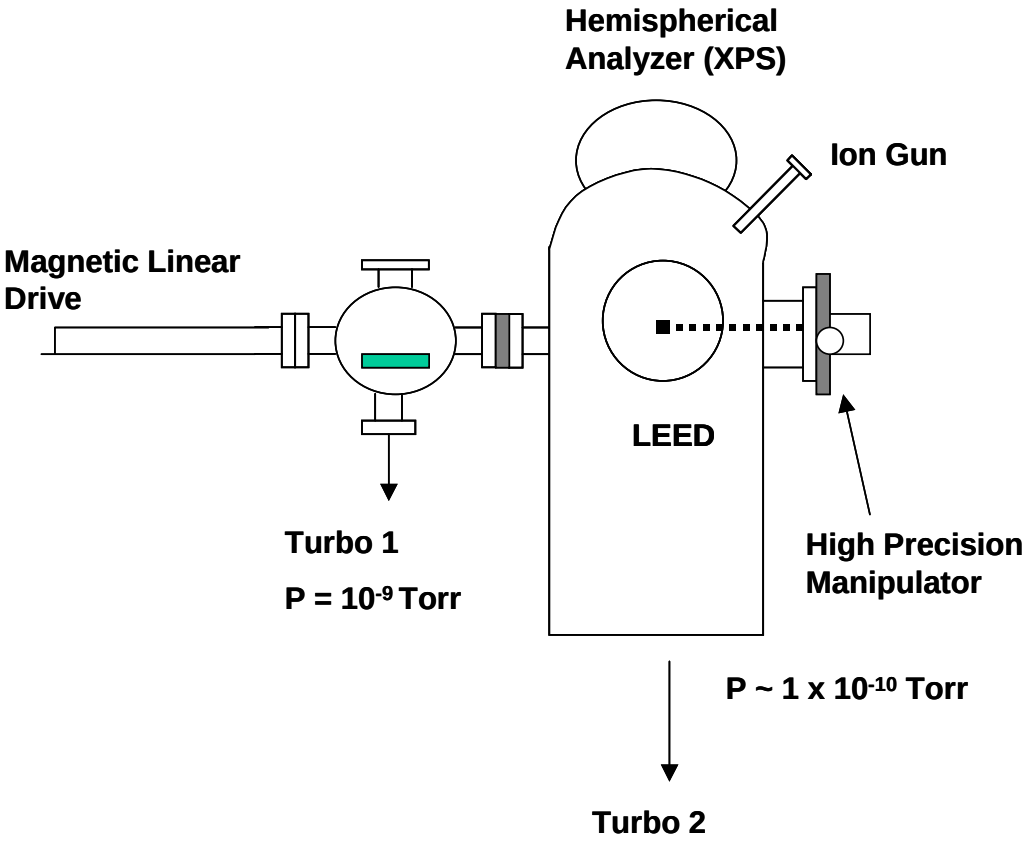

Fig. 4.1. The UHV/XPS system used in this study. The system is equipped with XPS and LEED.

annealed in UHV to obtain the well-ordered alumina thin film. Millipore grade water was used in the H_2O exposure experiments and was purified by several freeze-pump-thaw cycles.

The thickness (d) of the oxide overlayer can be estimated according to [34]:

$$\frac{N_A}{N_B} = \frac{1-\exp[-d/\lambda_A(E_A)]}{\exp[-d/\lambda_B(E_B)]} \quad (4\text{-}1)$$

where N_A and N_B are the atomic concentrations of the overlayer and substrate, respectively, and λ_A and λ_A are the mean free path length of element A and B respectively. In the AES experiments, the peak-to-peak heights (pph) of the $O_{(510)}$ and $Ni_{(848)}$ were used in calculating the thickness of the oxide film. In the XPS experiments, the Ni ($2p_{3/2}$) and O(1s) intensities were used in calculating the thickness of the oxide film.

4.3. Results

4.3.1. Oxidation of $Ni_3Al(110)$ and $Ni_3Al(111)$

Al_2O_3 films were grown on $Ni_3Al(110)$ by exposure to O_2 at $1\square 10^{-6}$ Torr for 8.5 minutes (500 L, saturation level) at 900 K followed by annealing to 1100 K for 60 minutes in UHV. High temperature oxidation of $Ni_3Al(110)$ was necessary since oxidation at room temperature followed by annealing to ~1100 K in UHV resulted in the disappearance of the O_{503} Auger signal or the O(1s) XPS signal as previously reported [7]. $Al_2O_3/Ni_3Al(111)$ films were grown by exposure to $1\square 10^{-6}$ Torr of O_2 for 12 minutes (700 L, saturation level) at 300 K followed by annealing to 1100 K in UHV for 60 minutes. AES revealed no significant carbon contamination and XPS revealed no observable hydroxide formation after the oxidation procedures. Previous studies on sapphire(0001) indicate that sensitivities to C and OH coverage with these procedures are ~ 0.01 and 0.1 ML (ML: monolayer), respectively [5].

Detailed information on $Al_2O_3/Ni_3Al(110)$ STM, LEED and AES were reported in section 3.3.1. Constant current STM and LEED images of the $Al_2O_3/Ni_3Al(110)$ film were similar to those previously reported [35] except that Auger spectra showed the presence of Al^{+3} species, indicative of true oxide formation. High resolution STM and LEED data [8] indicate the formation of a Al(111) interface between the ultrathin oxide film and the $Ni_3Al(110)$ surface in agreement with a model of the incommensurate interface proposed by Cotterill et al. [35]. The experimental data are in agreement with first principles DFT results and indicate that the $Al_2O_3/Ni_3Al(110)$ film is κ-phase [8]. STM, LEED and AES for $Al_2O_3/Ni_3Al(111)$ were similar to those previously reported [9]. The thickness of the annealed oxide film grown on $Ni_3Al(111)$ was estimated to be 7 ± 1 Å using Eqn. (4-1). Formation of the Al_2O_3 on top of the $Ni_3Al(111)$ substrate results in an aluminum interface as evidenced by the AES data (not shown), which is consistent with the previous report [9]. As indicated by the LEED pattern (Fig. 4.2a) of the ordered oxide, two domains that are rotated at 37.5° (a, b) and 24.5° (c, d) with respect to the substrate coexist on the surface, consistent with earlier reports [9, 11]. A 300 nm × 300 nm STM constant current image of the $Al_2O_3/Ni_3Al(111)$ sample is shown in Fig. 4.2b. The typical step height is equal to 2.8-5.3 Å with terrace width ranging from 50 nm to 150 nm. The stoichiometries of the two films are similar, as manifested by O/Al AES peak-to-peak height ratios that are equal to within experimental error.

XPS spectra for the clean, oxidized and annealed Al_2O_3 film on $Ni_3Al(110)$ are shown in Fig. 4.3. Prior to oxidation (spectrum A), a single Al(2p) feature is observed, at 72.3 eV, corresponding to metallic aluminum ($Al(2p)^{metal}$) [7]. Exposing the sample to

500 L O_2 at 900 K results in the disappearance of the $Al(2p)^{metal}$ peak and replacement by a peak at higher binding energy (Spectrum B in Fig. 4.3a).

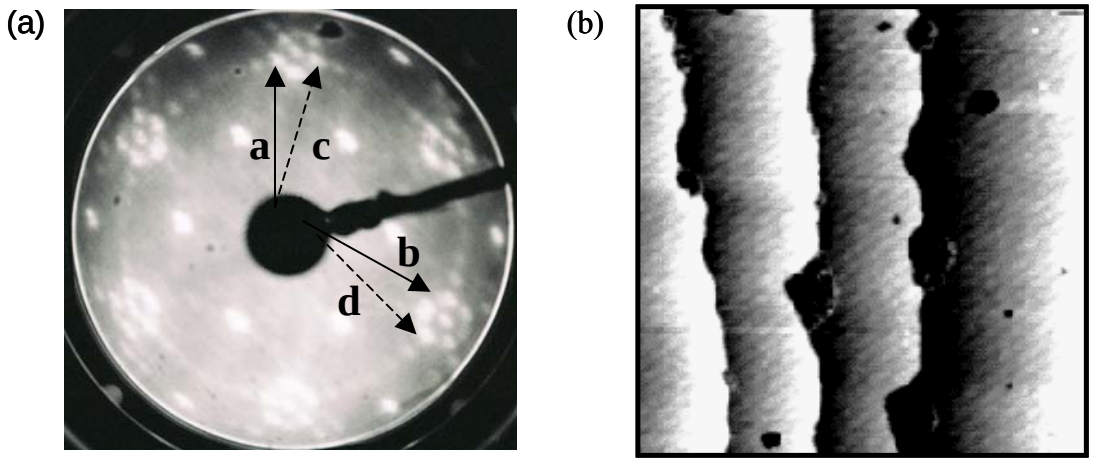

Fig. 4.2. (a) LEED image of the $Al_2O_3/Ni_3Al(111)$, incident energy = 60 eV. The arrows in the LEED pattern show the reciprocal unit vectors of the two domains which are rotated by 37.5° (a, b) and 24.5° (c, d), respectively relative to the orientation of the substrate. (b) 300 nm × 300 nm STM image of the $Al_2O_3/Ni_3Al(111)$ (Bias voltage = 2 V, I = 0.1 nA).

The corresponding O(1s) spectrum is shown in spectrum E of Fig. 4.3b. The O(1s) peak has a FWHM of 2.2 eV. This spectrum is well fit by two components, each with a FWHM of 1.72 eV, at binding energies of 530.3 eV and 531.3 eV. The 530.3 eV component is assigned to NiO [7, 36-38]. However, we cannot assign the peak at 531.3 eV to either NiO (530.3 eV [7, 36-38]) or Al_2O_3 (532.2 eV [7, 39, 40]). The corresponding Al(2p) spectrum (spectrum B in Fig. 4.3a) indicates a significant Al component with an oxidation state intermediate between the metal and the stoichiometric oxide (Al_2O_3). Hence, we assign the peak at 531.3 eV (and the corresponding Al(2p) feature near 75 eV) to an interfacial phase, denoted here as "AlO_x" [7, 41, 42]. Annealing

the oxide film to ~ 1100 K results in a shift in both the Al(2p) and O(1s) spectra to higher binding energies shown in spectra C and F, respectively. The Al(2p) spectrum of the oxide annealed at 1100 K is well fit with two components at binding energies of 74.8 eV (AlO_x) and at 75.7 eV (Al_2O_3) [7, 41, 42]. Therefore, the two O(1s) components in

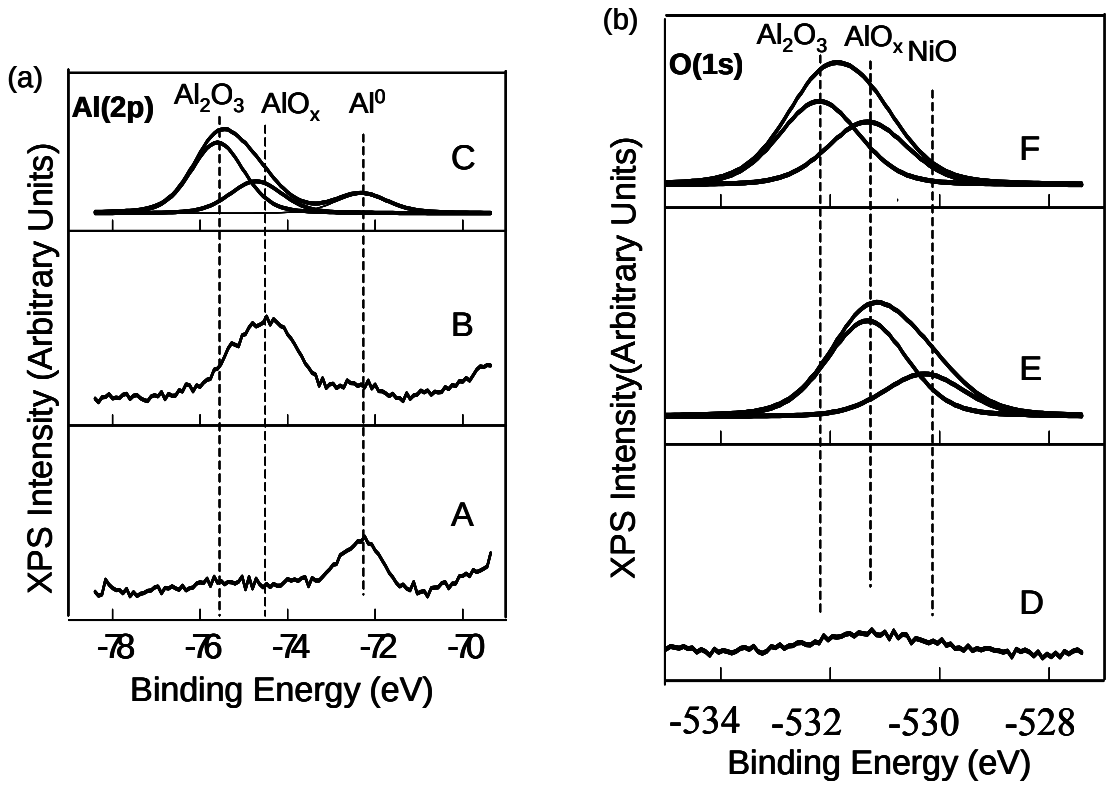

Fig. 4.3. Al(2p) and O(1s) XPS spectra for $Al_2O_3/Ni_3Al(110)$: A and D – preoxidized; B and E – oxidized, 1×10^{-6} Torr O_2 (500 L), 900 K; C and F – annealed oxide, 1100 K. Al_2O_3 film was grown on top of the $Ni_3Al(110)$ substrate via oxidizing the $Ni_3Al(110)$ at 900 K followed by annealing to 1100 K.

spectrum F of Fig. 4.3b are assigned to Al_2O_3 (532.2 eV), and AlO_x (531.3 eV) [7, 42]. In Fig. 4.3, there is no component in the O(1s) spectra observed under our experimental

conditions at a binding energy from 533.5 to 534.2 eV , which is 1.3-2 eV removed to higher binding energy from the Al_2O_3, that would indicate Al-(OH) formation [5, 39, 40].

Nickel is known to diffuse easily into bulk Ni_3Al at elevated temperatures [32, 43]. The disappearance of the NiO component (530.3 eV) upon annealing is therefore attributed to reduction of NiO followed by Ni diffusion into the bulk. Annealing the oxide to 1100 K also results in Al segregation to the near surface region, as manifested by the reappearance of the $Al(2p)^0$ peak shown in spectrum C, consistent with previous reports that the presence of an Al_2O_3 layer stabilizes an Al interfacial layer on Ni-Al alloys [7, 9, 44]. The thickness of the annealed oxide film grown on $Ni_3Al(110)$ was estimated to be 6.5 ± 1 Å using Eqn. (4-1). This is in good agreement with the AES-determined thickness of the $Al_2O_3/Ni_3Al(110)$ film grown in the STM/AES/LEED chamber. The presence of O_2 at elevated temperature is generally considered a crucial condition for $NiAl_2O_4$ formation at the Ni/Al_2O_3 interface [45]. Further, the experimental oxidation temperature of ~ 900 K used in our study is below the temperature needed for bulk $NiAl_2O_4$ formation (~ 1400 K, [46]). In addition, under our experimental conditions there is no component in the Ni(2p) spectra observed at a binding energy from 856 to 857 eV (not shown) that would indicate $NiAl_2O_4$ formation, in agreement with the results of previous studies [7, 45].

4.3.2. Exposure of $Al_2O_3/Ni_3Al(110)$ and $Al_2O_3/Ni_3Al(111)$ to Water Vapor

The 7 Å thick $Al_2O_3/Ni_3Al(110)$ film was exposed to water vapor at 10^{-4} Torr. All exposures were carried out at ambient temperature (~ 300 K). Fig. 4.4 displays the STM

images of the surface after exposing to water vapor for 5, 15 and 45 minutes. It has been demonstrated [28] that for thin oxide films on conductive substrates, STM constant current images acquired at low and high bias voltages are more sensitive to interfacial

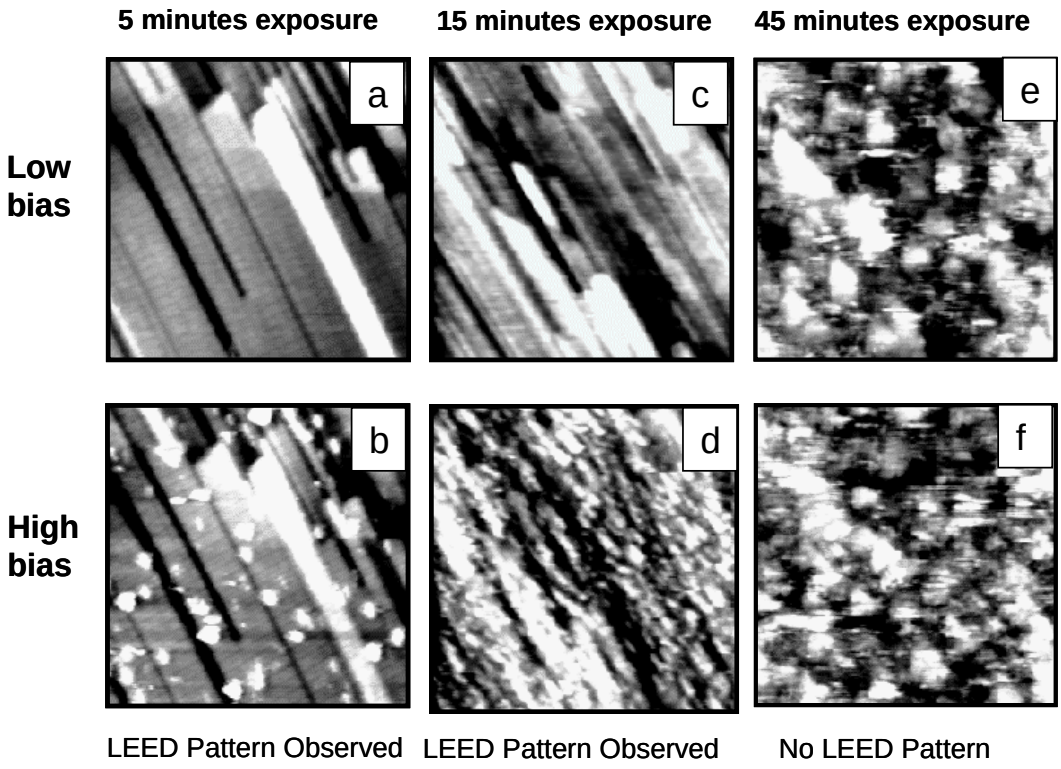

Fig. 4.4. 300 nm × 300 nm STM images of the $Al_2O_3/Ni_3Al(110)$ after exposing to water vapor pressure of $1x10^{-4}$ Torr for different times: (a) and (b)–5 minutes; (c) and (d)–15 minutes; (e) and (f)– 45 minutes; scanning parameters: (a), (c) and (e)– bias voltage = 0.1 V (low bias), I = 0.1 nA; (b), (d) and (f)– bias voltage = 2 V (high bias), I = 0.1 nA. Al_2O_3 film was grown on top of the $Ni_3Al(110)$ substrate via oxidizing the $Ni_3Al(110)$ at 900 K followed by annealing to 1100 K.

and oxide surface topographies, respectively. Hence the STM images (a, c and e in Fig. 4.4) obtained at low (0.1 V) scanning voltage and the STM images (b, d and f in Fig. 4.4) obtained at high voltage (2 V) highlight changes of the oxide/metal interface and oxide

surface, respectively, upon increasing exposure to water vapor of 10^{-4} Torr. After an exposure time of 5 minutes at $P_{H_2O} = 10^{-4}$ Torr, the interfacial region is unaffected (Fig. 4.4a), and isolated bright spots are visible at the oxide surface (Fig. 4.4b). The sample LEED pattern (not shown) is still intact at this point. The oxide surfaces undergo more severe reconstruction upon longer exposure (15 minutes) while the interface is still unaffected (Fig. 4.4c, d). The LEED pattern is fainter but still visible after the water dosing of 15 minutes. Both the oxide surface and the interface reconstruct upon water exposure of 45 minutes (Fig. 4.4e, f), and no LEED pattern is observed at this stage. The data in Fig. 4.4 (a-f) indicate that first, a roughening or reconstruction is initiated at the oxide surface rather than by diffusion into the interface; second, the roughening transformation progresses over gradually wider areas of the surface with increasing exposure time, rather than by a temporally abrupt transition.

The observation of surface instability only for P_{H_2O} above UHV strongly suggests that the reaction involves the cooperative interaction of several H_2O molecules at the surface. Molecular dynamics studies [26] indicate the feasibility of such reactions at α-Al_2O_3(0001) surfaces. Such cooperative reactions should be pressure-, rather than exposure- dependent, and the data in Fig. 4.5 indicate that this is the case. Constant current STM images of an Al_2O_3/Ni_3Al(110) films exposed to 270,000 L H_2O vapor at 10^{-5} Torr or at 10^{-4} Torr are compared in Fig. 4.5. Both the oxide surfaces undergo severe reconstruction at 10^{-4} and 10^{-5} Torr, as shown in Fig. 4.5b and Fig. 4.5d. However, at 10^{-5} Torr (Fig. 4.5a), the interfacial region is largely intact, and a LEED pattern is still observable at this point. In contrast, the same exposure at 10^{-4} Torr (Fig. 4.5c) results in

severe reconstruction of the interface region; no LEED pattern was observed for this sample. The STM images (Fig. 4.5a,c), acquired at 0.1 V tip/sample bias, indicate that the

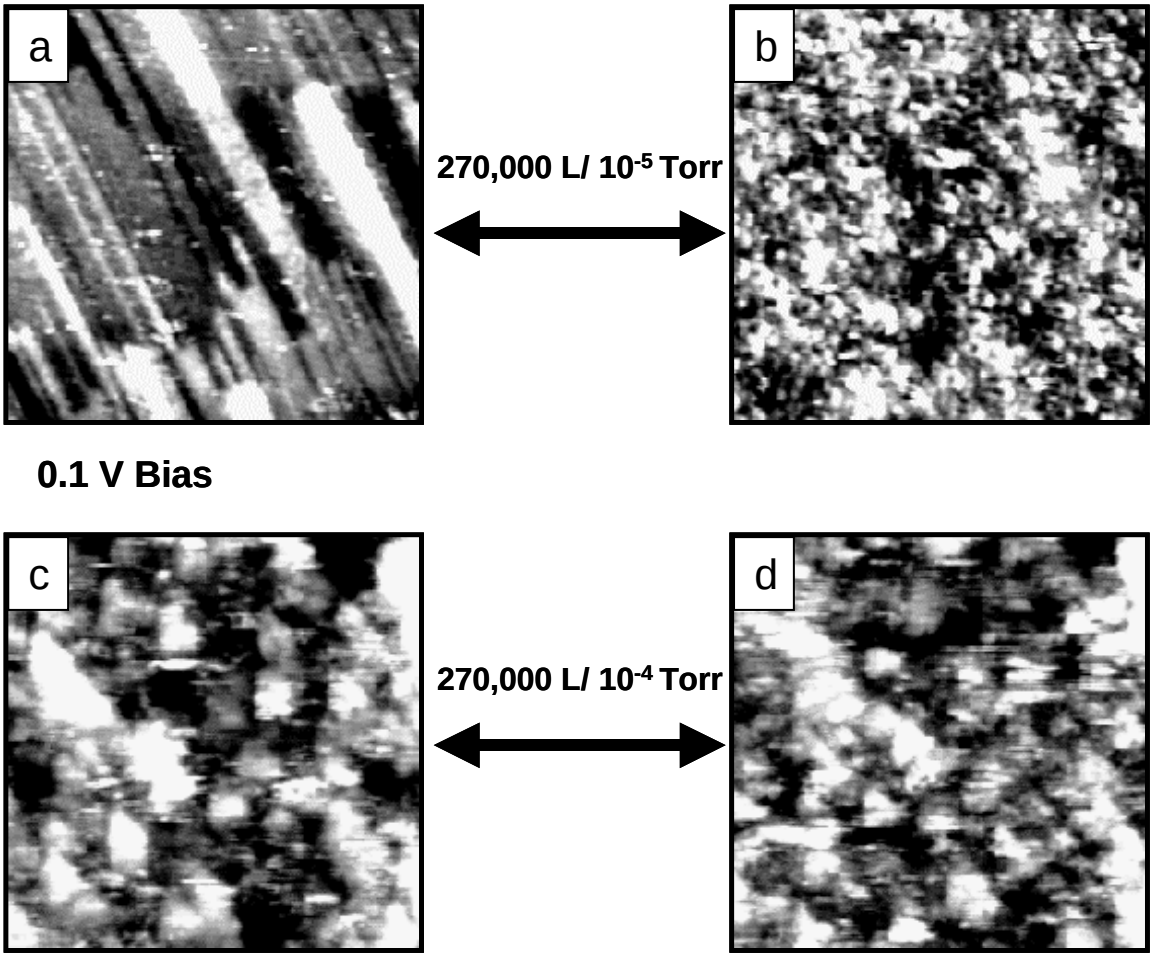

Fig. 4.5. 300 nm × 300 nm constant current STM images of the $Al_2O_3/Ni_3Al(110)$ after exposure to 270,000 L water vapor at different pressures: (a, b) pressure of 1×10^{-5} Torr for 450 minutes, 0.1 V and 2.0 V tip/sample bias, respectively; (c & d) pressure of 1×10^{-4} Torr for 45 minutes, 0.1 V and 2.0 V tip/sample bias, respectively. Al_2O_3 film was grown on top of the $Ni_3Al(110)$ substrate via oxidizing the $Ni_3Al(110)$ at 900 K followed by annealing to 1100 K.

H_2O-surface interaction is pressure- dependent rather than exposure- dependent.

Exposure, the product of pressure □ time, is proportional to the number of gas/molecule

surface interactions [47]. The data show that the process of surface reconstruction is *not* proportional to H_2O exposure. Equal exposures at different pressures yield different results (Fig. 4.5). This pressure dependence is further evidenced by the experiments conducted at H_2O vapor pressure of 10^{-3} Torr as shown in Fig. 4.6. The STM images in Fig. 4.6 were obtained after the $Al_2O_3/Ni_3Al(110)$ film was exposed to 90,000 L H_2O at 10^{-3} Torr (Fig. 4.6a) and 10^{-4} Torr (Fig. 4.6b). Although a reconstruction is observed in both cases, Fig. 4.6b indicates a less advanced reconstruction at 90,000L/10^{-4} Torr, since the regular features oriented along the (110) axis are still visible. The data in Figs. 4.5 and 4.6 demonstrate that equal exposures (L) result in a more severe reconstruction for the exposure carried out at higher pressure.

The different responses of Al_2O_3/Ni_3Al (110) (7.1 Å thick) and of $Al_2O_3/Ni_3Al(111)$ (7 Å thick) to P_{H_2O} = 10^{-4} Torr/270,000 Langmuir (L; 1 L = 1 Torr-sec^{-1}) are shown in Fig. 4.7. The as-grown $Al_2O_3/Ni_3Al(110)$ film (Fig. 4.7a) consists of rows of oxide oriented along the [110] axis, but with random width along the [001] direction, consistent with the diffuse LEED scattering [35]. The exposure to H_2O (10^{-4} Torr, 270,000 L) at 300 K results in severe roughening and randomization of the surface (Fig. 4.7b) coincident with the loss of any LEED pattern. In contrast, similar exposure of the $Al_2O_3/Ni_3Al(111)$ film (Fig. 4.7d) results in little significant surface reconstruction apparent in either the STM image (Fig. 4.7e) or LEED pattern (not shown). Isolated bright spots are apparent in the STM image of the $Al_2O_3/Ni_3Al(111)$ film after H_2O exposure, suggesting reaction at localized defect areas. At longer exposures (10^{-4} Torr, 90 minutes) roughening of the $Al_2O_3/Ni_3Al(111)$ film surface is observed (Fig. 4.7f), with no

LEED pattern observed at this point. The data in Fig. 4.7 demonstrate that Al_2O_3 films grown on $Ni_3Al(111)$ reconstruct at a much slower rate (or at longer exposure times) at equal pressures compared with $Al_2O_3/Ni_3Al(110)$ film of similar thickness. In order to test the specificity of the reaction toward H_2O, both the $Al_2O_3/Ni_3Al(110)$ and the $Al_2O_3/Ni_3Al(111)$ films are exposed to oxygen at 10^{-4} Torr for 45 minutes. The results (not shown) reveal that similar exposures to oxygen have no effect on either film, indicating that reactions at both film surfaces are specific to H_2O.

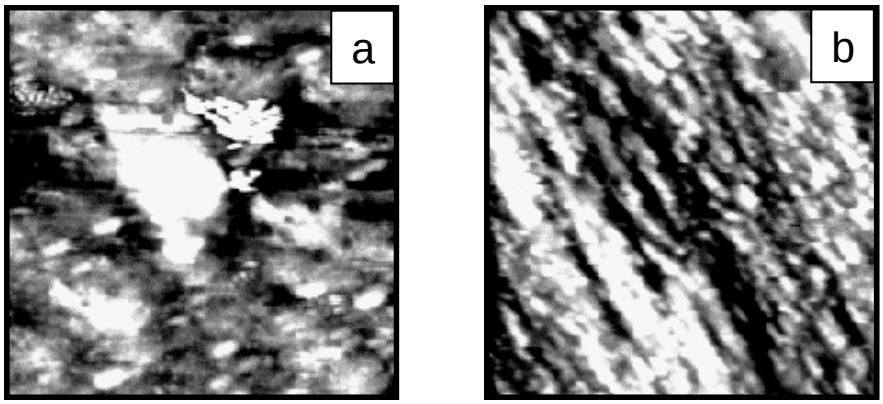

Fig. 4.6. 300 nm × 300 nm STM image of the $Al_2O_3/Ni_3Al(110)$ after exposing to water vapor to the same exposure at different pressures: (a) 1×10^{-3} Torr for 1.5 minutes; (b) 1×10^{-4} Torr for 15 minutes. Scanning parameter: bias voltage = 2 V, I = 0.1 nA.

XPS O(1s) and Al(2p) spectra of a 7.1 Å thick $Al_2O_3/Ni_3Al(110)$ film before and after H_2O exposure are displayed in Fig. 4.8. Spectra of the as-grown film are similar to those reported for other ultrathin alumina thin films [12] with O(1s) and Al(2p) components at higher binding energies attributed to lattice oxygen and aluminum ions, and components at lower binding energies assigned to less ionic, interfacial environments

[12, 13]. Upon exposure to H_2O, the relative intensities of the "oxide (Al_2O_3)" components of the O(1s) and Al(2p) spectra decrease significantly, while the relative

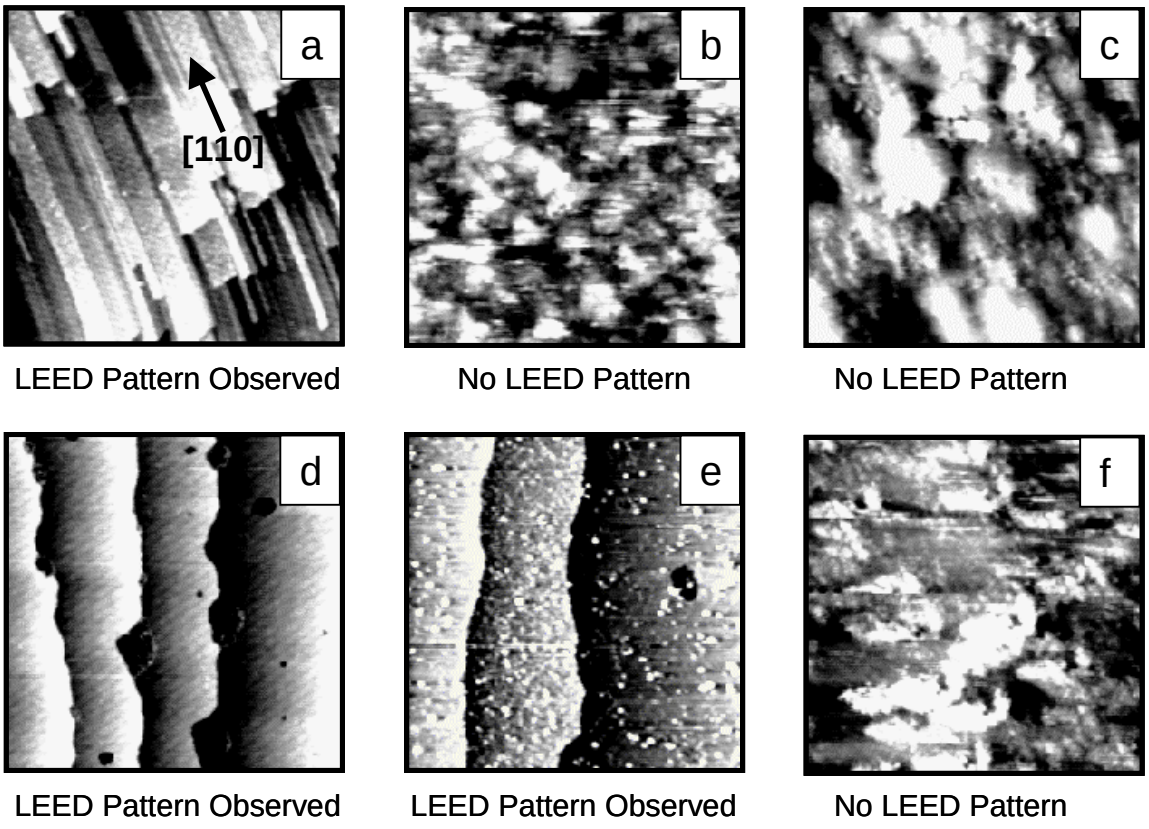

Fig. 4.7. 300 nm □ 300 nm STM constant current images of (a) a 7 Å thick as grown $Al_2O_3/Ni_3Al(110)$ film; (b) the $Al_2O_3/Ni_3Al(110)$ exposed to H_2O at 10^{-4} Torr, 45 minutes, 300 K; (c) the $Al_2O_3/Ni_3Al(110)$ exposed to H_2O at 10^{-4} Torr, 90 minutes, 300 K; (d) a 7 Å thick as-grown $Al_2O_3/Ni_3Al(111)$; (e) $Al_2O_3/Ni_3Al(111)$ after exposure to H_2O at 10^{-4} Torr; 45 minutes, 300 K; (f) the $Al_2O_3/Ni_3Al(111)$ exposed to H_2O at 10^{-4} Torr, 90 minutes, 300 K. Scanning parameters: Gap Voltage = 2 V, Current = 0.1 nA. [*]

[*] This figure is reproduced with permission from Elsevier (Surface Science). Reference: Qin, F., Magtoto, N.P., and Kelber, J.A., *Surf. Sci*, **565**, L277 (2004).

intensities of the corresponding "AlO_x" components increase. There is no change in the total O(1s) intensity before and after the water exposure. (No evidence of Ni oxidation or hydroxylation was observed.) The H_2O exposure results in *no* evidence of aluminum hydroxide formation, which would be manifested by a broadening of the O(1s) peak to higher binding energy [4, 7, 12]. (Based on previous XPS studies of hydroxylated alumina surfaces [5, 48], we estimate maximum hydroxyl coverage in UHV as < 10% of a monolayer.) The data in Fig. 4.7 and Fig. 4.8 indicate that the thin alumina film on $Ni_3Al(110)$ undergoes severe surface reconstruction upon exposure to $P_{H_2O} = 10^{-4}$ Torr, 300 K. These results are in general agreement with previously reported XPS results for thicker (17 Å) $Al_2O_3/Ni_3Al(110)$ films, and indicate that this H_2O-induced instability cannot be ascribed to the extreme thinness of the film.

4.4. Discussion

The results presented here indicate that Al_2O_3 films grown on $Ni_3Al(110)$ and $Ni_3Al(111)$ substrates display a striking instability to low-intermediate partial pressures of H_2O (> 10^{-5} Torr), 300 K. This instability results in substantial roughening of the film and loss of long-range order without the formation of a stable surface hydroxide (at least one that is observable under UHV conditions). These results are in excellent agreement with those previously reported [7] for a substantially thicker (17 Å) Al_2O_3 film. These results are also consistent with experimental and theoretical data [49] for transitional phase alumina films ~ 80 Å which indicate that exposure to H_2O results in the permeation of atomic hydrogen into the film, but not OH or bulk hydroxide formation. Therefore, the

H_2O-specific structural instability of the alumina films described here cannot be ascribed to the extreme thinness of the films (< 1 nm), but is consistent with reported [7, 49] behavior for thicker transitional phase aluminas.

The data in Fig. 4.4 and 4.7 indicate that the surface transformation is initiated at localized regions of the oxide surface, and that the surface area affected increases gradually with exposure time. This is consistent with a transformation process that begins

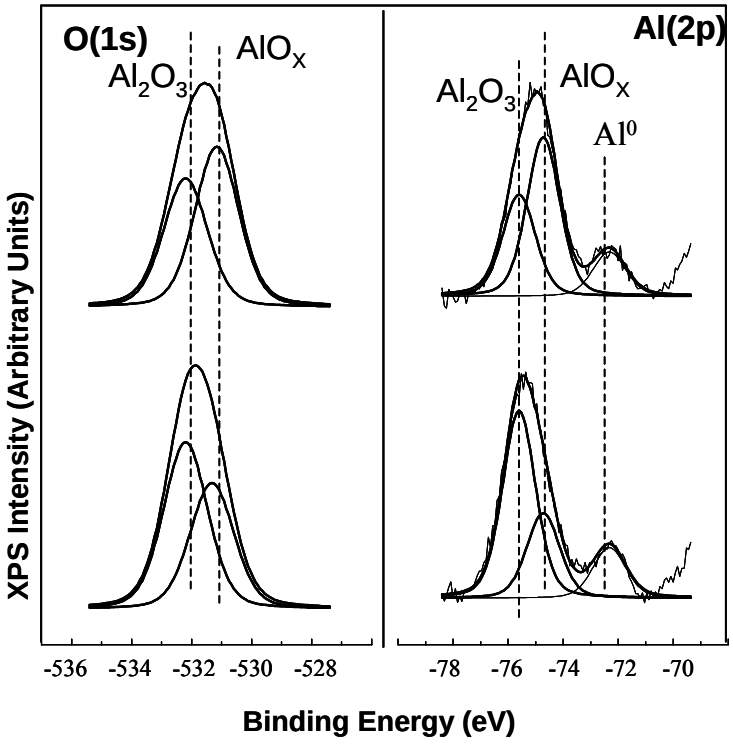

Fig. 4.8. O(1s) and Al(2p) XPS spectra for $Al_2O_3/Ni_3Al(110)$ before (a and b) and after (c and d) exposure to H_2O (10^{-4} Torr, 45 minutes, 300 K).

at defect sites of some type (whether of atomic or larger dimensions) – a nucleation and growth mechanism—rather than by a temporally abrupt surface reconstruction. These

data therefore also suggest that *there is really no critical* P_{H_2O} *below which some transformation will not occur*, only that the time for the transformation process to affect areas of the film increases in a non-linear manner as P_{H_2O} decreases. Since the degradation begins at the outer oxide surface, degradation at the film/metal interface might not be readily observable at practical time intervals under dry conditions.

The exact mechanism of the H_2O-oxide interaction cannot be explained by the existing data. Most puzzling is the fact that no hydroxide phase is observed *in UHV* for $P_{H_2O} < \sim 1$ Torr. Above 1 Torr, an alumina hydroxide is observed by XPS on both alpha-alumina(0001) [4, 5] and $Al_2O_3/Ni_3Al(110)$ [7]. That dissociative adsorption of H_2O occurs for $P_{H_2O} < 1$ Torr is indicated by the presence of interstitial H in alumina films exposed to water vapor [49]. This suggests a H_2O/alumina complex which is stabilized by the presence of an overpressure of H_2O:

$$xH_2O + Al^{+3}_{surface} \square Al^{+3-x}(OH)_x + x\ H\ (interstitial) \qquad (4\text{-}2)$$

The formation of additional alumina is precluded because AES (not shown) and XPS (Fig. 4.8) indicate no significant additional oxide formation upon sample reintroduction into UHV chamber. The fact that equal exposures at different pressures yield different results (Figs. 4.5, 4.6) indicates that the surface reconstruction process is not dependent on the number of individual H_2O/surface interactions [47]. The pressure dependence, rather than exposure dependence of the surface reconstruction process is strong evidence that a cooperative H_2O/surface reaction, involving more than one H_2O molecule (i.e. $x > 1$ in Eqn. 4-2) is occurring on the surface. The plausibility of such a pathway to induce

H_2O dissociation at the sapphire(0001) surface has been demonstrated [26]. The involvement of a cooperative pathway would also explain the failure to see such effects at alumina surfaces under UHV conditions.

The relatively greater sensitivity of $Al_2O_3/Ni_3Al(110)$ film compared to the film grown on $Ni_3Al(111)$ (Fig. 4.7) suggests that the interfacial structure plays a role in this phenomenon, even though the film reconstruction is initiated at the oxide surface, rather than at the metal/oxide interface (Fig. 4.4). The LEED data for the annealed $Al_2O_3/Ni_3Al(110)$ film (Fig. 3.5 in section 3.3) indicate the presence of a hexagonal interfacial region with 2.9 Å lattice constant, which corresponds to the Al(111) structure. The XPS Al(2p) spectrum for the annealed film (Fig. 4.3) also indicates the presence of a metallic aluminum interfacial layer, as does the AES spectrum (Fig. 3.2 in section 3.3). The data therefore indicate that the interface between the alumina layer and the $Ni_3Al(110)$ surface is actually an Al(111) interface, as proposed by Cotteril et al. [35]. Such a (111)/(110) interface would be incommensurate. In contrast, LEED, AES and STM data [9] by Addepalli et al., indicate that the $Al_2O_3/Ni_3Al(111)$ interface also has an Al(111) interfacial layer, which results in a commensurate interface. The LEED spectrum for the $Al_2O_3/Ni_3Al(110)$ indicates a ~ 10 Å × 3 Å rectangular unit cell, which is consistent with a transitional phase alumina, as is the LEED data for the film grown on the $Ni_3Al(111)$ surface [9]. This is hardly surprising, in view of the annealing temperatures involved. Therefore, both the $Al_2O_3/Ni_3Al(110)$ and $Al_2O_3/Ni(111)$ films are transitional phases with an Al(111) transitional layer, and the main difference between the two is the weakly bonded interface at the (110) surface. The data in Fig. 4.7

demonstrate that the H_2O-induced reconstruction involves significant mass transport within the oxide layer. STM data [50] for hydroxylated Cr_2O_3/Cr(110) (which has the corundum structure) suggest that hydroxylation induces a high degree of ion mobility. One possibility, therefore, is that hydrated or hydroxylated Al cations become more mobile within the oxide layer under intermediate pressures of H_2O. When the overpressure of H_2O is removed under UHV conditions, the commensurate (111) interface might provide a more stable template for the reformation of the oxide.

Although the exact relationship of the H_2O-induced instability observed here to the moisture-induced spallation of "real world" alumina coatings is beyond the scope of this paper, certain parallels are inescapable:

(1) This phenomenon occurs readily at 300 K.

(2) This phenomenon is inhibited at extremely low P_{H_2O} (~ 10^{-5} Torr).

4.5. Conclusions

STM, LEED, AES and XPS data are used to study the oxidation of Ni_3Al(110) and Ni_3Al(111) and the interaction with the resulting oxide films with water vapor at the pressure range of 10^{-5} to 10^{-3} Torr. The data presented above confirm previous observations [7] and demonstrate that (a) the alumina films grown on Ni_3Al(111) and Ni_3Al(110) are unstable to extremely mild conditions: $P_{H_2O} > \sim 10^{-5}$ Torr, 300 K; (b) the film grown on the (110) substrate (Al_2O_3/Ni_3Al(110)) is significantly more sensitive to H_2O vapor than the Al_2O_3/Ni_3Al(111) film, and this may be due to the incommensurate nature of the oxide/Ni_3Al(110) interface; (c) this surface reconstruction effect, is not

associated with formation of a surface hydroxide observable in UHV, yet is specific to H_2O, since similar O_2 exposures have no effect on both oxide films; (d) that the oxide instability is initiated at the oxide surface, rather than at the oxide/metal interface; and (e) that the data also show that the H_2O-induced reconstruction is pressure-dependent rather than exposure-dependent.

4.6. Summary and Recommendations

The results presented in this chapter indicate that transitional phase (non-alpha) alumina surfaces become dynamic in contact with intermediate pressures ($> 10^{-7}$ Torr – 0.1 Torr) of water vapor at 300 K. Other data [49] strongly suggest that, under such conditions, alumina films may store atomic hydrogen. Such novel phenomena have significant implications for aluminum oxides as thermal barrier coatings in fossil fuel applications, in MEMS applications, ceramic composites, hydrogen production and nanocatalyst supports, and corrosion barriers. Our results also demonstrate that these transitional phase alumina surfaces exhibit fundamentally different behavior than 1) the alpha-phase, or sapphire, at water vapor partial pressures $P_{H_2O} < 1$ Torr, and 2) than transitional phase surfaces at lower pressures, such as UHV ($P_{H_2O} \leq 10^{-8}$ Torr).

Furthermore, our results indicate that for transitional phase alumina, a cooperative (pressure-dependent) H_2O reaction mechanism results in the nucleation and growth of a dramatically reconstructed surface. This occurs without the formation of a UHV-stable hydroxide and at far lower pressures of H_2O but still well above UHV. The existence of a cooperative (pressure, rather than exposure-dependent) H_2O reaction mechanism, the

absence of stable hydroxide formation and the possible generation of atomic hydrogen, demonstrate the need for precise, *in-situ* surface science studies under rigorously controlled *non-UHV* conditions.

In this context, *in-situ* variable pressure/temperature scanning tunneling microscopy (VP/VTSTM) and reflection absorption infrared (RAIR) studies should be carried out on well defined aluminum oxide thin film surfaces at 10^{-7} Torr < P_{H_2O} < 10 Torr and at temperatures between 300 K and ~1200 K. In addition, electron spin resonance (ESR) studies should be carried out to detect the formation of atomic hydrogen.

4.7. Chapter References

[1] Dellwig, T., Rupprechter, G., Unterhalt, H. and Freund, H.-J., *Phys. Rev. Lett.*, **85**, 776 (2000).

[2] Chambers, S. A., Droubay, T., Jennison, D. R. and Mattsson, T. R., *Science*, **297**, 827 (2002).

[3] Tolpygo, V. K. and Clarke, D. R., *Mater. Sci. Eng. A,* **278**, 151 (2000).

[4] Liu, P., Kendelewicz, T., G. Brown, J., Neslon, E. J. and Chambers, S. A., *Surf. Sci.*, **417**, 53 (1998).

[5] Niu, C., Shepherd, K., Martini, D., J.Tong, Kelber, J. A., Jennison, D. R. and Bogicevic, A., *Surf. Sci.*, **465**, 163 (2000).

[6] Gassmann, P., Franchy, R. and Ibach, H., *Surf. Sci.*, **319**, 95 (1994).

[7] Garza, M., Magtoto, N. P. and Kelber, J. A., *Surf. Sci.*, **519**, 259 (2002).

[8] Qin, F., Magtoto, N. P., Kelber, J. A. and Jennison, D. R., *J. Molec. Catal. A*, **228**, 83 (2005).

[9] Addepalli, S. G., Ekstrom, B., Magtoto, N. P., Lin, J.-S. and Kelber, J. A., *Surf. Sci.*, **442**, 385 (1999).

[10] Bardi, U., Atrei, A. and Rovida, G., *Surf. Sci.*, **268**, 87 (1992).

[11] Becker, C., Kandler, J., Raaf, H., Linker, R., Pelster, T., Draeger, M., Tanemura, M. and Wandelt, K., *J. Vac. Sci. Technol. A*, **16**, 1000 (1998).

[12] Libuda, J., Frank, M., Sandell, A. and Freund, H.-J., *Surf. Sci.*, **384**, 106 (1997).

[13] Jennison, D. R. and Bogicevic, A., *Surf. Sci.*, **464**, 108 (2000).

[14] Svensson, H., Angentete, J. and Stiller, K., *Surface and Coatings Technology*, **177-178**, 152 (2004).

[15] Yadav, O. P., Palmqvist, A., Cruise, N. and Holmberg, K., *Colloids and Surfaces A: Physicochem. Eng. Aspects*, **221**, 131 (2003).

[16] Hansen, K. H., Worren, T., Stempel, S., Laegsgaard, E., Baumer, M., Freund, H.-J., Besenbacher, F. and Stensgaard, I., *Phys. Rev. Lett.*, **83**, 4120 (1999).

[17] Hsiao, G., Erley, W. and Ibach, H., *Surf. Sci.*, **405**, L465 (1998).

[18] Smialek, J. L. and Morscher, G. N., *Mater. Sci. Eng. A*, **332**, 11 (2002).

[19] Smith, M. A., Frazier, W. E. and Pregger, B. A., *Mater. Sci. Eng. A*, **203**, 388 (1995).

[20] Sergo, V. and Clarke, D. R., *J. Am. Ceram. Soc.*, **81**, 3237 (1998).

[21] Maris-Sida, M. C., Meier, G. H. and Pettit, F. S., *Metall. and Mater. Trans. A*, **34A**, 2609 (2003).

[22] Smialek, J. L., *Acta Materialia*, **51**, 469 (2003).

[23] Janakiraman, R., Meier, G. H. and Pettit, F. S., *Metall. and Mater. Trans. A*, **30A**, 2905 (1999).

[24] Wang, X.-G., Chaka, A. and Scheffler, M., *Phys. Rev. Lett.*, **84**, 3650 (2000).

[25] Ruberto, C., Yourdshahyan, Y. and Lundqvist, B. I., *Phys. Rev. B*, **67**, 195412 (2003).

[26] Hass, K. C., Schneider, W. F., Curioni, A. and Andreoni, W., *Science*, **282**, 265 (1998).

[27] Jennison, D. R. and Mattsson, T. R., *Surf. Sci.*, **544**, L689 (2003).

[28] Baumer, M. and Freund, H.-J., *Prog. Surf. Sci.*, **61**, 127 (1999).

[29] Al-Abadleh, H. A. and Grassian, V. H., *Langmuir*, **19**, 341 (2003).

[30] Baumer, M., Frank, M., Heemeier, M., Kuhnemuth, R., Stempel, S. and Freund, H.-J., *Surf. Sci.*, **454-456**, 957 (2000).

[31] Frederick, B. G., Apai, G. and Rhodin, T. N., *Surf. Sci.*, **244**, 67 (1991).

[32] Shen, Y. G., O'Connor, D. J. and McDonald, R. J., *Surf. Interf. Anal.*, **18**, 729 (1992).

[33] Shen, Y. G., O'Connor, D. J. and MacDonald, R. J., *Surf. Interf. Anal.*, **17**, 903 (1991).

[34] Seah, M. P., Practical Surface Analysis, Wiley, New York, 1990.

[35] Cotterill, G. F., Niehus, H. and O'Connor, D. J., *Surf. Rev. Lett.*, **3**, 1355 (1996).

[36] Cappus, D., Xu, C., Ehrlich, D., Dillmann, B., C. A. Ventrice, J., Al-Shamery, K., Kuhlenbeck, H. and Freund, H.-J., *Chem. Phys.*, **177**, 533 (1993).

[37] Evans, S., Pielaszek, J. and Thomas, J. M., *Surf. Sci.*, **55**, 644 (1976).

[38] Tyuliev, G. T. and Kostov, K. L., *Phys. Rev. B*, **60**, 2900 (1999).

[39] Chen, C., Splinter, S. J., Do, T. and McIntyre, N. S., *Surf. Sci*, **382**, L652 (1997).

[40] Fuggle, J. C., Watson, L. M. and Fabian, D. J., *Surf. Sci.*, **49**, 61 (1975).

[41] Venezia, A. M. and Loxton, C. M., *Surf. Sci.*, **194**, 136 (1988).

[42] Tzvetkov, G., Zubavichus, Y., Koller, G., Schmidt, T., Heske, C., E.Umbach, Grunze, M., Ramsey, M. G. and Netzer, F. P., *Surf. Sci.*, **543**, 131 (2003).

[43] Jaeger, R. M., Kuhlenbeck, H., Freund, H.-J., Wuttig, M., Hoffmann, W., Franchy, R. and Ibach, H., *Surf. Sci.*, **259**, 235 (1991).

[44] Libuda, J., Winkelmann, F., Bäumer, M., Freund, H.-J., Bertrams, T., Neddermeyer, H. and Müller, K., *Surf. Sci.*, **318**, 61 (1994).

[45] Zhong, Q. and Ohuchi, F. S., *J. Vac. Technol. A*, **8**, 2017 (1990).

[46] Calow, C. A. and Porter, I. T., *J. Mater. Sci.*, **6**, 156 (1971).

[47] Somorjai, G. A., Introduction to Surface Chemistry and Catalysis, John Wiley & Sons, Inc, New York, 1994.

[48] Kelber, J. A., Niu, C., Shepherd, K., Jennison, D. R. and Bogicevic, A., *Surf. Sci.*, **446**, 76 (2000).

[49] Jennison, D. R., Schultz, P. A. and Sullivan, J. P., *Phys. Rev. B.*, **69**, 041405(R) (2004).

[50] Maurice, V., Cadot, S. and Marcus, P., *Surf. Sci.*, **471**, 43 (2001).

REFERENCE LIST

Addepalli, S. G., Ekstrom, B., Magtoto, N. P., Lin, J.-S. and Kelber, J. A., *Surf. Sci.*, **442**, 385 (1999).

Addepalli, S. G., Magtoto, N. P. and Kelber, J. A., *Langmuir*, **16**, 8352 (2000).

Addepalli, S. G., Magtoto, N. P. and Kelber, J. A., *Surf. Sci.*, **458**, 123 (2000).

Ahn, J. and Rabalais, J. W., *Surf. Sci.*, **388**, 121 (1997).

AKagi, K. and Tsukada, M., *Thin Solid Films*, **343-344**, 397 (1999).

Akpati, H. C., Nordlander, P., Lou, L. and Avouris, P., *Surf. Sci.*, **401**, 47 (1998).

Al-Abadleh, H. A. and Grassian, V. H., *Langmuir*, **19**, 341 (2003).

Anast, M., Jamting, Å., Bell, J. M. and Ben-Nissan, B., *Thin Solid Films*, **253**, 303 (1994).

Anders, S., Anders, A., Rubin, M., Wang, Z., Raoux, S., Kong, F. and Brown, I. G., **76-77**, 167 (1995).

Arabcysk, W. and Narkiewicz, U., *Appl. Surf. Sci.*, **108**, 379 (1997).

Aronniemi, M., Sainio, J. and Lahtinen, J., *Surf. Sci.*, **578**, 108 (2005).

Avouris, P., Walkup, R. E., Rossi, A. R., Shen, T.-C., Abeln, G. C., Tucker, J. R. and Lyding, J. W., *Chem. Phys. Lett.*, **257**, 148 (1996).

Bardi, U., Atrei, A. and Rovida, G., *Surf. Sci.*, **268**, 87 (1992).

Baumer, M., Frank, M., Heemeier, M., Kuhnemuth, R., Stempel, S. and Freund, H.-J., *Surf. Sci.*, **454-456**, 957 (2000).

Bäumer, M. and Freund, H.-J., *Prog. Surf. Sci*, **61**, 127 (1999).

Becker, C., Kandler, J., Raaf, H., Linker, R., Pelster, T., Draeger, M., Tanemura, M. and Wandelt, K., *J. Vac. Sci. Technol. A*, **16**, 1000 (1998).

Bertrams, T., Brodde, A. and Neddermeyer, H., *J. Vac. Sci. Technol. B*, **12**, 2122 (1994).

Betrabet, H. S., Reddy, S. N. S. and Pureshothaman, S., *Ceramic Eng. Sci. Proc.*, **10**, 1531 (1989).

Binning, G., Rohrer, H., Gerber, C. and Weibel, E., *Phys. Rev. Lett.*, **49**, 57 (1982).

Blum, R.-P., Ahlbehrendt, D. and Niehus, H., *Surf. Sci.*, **396**, 176 (1998).

Bownell, D. A., *Prog. Surf. Sci.*, **57**, 187 (1998).

Briggs, D. and Seah, M. P., Pratical Surface Analysis, Vol. 1, John Wiley & Sons Ltd, New York, 1990.

Brundle, C. R., Chuang, T. J. and Wandelt, K., *Surf. Sci.*, **68**, 459 (1977).

Calow, C. A. and Porter, I. T., *J. Mater. Sci.*, **6**, 156 (1971).

Cappus, D., Xu, C., Ehrlich, D., Dillmann, B., C. A. Ventrice, J., Al-Shamery, K., Kuhlenbeck, H. and Freund, H.-J., *Chem. Phys.*, **177**, 533 (1993).

Carlsson, A. F., Naschitzki, M., Bäumer, M. and Freund, H.-J., *Surf. Sci.*, **545**, 143 (2003).

Ceballos, G., Spong, Z., Pascual, J. I., Rust, H.-P., Conrad, H., Baumer, M. and Freund, H.-J., *Chem. Phys. Lett.*, **359**, 41 (2002).

Chambers, S. A. and Joyce, S. A., *Surf. Sci.*, **420**, 111 (1999).

Chambers, S. A., Droubay, T., Jennison, D. R. and Mattsson, T. R., *Science*, **297**, 827 (2002).

Chen, J. G., Crowell, J. E. and J. T. Yates, J., *Phys. Rev. B*, **33**, 1436 (1986).

Chen, C., Splinter, S. J., Do, T. and McIntyre, N. S., *Surf. Sci*, **382**, L652 (1997).

Chen, C.-C., Chang, C.-Y., chien, C.-H., Huang, T.-Y., Lin, H.-C. and Liang, M.-S., *Appl. Phys. Lett.*, **74**, 3708 (1999).

Chen, L., Magtoto, N. P., Addepali, S., Ekstrom, B. and kelber, J. A., *Oxid. Met.*, **54**, 285 (2000).

Chinchen, G., Davis, P. and Sampson, R. J., in J. R. Anderson and M. Boudart (Eds.): Catalysis: Science and technology, Vol. 8, Springer, Berlin, 1987.

Condon, N. G., Murray, P. W., Leibsle, F. M., Thornton, G., Lennie, A. R. and Vaughan, D. J., *Surf. Sci.*, **310**, L609 (1994).

Condon, N. G., Leibsle, F. M., Lennie, A. R., Murray, P. W., Vaughan, D. J. and Thornton, G., *Phys. Rev. Lett.*, **75**, 1961 (1995).

Condon, N. G., Leibsle, F. M., Lennie, A. R., Murray, P. W., Parker, T. M., Vaughan, D. J. and Thornton, G., *Surf. Sci.*, **397**, 278 (1998).

Cotterill, G. F., Niehus, H. and O'Connor, D. J., *Surf. Rev. Lett.*, **3**, 1355 (1996).

Dake, L. S. and Lad, R. J., *Surf. Sci.*, **289**, 297 (1993).

Davis, L. E., MacDonald, N. C., Palmberg, P. W., Raich, G. E. and Weber, R. E., Handbook of Auger Electron Spectroscopy, Physical Electronics Industries, Inc, Eden Prairie, MN, 1979.

Dellwig, T., Rupprechter, G., Unterhalt, H. and Freund, H.-J., *Phys. Rev. Lett.*, **85**, 776 (2000).

Diebold, U., Pan, J. M. and Madey, T. E., *Phys. Rev. B*, **47**, 3868 (1993).

Elam, J. W., Nelson, C. E., Cameron, M. A., Tolbert, M. A. and George, S. M., *J. Phys. Chem. B*, **102**, 7008 (1998).

Eng, P. J., Trainor, T. P., G. E. Brown, J., Waychunas, G. A., Neville, M., Sutton, S. R. and Rivers, M. L., *Science*, **288**, 1029 (2000).

Erley, W. and Ibach, H., *Solid State Commun.*, **37**, 937 (1981).

Ernst, F., *Mat. Sci. Eng.*, **R14**, 97 (1995).

Ertl, G. and Kueppers, J., Low Energy Electrons and Surface Chemistry, Vol. 4, Verlag Chemie, Weinheim, 1974.

Ertl, G. and Wandelt, K., *Surf. Sci.*, **50**, 479 (1975).

Ertl, G. and Kuppers, J., Low Energy Electrons and Surface Chemistry, VCH Publishers, New York, 1985.

Eumann, M., Schmitz, G. and Franchya, R., *Appl. Phys. Lett.*, **72**, 3440 (1998).

Evans, S., Pielaszek, J. and Thomas, J. M., *Surf. Sci.*, **55**, 644 (1976).

Fan, J. C. C. and Henrich, V. E., *Appl. Phys. Lett.*, **25**, 401 (1974).

Fauer, G., Principles and Applications of Inorganic Geochemistry, MavMillan, New York, 1991.

Feenstra, R. M., *Surf. Sci.*, **299-300**, 965 (1994).

Feldman, L. C. and Mayer, J. W., Fundamentals of Surface and Thin Film Analysis, P T R Prentice Hall, Englewood Cliffs, 1986.

Fellows, R. A., Lenie, A. R., Raza, H., Pang, C. L., Thornton, G. and Vaughan, D. J., *Surf. Sci.*, **445**, 11 (2000).

Fontana, M. G., Corrosion Engineering, McGraw-Hill, Inc., New York, 1986.

Franchy, R., *Surf. Sci. Rep.*, **38**, 195 (2000).

Frederick, B. G., Apai, G. and Rhodin, T. N., *Surf. Sci.*, **244**, 67 (1991).

Freund, H.-J., Dillmann, B., Seiferth, O., Klivenyi, G., Bender, M., Ehrlich, D., Hemmerich, I. and Cappus, D., *Catal. Today*, **32**, 1 (1996).

Freund, H.-J., Baumer, M., Libuda, J., Risse, T., Rupprechter, G. and Shaikhutdinov, S., *J. Catal.*, **216**, 223 (2003).

Fuggle, J. C., Watson, L. M. and Fabian, D. J., *Surf. Sci.*, **49**, 61 (1975).

Fukano, Y., Sugawara, Y., Yamanishi, Y., Oasa, T. and Morita, S., *Jpn. J. Appl. Phys.*, **32**, 290 (1993).

Gafner, G. and Feder, R., *Surf. Sci.*, **57**, (1976).

Garza, M., Magtoto, N. P. and Kelber, J. A., *Surf. Sci.*, **519**, 259 (2002).

Gassman, P., Franchy, R. and Ibach, H., *Surf. Sci.*, **319**, 95 (1994).

Giordano, L., Goniakowski, J. and Suzanne, J., *Phys. Rev. Lett.*, **81**, 1271 (1998).

Golodets, G. I., Heterogeneous Catalytic Reaction Involving Molecular Oxygen, Elsevier, Amsterdam, 1983.

Goodman, D. W., *Surf. Sci.*, **299-300**, 837 (1994).

Goodman, D. W., *J. Vac. Sci. Technol. A*, **14**, 1526 (1996).

Graupner, H., Hammer, L., Heinz, K. and Zehner, D. M., *Surf. Sci.*, **380**, 335 (1997).

Guinn, K. V., Donnelly, V. M., Gross, M. E., Baiocchi, F. A., Petrov, I. and Greene, J. E., *Surf. Sci*, **295**, 219 (1993).

Hansen, K. H., Worren, T., Stempel, S., Laegsgaard, E., Baumer, M., Freund, H.-J., Besenbacher, F. and Stensgaard, I., *Phys. Rev. Lett.*, **83**, 4120 (1999).

Hass, K. C., Schneider, W. F., Curioni, A. and Andreoni, W., *Science*, **282**, 265 (1998).

Henderson, M. A., *Surf. Sci. Rep.*, **46**, 1 (2002).

Henrich, V. E. and Cox, P. A., The Surface Science of Metal Oxides, Cambridge University Press, New York, 1994.

Hickmott, T. W., *J. Appl. Phys.*, **88**, 2805 (2000).

Hohenberg, P. and Kohn, W., *Phys. Rev.*, **136**, B864 (1964).

Homeny, J. and Buckley, M. M., *Mater. Lett.*, **9**, 443 (1990).

Hsiao, G., Erley, W. and Ibach, H., *Surf. Sci.*, **405**, L465 (1998).

Huo, D. T. C., Yan, M. F. and Foo, P. D., *J. Vac. Sci. Technol. A*, **9**, 2602 (1991).

Imaduddin, S. and Lad, R. J., *Surf. Sci.*, **290**, 35 (1990).

Jacobsson, J. R., Thin Film Technologies, SPIE, Bellingham, WA, 1983.

Jacoby, M., *C & E News*, **80**, 4 November (2002).

Jaeger, R. M., Kuhlenbeck, H., Freund, H.-J., Wuttig, M., Hoffmann, W., Franchy, R. and Ibach, H., *Surf. Sci.*, **259**, 235 (1991).

Janakiraman, R., Meier, G. H. and Pettit, F. S., *Metall. and Mater. Trans. A*, **30A**, 2905 (1999).

Jansen, R., Brabers, V. A. M. and Kempen, H. v., *Surf. Sci.*, **328**, 237 (1995).

Jennison, D. R., Verdozzi, C., Schultz, P. A. and Sears, M. P., *Phys. Rev. B*, **59**, R15605 (1999).

Jennison, D. R. and Bogicevic, A., *Surf. Sci.*, **464**, 108 (2000).

Jennison, D. R. and Mattsson, T. R., *Surf. Sci.*, **544**, L689 (2003).

Jennison, D. R., Schultz, P. A. and Sullivan, J. P., *Phys. Rev. B.*, **69**, 041405(R) (2004).

Jones, D. A., Principles and Preventions of Corrosion, Macmillan Publishing Company, New York, 1991.

Kelber, J. A., Addepalli, S. G., Lin, J.-S. and Cabibil, H., P. Y. Hou, M. J. McNallan, R. Oltra, E. J. Opila and D. A. Shores, High Temperature Corrosion and Materials Chemistry, San Diego, CA, 1998, The Electrochemical Society, Inc., 98-99 (1998) 190.

Kelber, J. A., Niu, C., Shephed, K., Jennison, D. R. and Bogicevic, A., *Surf. Sci.*, **446**, 76 (2000).

Kim, H.-J., Park, J.-H. and Vescovo, E., *Phys. Rev. B*, **61**, 15284 (2000).

Kizilkaya, O., Hite, D. A., Zehner, D. M. and Sprunger, P. T., *Surf. Sci.*, **529**, 223 (2003).

Kohn, W. and Sham, L. J., *Phys. Rev.*, **140**, A1133 (1965).

Kolodzey, J., Chowdhury, E. A., Adam, T. N., Qui, G., Rau, I., Olowolafe, J. O., Suehle, J. S. and Chen, Y., *IEEE Trans. Electron Devices*, **47**, 121 (2000).

Kresse, G. and Hafner, J., *Phys. Rev. B*, **47**, 558 (1993).

Kresse, G. and Hafner, J., *Phys. Rev. B*, **49**, 14251 (1995).

Kresse, G. and Furthmüller, J., *Phys. Rev. B*, **54**, 11169 (1996).

Kubaschewski, O. and Hopkins, B. E., Oxidation of Metals and Alloys, Butterworth and Co. Ltd., Northern Ireland, 1962.

Kulawik, M., Nilius, N., Rust, H. P. and Freund, H. J., *Phys. Rev. Lett*, **91**, 256101 (2003).

Kurnosikov, O., Nooij, F. C. d., LeClair, P., Kohlhepp, J. T., Koopmans, B., Swagten, H. J. M. and Jonge, W. J. M. D., *Phys. Rev. B*, **64**, 153407 (2001).

Lad, R. J., *Surf. Rev. Lett.*, **2**, 109 (1995).

langell, M. and Somorjai, G. A., *J. Vac. Sci. Technol.*, **21**, 858 (1982).

Lee, M. B., Lee, J. H., Frederick, B. G. and Richardson, N. V., *Surf. Sci.*, **448**, L207 (2000).

Lemire, C., Meyer, R., Henrich, V. E., Shaikhutdinov, S. and Freund, H.-J., *Surf. Sci.*, **572**, 103 (2004).

Libuda, J., Winkelmann, F., Bäumer, M., Freund, H.-J., Bertrams, T., Neddermeyer, H. and Müller, K., *Surf. Sci.*, **318**, 61 (1994).

Libuda, J., Frank, M., Sandell, A. and Freund, H.-J., *Surf. Sci.*, **384**, 106 (1997).

Lin, J.-S., Cabibil, H. and Kelber, J. A., *Surf. Sci.*, **395**, 30 (1998).

Lin, J.-S., Ekstrom, B., Addepalli, S. G., Cabibil, H. and Kelber, J. A., *Langmuir*, **14**, 4843 (1998).

Liu, P., Kendelewicz, T., G. Brown, J., Neslon, E. J. and Chambers, S. A., *Surf. Sci.*, **417**, 53 (1998).

Lohrengel, M. M., *Mater. Sci. and Eng. R.*, **11**, 243 (1993).

Lu, J.-P., Albert, M. and Bernasek, S. L., *Surf. Sci.*, **215**, 348 (1989).

Lucovsky, G., Richard, P. D., Tsu, D. V., Lin, S. Y. and Markunas, R. J., *J. Vac. Sci. Technol. A*, **4**, 681 (1986).

Magtoto, N., Niu, C., Ekstrom, B., Addepalli, S. and Kelber, J. A., *Appl. Phys. Lett.*, **77**, 2228 (2000).

Magtoto, N. P., Niu, C., Anzaldua, M., Kelber, J. A. and Jennison, D. R., *Surf. Sci.*, **472**, L157 (2001).

Marchese, L., Coluccia, S., Martra, G. and Zecchina, A., *Surf. Sci.*, **269**, 135 (1992).

Maris-Sida, M. C., Meier, G. H. and Pettit, F. S., *Metall. and Mater. Trans. A*, **34A**, 2609 (2003).

Masella, M., Gresh, N. and Flament, J.-P., *J. Chem. Soc. Faraday Trans.*, **94**, (1998).

Mattson, A. E. and Jennison, D. R., *Surf. Sci.*, **520**, 611 (2002).

Maurice, V., Cadot, S. and Marcus, P., *Surf. Sci.*, **471**, 43 (2001).

Metikos-Hukovic, M. and Omanovic, S., *Mat. Chem. Phys.*, **38**, 55 (1994).

Miyano, T., Sakisaka, Y., Komeda, T. and Onchi, M., *Surf. Sci.*, **169**, 197 (1986).

Miyazaki, T. and Tezuka, N., *J. Magn. Magn. Mater.*, **139**, L231 (1995).

Møller, P. J. and Wu, M.-C., *Surf. Sci.*, **224**, 265 (1989).

Niu, C., Shepherd, K., Martini, D., J.Tong, Kelber, J. A., Jennison, D. R. and Bogicevic, A., *Surf. Sci.*, **465**, 163 (2000).

Niu, C., Magtoto, N. P. and Kelber, J. A., *J. Vac. Sci. Technol. A*, **19**, 1947 (2001).

Ohtani, H., Kao, C.-T., Hove, M. A. V. and Somorjai, G. A., *Prog. Surf. Sci.*, **23**, 155 (1986).

Olivier, J. and Poirier, R., *Surf. Sci.*, **105**, 347 (1981).

Park, B. G. and Lee, T. D., *IEEE Trans. Magn.*, **35**, 2919 (1999).

Parmaliana, A., Arena, F. and Frusteri, F., *J. Chem. Soc. Faraday Trans.*, **86**, 2663 (1990).

Pendry, J. B., Low Energy Electron Diffraction, Academic Press Inc., New York, 1974.

Perdew, J. P. and Zunger, A., *Phys. Rev. B*, **23**, 5048 (1981).

Perdew, J. P., Chevary, J. A., Vosko, S. H., Jackson, K. A., Pederson, M. R., Singh, D. J. and Fiolhais, C., *Phys. Rev. B*, **46**, 6671 (1992).

Persson, B. N. J. and Avouris, P., *Surf. Sci.*, **390**, 45 (1997).

Qin, F., Magtoto, N. P. and Kelber, J. A., *Surf. Sci.*, **565**, L277 (2004).

Qin, F., Magtoto, N. P., Kelber, J. A. and Jennison, D. R., *J. Molec. Catal. A*, **228**, 83 (2005).

Rae, A. U. M., *Surf. Sci.*, **1**, 319 (1964).

Riviere, J. C., in D. Briggs and M. P. Seah (Eds.): Practical surface analysis: Auger and X-ray photoelectron spectroscopy, Vol. 1, Wiley, New York 1979, p. 19.

Roberts, R. H. and Ramsey, J. A., *J. Electron Spectrosc.*, **52**, 185 (1990).

Rosenhahn, A., Schneider, J., Becker, C. and Wandelt, K., *Appl. Surf. Sci.*, **142**, 169 (1999).

Rosenhahn, A., Schneider, J., Kandler, J., Becker, C. and Wandelt, K., *Surf. Sci.*, **433-435**, 705 (1999).

Ruberto, C., Yourdshahyan, Y. and Lundqvist, B. I., *Phys. Rev. B*, **67**, 195412 (2003).

Sault, A. G., *Appl. Surf. Sci.*, **74**, 249 (1994).

Schedel-Niedrig, T., Weiss, W. and Schlogl, R., *Phys. Rev. B*, **52**, 17449 (1995).

Schmitz, G., Gassmann, P. and Franchy, R., *J. Appl. Phys.*, **83**, 2533 (1998).

Scully, J. C., The Fundamentals of Corrosion, Pergamon Press, New York, 1990.

Seah, M. P., in D. Briggs and M. P. Seah (Eds.): Practical surface analysis: Auger and X-ray photoelectron spectroscopy, Vol. 1, Wiley, New York, 1990, p. 201.

Seah, M. P., Practical Surface Analysis, Wiley, New York, 1990.

Seo, M., Lumsden, J. B. and Staehle, R. W., *Surf. Sci.*, **42**, 337 (1974).

Seo, M., Lumsden, J. B. and Staehle, R. W., *Surf. Sci.*, **50**, 541 (1975).

Sergo, V. and Clarke, D. R., *J. Am. Ceram. Soc.*, **81**, 3237 (1998).

Shen, Y. G., O'Connor, D. J. and MacDonald, R. J., *Surf. Interf. Anal.*, **17**, 903 (1991).

Shen, Y. G., O'Connor, D. J. and McDonald, R. J., *Surf. Interf. Anal.*, **18**, 729 (1992).

Siegbahn, K., Nording, C. N., Fahlman, A., Nordberg, R., Hamrin, K., Hedman, J., Johansson, G., Bermark, T., Karlsson, S. E., Lindgren, I. and Linberg, B., ESCA: Atomic, Molecular and Solid State Structure Studied by Means of Electron Spectroscopy, Almqvist and Wilksells, Uppsala, 1967.

Siegel, D., Louis G. Hector, J. and Adams, J. B., *Phys. Rev. B*, **65**, 85415

Simmons, G. W. and Dwyer, D. J., *Surf. Sci.*, **48**, 373 (1975).

Smentkowski, V. S. and J. T. Yates, J., *Surf. Sci.*, **232**, 113 (1990).

Smialek, J. L. and Morscher, G. N., *Mater. Sci. Eng. A*, **332**, 11 (2002).

Smialek, J. L., *Acta Materialia*, **51**, 469 (2003).

Smith, M. A., Frazier, W. E. and Pregger, B. A., *Mater. Sci. Eng. A*, **203**, 388 (1995).

Somorjai, G. A., Introduction to Surface Chemistry and Catalysis, John Wiley & Sons Ltd, New York, 1994.

Stanka, B., Hebenstreit, W., Diebold, U. and Chambers, S. A., *Surf. Sci.*, **448**, 49 (2000).

Stierle, A., Renner, F., Streitel, R., Dosch, H., Drube, W. and Cowie, B. C., *Science*, **303**, 1652 (2004).

Street, S. C., Xu, C. and Goodman, D. W., *Annu. Rev. Phys. Chem.*, **48**, 43 (1997).

Strehlow, W. H. and Cook, E. L., *J. Phys. Chem. Ref. Data*, **2**, 163 (1973).

Strongin, D. R., Bare, S. R. and Somorjai, G. A., *J. Catal.*, **103**, 289 (1987).

Sullivan, J. P., Dunn, R. G., Barbour, J. C., Wall, F. D., Missert, N. and Buchheit, R. G., K. R. Hebert, R. S. Lillard and B. R. MacDougall, Oxide Films, Toronto, Canada, 2000, Electrochemical Society, Inc., 2000-4 (2000) 24.

Svensson, H., Angentete, J. and Stiller, K., *Surface and Coatings Technology*, **177-178**, 152 (2004).

Tolpygo, V. K. and Clarke, D. R., *Mater. Sci. Eng. A*, **278**, 151 (2000).

Tsuji, M., Sakumoto, M., Itoh, N., Obase, H. and Nishimura, Y., *Appl. Surf. Sci.*, **51**, 171 (1991).

Tyuliev, G. T. and Kostov, K. L., *Phys. Rev. B*, **60**, 2900 (1999).

Tzvetkov, G., Zubavichus, Y., Koller, G., Schmidt, T., Heske, C., Umbach, E., Grunze, M., Ramsey, M. G. and Netzer, F. P., *Surf. Sci.*, **543**, 131 (2003).

Vanderbilt, D., *Phys. Rev. B*, **41**, 7892 (1990).

Venezia, A. M. and Loxton, C. M., *Surf. Interface Anal.*, **2**, 287 (1988).

Venezia, A. M. and Loxton, C. M., *Surf. Sci.*, **194**, 136 (1988).

Vurens, G. H., Salmeron, M. and Somorjai, G. A., *Prog. Surf. Sci.*, **33**, 333 (1990).

Wallace, R. M., Chen, P. J., Archer, L. B. and Anthony, J. M., *J. Vac. Sci. Technol. B*, **17**, 2153 (1999).

Wang, X.-G., Chaka, A. and Scheffler, M., *Phys. Rev. Lett.*, **84**, 3650 (2000).

Watanabe, H., Baba, T. and Ichikawa, M., *J. Appl. Phys.*, **85**, 6704 (1999).

Weiss, W., Barbieri, A., Hove, M. A. V. and Somorjai, G. A., *Phys. Rev. Lett.*, **71**, 1848 (1993).

Welsh, I. D. and Sherwood, P. M. A., *Phys. Rev. B*, **40**, 6386 (1989).

West, J. M., Basic Corrosion and Oxidation, 2nd ed., Ellis Horwood Limited, Chichester, 1986.

Wiesendanger, R., Shvets, I. V., Burgler, D., Tarrach, G., Guntherodt, H. J., Cory, J. M. D. and Graser, S., *Science*, **255**, 583 (1992).

Wiesendanger, R., Scanning Probe Microscopy and Spectroscopy: Methods and Applications, Cambridge University Press, Cambridge, 1994.

Wilhelm, S. M., Yun, K. S., Ballenger, L. W. and Hackerman, N., *Electrogenerated Chemiluminescence*, **126**, 419 (1979).

Woodruff, D. P. and Delchar, T. A., Modern Techniques of Surface Science, Cambrige University Press, New York, 1994.

Wu, M.-C. and Møller, P. J., *Surf. Sci.*, **224**, 250 (1989).

Wu, M., Estrada, C. A. and Goodman, D. W., *Phys. Rev. Lett.*, **67**, 2910 (1991).

Wu, M., Truong, C. and Goodman, D. W., Adsorption on Ordered Surfaces of Ionic Solids and Thin Films, Vol. 33, Springer Verlag, Heidelberg, 1993.

Xantheas, S. S. and Dunning, J., Thom H., *J. Chem. Phys.*, **99**, 8774 (1993).

Xantheas, S. S., *J. Chem. Phys.*, **100**, 7523 (1994).

Xu, Y., Wang, M. and Pickering, H. W., *J. Electrochem. Soc.*, **140**, 3448 (1993).

Xu, C. and Goodman, D. W., *Chem. Phys. Lett.*, **263**, 13 (1996).

Xu, C.-H., Gao, W. and He, Y.-D., *Scripta Mater*, **28**, 975 (2000).

Yadav, O. P., Palmqvist, A., Cruise, N. and Holmberg, K., *Colloids and Surfaces A: Physicochem. Eng. Aspects*, **221**, 131 (2003).

Yamada, H. and Makino, T., *Appl. Phys. Lett.*, **59**, 2159 (1991).

Yasue, T., Yoshida, Y., koyama, H., Kato, T. and Nishioka, T., *J. Vac. Sci. Technol. B*, **15**, 1884 (1997).

Young, E. W. A., Rivière, J. C. and Welch, L. S., *Appl. Surf. Sci.*, **28**, 71 (1987).

Yourdshahyan, Y., Reberto, C., Halvarsson, M., Bengtsson, L., Langer, V., Lundqvist, B. I., Ruppi, S. and Rolander, U., *J. Am. Ceram. Soc.*, **82**, 8265 (1999).

Zaki, M. I. and Knözinger, H., *J. Catal.*, **119**, 311 (1989).

Zhang, Z. and Satpathy, S., *Phys. Rev. B*, **44**, 13319 (1991).

Zhong, Q. and Ohuchi, F. S., *J. Vac. Sci. Technol. A*, **8**, 2107 (1990).